UNIVERSITY OF READING

DEPARTMENT OF MATHEMATICS AND STATISTICS

Multiscale Computer Simulation Studies of Entangled Branched Polymers

Jian Zhu

Thesis submitted for the degree of

Doctor of Philosophy

September 2016

Abstract

In this thesis, we investigate two problems of entangled branched polymers, i.e., the numerical solutions of the arm-retraction problem for well entangled star arms and the relaxation behaviours of branched polymers with different architectures. For the first problem, the arm retraction dynamics is studied using both the one-dimensional Rouse chain model and the slip-spring model by an advanced numerical method for the first-passage time problems, namely the forward flux sampling (FFS) method. In the one-dimensional Rouse chain model, we measured the first-passage time that the arm free end extends to a distance away from the origin, showing that the mean first-passage time is getting shorter if the Rouse chain is represented by more beads. The simulation results validate the prediction of an asymptotic solution for the multi-dimensional first-passage problem, which suggests the arm retraction time is much shorter than the prediction of the Milner-McLeish theory without constraint release. Then, we implement the FFS method to the slip-spring model and get the relaxation spectra for different arm lengths, ranging from mildly entangled to well-entangled star arms. We also proposed an algorithm to extract the dynamic observables, i.e., the end-to-end vector and stress relaxation functions, from the FFS simulation results. For the second problem, we conduct a series of molecular dynamics (MD) simulations using high performance GPU methods on the mildly entangled branched polymers of different architectures, including 3-arm symmetric and asymmetric stars, and H-shaped polymers. The slip-spring model, whose parameters are carefully calibrated according to the MD results of linear chains, is

also implemented to predict the relaxation behaviours of the branched polymers. We present a detailed analysis on the arm end-to-end vector relaxation functions and the monomer mean-squared displacements. By comparing the MD and slip-spring model simulation results, we propose a slip-link "hopping" mechanism, which accounts for the behaviour that the entanglements can pass through the branch point when the third arm is disentangled.

Declaration of Authorship

I confirm that this is my own work and the use of all material from other sources has been properly and fully acknowledged.

Acknowledgements

I would like to express my most sincere gratitude to my supervisors Professor Alexei E. Likhtman and Dr. Zuowei Wang for their continued support throughout my Ph.D study and related research.

Professor Alexei E. Likhtman sadly passed away before the completion of the thesis. His passion, focus, immense knowledge, and most all, the tireless desire to find scientific truth would be an eternal inspiration to all his students. He will be sorely missed not only as a mentor but also a friend.

My Ph.D study could not be accomplished without the meticulous guidance, patient help and constant encouragement from Dr. Zuowei Wang, whose insightful comments also inspired me to widen my research from various perspectives.

Besides my supervisors, I would like to thank Professor Mark W. Matsen, Dr. Patrick Ilg and Dr. Jing Cao for their kind guidance and enlightening discussions.

My sincere appreciation also goes to Dr Pawel Stasiak, Dipesh Amin, Changqiong Wang, Jack Kirk, Christopher R. Davies and other members of the Theoretical Polymer Physics group.

Finally, I would like thank my parents and friends for their constant support and encouragement.

Contents

List of Figures

Chapter 1

Introduction

1.1 Background

The annual worldwide production of synthetic polymers has reached several million tons and still undergoes continuous growth. Before being shaped into commercial plastic or rubber products, the raw materials are processed in molten or liquid state, thus our understanding of their rheology is crucial to enhancing their processing properties. Driven by industrial interests and scientific curiosity, both experimental and theoretical research on the rheological properties of bulk polymer fluids has experienced a fast development in the past half century. It is known that polymeric liquids have very complicated rheological and thus processing properties due to the hierarchical relaxation behaviours at different time and length scales. These behaviours are governed by polymer architectures and distribution of molecular weights. A typical example is that the presence of a small amount of **long chain branching (LCB)** in commercial polymers can dramatically affect rheological behaviour, e.g., giving them a much higher zero-shear viscosity η_0 than in linear systems with the same molecular weights. Understanding the relationship between LCB and rheology could simultaneously solve both the direct and inverse problems: to predict the rheological and thus the processing properties of a given polymer

system and using rheological measurements to deduce molecular weight distribution and identify LCB. Such relationship, however, remains to be one of the most challenging problems in polymer physics.

A typical polymer chain is constituted by repeated chemical units, called monomers, connected via covalent bonds. When polymers are in bulk, the polymer melts exhibit a fascinating property called "**viscoelasticity**". The stress of the viscoelastic materials neither simply depends on the strain nor the strain rate, but is a function of the deformation history [1, 2]. For example, in response to a small step strain γ, the stress σ of of an isotropic polymer liquid first raises to a level proportional to the strain, then slowly decays over a long period. Such behaviour showing both elasticity and viscosity could be qualitatively described by the general **Maxwell model**, which is constructed by connecting a set of linear springs and dashpots in series [3]. The stress modulus of the this mechanical model, $G(t)$, is a sum of exponentials:

$$G(t) = \sum_{i=1}^{m} G_i \exp\left(-t/\tau_i\right)$$

where G_i and τ_i are the moduli and the relaxation times of the **Maxwell modes**. The stress relaxation modulus exhibits an exponential decay beyond the longest relaxation time τ_m, which is also referred to as the terminal relaxation time τ_d in literature due to its significance.

The complexity of polymer dynamics is far beyond the description of the phenomenological mechanical models, which can be reflected in the rheological properties of polymers [4–7], and thus other measurements analogous to rheology, such as dielectric [8], optical [9] and diffusional [10, 11] properties. A typical example is the dependence of rheological properties on the molecular weight, M. For linear polymer melts, the viscosity η_0 increases linearly with M at low molecular weights, but exhibits power law growth of $M^{3.4}$ when M exceeds a critical value, M_c:

$$\eta_0 \sim \begin{cases} M, & M < M_\mathrm{c} \\ M^{3.4}, & M > M_\mathrm{c} \end{cases}$$
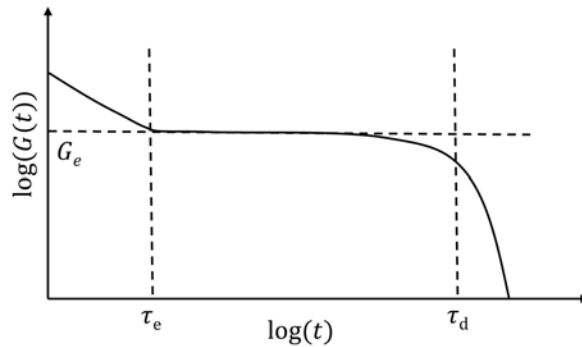
Figure 1.1: The typical relaxation modulus $G(t)$ of a well-entangled linear polymer melt after a step-strain.

Fig. 1.1 sketches the stress relaxation modulus of a linear polymer melt with $M \gg M_\mathrm{c}$. At short time scales, the stress relaxation moduli cannot be distinguished between different molecular weights. After a certain time τ_e, $G(t)$ for polymers with a large molecular weight barely decays, exhibiting a plateau with a M-independent modulus, G_e. Such plateau regime cannot be observed in low-M polymer systems, but is analogous to the plateau modulus of a cross-linked polymer network with a strand molecular weight M_e between the cross-links [12, 13]. The critical molecular weight M_c is approximately $2M_\mathrm{e}$ for all amorphous melts independent of their chemistry. After the plateau regime, $G(t)$ decays exponentially with the characteristic time τ_d which grows with M as $M^{3.4}$. It is well known that the remarkable difference in the rheological behaviours of linear melts with different molecular weights is attributed to "**entanglements**", which are essentially the topological interactions between neighboring polymers. In a melt of short-chain polymers, a probe chain diffuses freely as in a frictional fluid, whose dynamics could be well interpreted by the **Rouse model** [14]. In the long-chain polymer melts, the probe polymer chain feels the topological constraint, by which the chains cannot cross each other, thus lateral diffusion against such constraints is prohibited, leading to a drastic slowing down on diffusion.

The most successful theoretical framework for entangled polymers is the famous **tube model** originally proposed by de Gennes, Doi and Edwards [12, 13, 15–17], based on which theories for entangled dynamics have developed for half century, accounting for extensive experimental data. In the fundamental assumption of the tube model, the topological constraints imposed by surrounding chains act to confine the probe chain in a tube-like region. The contour line of the tube is called the **primitive path**, upon which the projected chain is called the **primitive chain**. The monomer diffusion perpendicular to the primitive path is restricted in the tube-like region with a diameter a. The chain can only diffuse curvilinearly along the primitive path at time scales longer than the entanglement time τ_e, which is the time taken by an entanglement segment to diffuse a distance of its own size a, i.e., the tube diameter. This type of diffusion is known as "**reptation**" [16]. "Reptation", which means "creeping" in Latin, represents the snake-like motion of a polymer chain in its own tube. On the length scales larger than the tube diameter a, reptation is equivalent to the one-dimensional diffusion of the primitive chain: the central sections of the chain follow the tube contour while the chain ends explore in the melt to create new tube segments. With very limited parameters, the original tube model successfully captures the qualitative features of entanglement dynamics of linear chains, but fails to provide quantitative predictions. For example, the predicted dependence of viscosity on molecular weight is $\eta_0 \sim M^{3.0}$ rather than the experimentally observed $M^{3.4}$. Such discrepancies arise from the oversimplified assumptions made in the original tube model, such as the inextensibility of the primitive chain.

In order to provide quantitative predictions, the tube model needs to be improved by incorporating additional relaxation modes, such as the **contour length fluctuation (CLF)** due to the fluctuations of tube length around the average value, and the **constraint release (CR)** due to the exchange of surrounding chains. In the picture of reptation plus CLF, Doi [18] deduced the 3.4 power law as well as the particular range it accounts for, which quantitatively predicted the experimen-

tal observation that the power law for very long chains would deviate from 3.4 to 3.0. The CR mechanism, which is extraordinarily important in polydisperse systems where the molecular weights of different species are significantly separated from each other, represents the effect brought by the exchange of the surrounding chains on the tube confinement. In a CR event, a probe chain is permitted to move transverse to the confining tube when some neighbouring chains move away by reptation or CLF. Graessley [6, 19] assumes that the exchange of the surroundings chains does not modify the tube diameter, but results in a rearrangement of tube segments of the probe chain. So the tube becomes a random walk and thus amounts to a Rouse-like motion, which is also referred to as the **constraint-release Rouse** (**CR Rouse**) motion. Cloizeaux [20] proposed a "**double-reptation**" approximation and inferred the stress relaxation modulus $G(t)$ as a quadratic function of the tube survival fraction $\mu(t)$. This "double-reptation" picture works best for the polydisperse systems with broad molecular weight distributions, but show limitation in binary blends of chains with greatly separated lengths. Rubinstein [21–23] considered the broad distribution of the CR rates, and proposed a self-consistent theory for binary blends, where the stress relaxation modulus $G(t)$ is in a product form of the tube survival fraction $\mu(t)$ and a Rouse-like relaxation function $R(t)$ of the tube representing the CR process. By incorporating CLF and CR, the tube model explained the additional stress relaxed at the reptation time of short chains in comparison with the pure reptation model. A quantitative tube theory for well-entangled linear chain systems was proposed by Likhtman and McLeish [24], who combined the main relaxation mechanisms in a self-consistent manner.

As anticipated, a simple change in the polymer architectures, such as adding a branch to a linear chain to create a 3-arm star polymer could completely change the dynamics. In a f-arm star polymer ($f \geq 3$), reptation is highly suppressed because entropically it is extremely unfavourable to drag $f - 1$ arms into one tube. Thus the branch point would be localized in a volume of tube diameter size before

the arms are relaxed by CLF and CR. In star polymers, the CLF mechanism is also termed as "**arm retraction**", in which the arm repeatedly retracts inwards along the primitive path toward the branch point to release original tube segment and stretches out to create new tube segments. de Gennes [25] indicated that arm retraction in a fixed network is an exponentially-rare event, whose probability was later calculated by Kuzzu and Doi [26]. Based on their works, Person and Helfand [27] presented a refined theory for arm retraction, which assumes the entropically unfavoured retraction is a thermally activated process in a quadratic potential field, $U(s) = \nu k_B T (M/M_e) s^2$, where s represents the relaxed fraction of the primitive path changing from zero to unity during the retraction, $\nu \approx 0.6$ is a numerical factor obtained by fitting experimental results. The Person-Helfand theory confirms the experimental observation that the viscosity of star polymers grows exponentially with the increasing molecular weight of the arm, M_a. However, the numerical factor $\nu \approx 0.6$ is in contrast to the CLF model which provides $\nu = 15/8$ [17].

Ball and McLeish [28] realized that the discrepancy in the value of ν can be attributed to the absence of CR mechanism in the Person-Helfand theory. By invoking a "tube-dilation" hypothesis [29], they proposed a well-known concept called "**dynamic tube dilation**" (**DTD**), which incorporates the CR mode into the tube model for branched polymers. The key assumption of DTD is that the relaxed arm segments could be treated as solvent for unrelaxed materials, such that the arm would retract in a gradually widening tube. The molecular weight of the dilated tube segment subjects to a dilation exponent α: $M_e(s) = M_{e0}(1 - s)^{-\alpha}$, where M_{e0} is the molecular weight of the undilated tube segment and α is either 4/3 or 1 whose exact value should depend on the physical nature of entanglements that is not yet fully resolved. When taking $\alpha = 1$, the effective potential $U_{eff}(s)$ is $(15/8)(M_a/M_e)k_B T (s^2 - 2s^3/3)$, which gives $\nu = 0.625$ at $s = 1$ in accordance with $\nu \approx 0.6$ in Person-Helfand theory. The DTD hypothesis is expected to work better for branched polymers due to the well-separated relaxation timescales. In the mean-

time, the continuous and smooth spectrum of relaxation time validates the gradual dilation ansatz. Milner and McLeish [30] developed a theory to predict the first-passage time of arm retraction by solving the Kramers problem [31] of a one-bead linked to the branch point by a harmonic spring. The solution gives the prefactor of the exponential function of the relaxation time $\tau(s)$:

$$\tau(s) \sim \tau_{\mathrm{e}} \left(\frac{M_{\mathrm{a}}}{M_{\mathrm{e}}} \right)^{3/2} \exp \left(U_{\mathrm{eff}}(s) \right)$$

where a scaling of $(M_{\mathrm{a}}/M_{\mathrm{e}})^{3/2}$ is found. Milner-McLeish theory also considers the early time fluctuations where the energy barrier is smaller than $k_{\mathrm{B}}T$, and formulates $\tau(s)$ into a crossover function of early to late timescales. The predictions of Milner-McLeish theory on the loss modulus modulus $G''(\omega)$ of symmetric star polymer melts are in good agreement with the experimental data for the whole range of frequency [32, 33]. Recently, Cao et al. [34] presented an analytical solution for arm retraction by solving it as a multi-dimensional first-passage time problem. By including all Rouse modes rather than only considering the slowest one as in Milner-McLeish theory, the relaxation time in the absence of CR is reduced by a factor of $2/M_{\mathrm{a}}$, implying a smaller prefactor for $\tau(s)$.

After the remarkable success on monodisperse symmetric stars, the Milner-McLeish model was then extended to other systems, such as star-linear blends [35] and asymmetric stars [36]. In a blend of monodisperse linear chains and stars, the DTD picture fails when the linear chains are fully relaxed by reptation at their terminal time τ_{d}, such that the tube diameter can not increase as fast as the decrease of unrelaxed materials in the system. Milner et al. [35] dealt with this problem by assuming three relaxation stages. In the early regime $t < \tau_{\mathrm{d}}$, the standard DTD model is applied by treating the linear chains as two-arm stars. After τ_{d}, the tube of star arms undergoes CR Rouse motion with a tube segmental relaxation time τ_{d}. The CR Rouse motion ends when the tube has explored the "supertube" defined by remaining entangled arm segments, after which the DTD picture resumes. In the simplest asymmetric stars consisting of one short arm and two long arms,

the terminal relaxation time of the short arm τ_s is much shorter than that of the long arm τ_l. Each time the short arm is fully retracted, the branch point is able to hop by a distance of a fraction of tube diameter pa with $p \leq 1$. Thus, at the time scales $t > \tau_s$, the short arm can be treated as effective frictional bead with a larger friction at the branch point, whose diffusion coefficient is estimated using Einstein relation: $D_b = p^2 a^2 / (2\tau_s)$ [36]. More recently, the Milner-McLeish theory has been generalized to model branched polymers with more complicated architectures, such as H-shaped, comb, Cayley tree polymers and their general mixtures [37–44]. Relaxation of these polymers proceeds hierarchically, starting from the retraction of the outermost branch arms and proceeding to inner layers until the core of the molecules. Under this frame, several computational models were developed for predicting viscoelastic properties of general mixtures of branched polymers with different architectures, including the hierarchical model by Larson et al. [39, 44, 45], the "bob" ("branch-on-branch") model by Das et al. [42] and the time marching algorithm by van Ruymbeke et al. [46–48]. These models differ in certain computational algorithms and relaxation mechanisms, but share similar theoretical framework that incorporates reptation, contour length fluctuation (or arm retraction), and constraint release by dynamic tube dilation or constraint-release Rouse motion. A detailed comparison between hierarchical model and "bob" model was carried out in Ref. [44].

Although tube-based theories have been shown to provide semi-quantitative predictions for rheological behaviours of various branched polymers, they are far from first-principle due to many mathematical and physical approximations involved. For example, the empirically fitting parameter p^2 which determines the fractional hopping distance of the branch point is found with a broad range from 1 to 1/60 for different asymmetric stars. For H-polymers, however, the range of p^2 is relatively narrow, roughly from 1/12 to 1/15 [36]. Whether the value of p^2 should be universal or system-dependent remains unknown. In star-linear blends, the DTD picture

would fail when the dilation speed is higher than the diffusion rate which the chain segments explore the tube. Before the DTD resumes, the confining tube of arms undergoes CR Rouse motion in a "supertube" [35]. In fact, arm retraction also happens in this intermediate regime, but how to handle it remains a question.

These open questions invariably point to the same origin: despite the concepts of entanglement and tube having been widely used in theoretical models for half century, there is still a lack of clear microscopic pictures about them. Computer simulations using a generic bead-spring polymer chain model, namely the **Kremer-Grest (KG) model** [49, 50] makes it possible to find the highly desired picture of entanglement and tube. One of the remarkable accomplishments was achieved by Everaers et al. [51]. They conducted a "**primitive-path analysis**" (**PPA**) to count the number of entanglements per chain and the average number of monomers in an entanglement strand, and thus predicted the plateau modulus comparable to experimental data. Recently, Likhtman and Ponmurugan [52] employed "**mean-path analysis**" [53] to trace the entanglements by constructing the "**contact map**" of chain segments, and got the lifetime distribution and the mean-square displacements of persistent binary contacts between neighbouring chains or entanglements. This algorithm has been applied by Cao and Wang to investigate the microscopic picture of constraint release in symmetric star polymer melts [54]. Likhtman [55] also proposed an algorithm to construct the "**tube axis**" for entangled polymers, whereby the binary and triple entanglements could be manifested through the smoothly averaged paths of the polymers. Likewise, the assumptions in tube theory that are necessarily empirical and speculative could be tested microscopically, such as the direct visualization of branch point hopping [56, 57].

In the past two decades, the **slip-link** or **slip-spring** models which work as alternative descriptions for entangled polymers have captured great attention. Different from the tube model that treats the topological constraints given by the surrounding chains in a mean-field way, this class of models assume the entanglements as

binary interactions between neighbouring chain segments, and thus can incorporate more refinements, such as the discrete description of entanglements that distribute along the chains with a wide range of lifetimes. The "slip-link" picture was first proposed by Doi [58] in his **slip-link network model**, where each slip-link represents an entanglement, and the release of an entanglement occurs only when either ends of the two individual chains passes through the slip-link to destroy it. The later slip-link based models, without exception, follow the primary picture of Doi's model, but differ in modeling and algorithms. Schieber et al. [59–61] developed a single-chain slip-spring model, in which each slip-link represents an entanglement whose dynamics is governed by a stochastic equation that exchanges the number of monomers between neighbouring entanglement strands. The rheological properties can thus be obtained by tracking the location of slip-links and number of monomers along each entangled strand in between two adjacent slip-links. Shanbhag and Larson [62, 63] developed a multi-chain slip-link model by simulating an ensemble of primitive chains. In this slip-link model, the entanglements are modeled by pairing the slip-links on different chains, whereby the constraint release is incorporated naturally by destroying the slip-link pairs when either of them escapes the ends of involved chains by primitive path fluctuation or reptation. The multi-chain slip-link model developed by Masubuchi et al. [64, 65] simulates the primitive chains bundled by slip-links that form a 3D network, whereby this model is called **primitive chain network** (**PCN**) model (also implemented in the **NAPLES** code). The motion of the slip-links is governed by the force balance between entanglement strands, while the diffusion of the monomers along each chain contour is operated according to the tension distribution along the chain. The slip-link based model developed by Likhtman [66] is called **slip-spring model** due to the slip-links are connected to a set of virtual springs anchored in space, which provides extra fluctuation to the location of entanglements. The polymer chains are modeled as Rouse chains, whose primitive paths are defined by the slip-links sitting on the monomers. The contour length fluc-

tuation is incorporated by the Rouse motion of the chains confined in the slip-links, while the constraint release is included in a similar way as other slip-link models. Based on the slip-spring model and the primitive chain network model, Langeloth el al. [67] recently developed another slip-spring model which employs **dissipative particle dynamics** (**DPD**) to simulate a 3D chain network. This model is built on a finer level by incorporating excluded volume as non-bonded interaction, but in return requires much large system and expensive computational cost.

The aim of this thesis is to study the relaxation dynamics of branched polymers with the simplest architectures, such as star and H-polymers, on which a complete set of observables predicted by tube theories have been compared with experiments. Efficient methodology to investigate the arm-retraction dynamics of well entangled branched polymers would be developed to examine existing tube-based theories, such as the Milner-McLeish theory on arm retraction dynamics [30, 34]. We will also explore the possibility of extending the slip-spring model to branched polymers. Despite its success on describing linear polymers, the slip-spring model encounters difficulty in extending its applications to branched polymers. The problem may lie in the absence of certain relaxation mechanisms close to the branch point, which could possibly be resolved by incorporating the hypothesis in tube theory for asymmetric stars, i.e., the fully retracted short arm allows the reptation of other two long arms. Such attempt can reversely verify the tube theory for polymers with different architectures.

The content of this thesis is arranged as follows. In the remaining part of this chapter, we will introduce the theoretical background of polymer dynamics. In the second chapter, we investigate two advanced numerical methods, namely **forward flux sampling** (**FFS**) [68] and **weighted ensemble** (**WE**) [69, 70] method, and their applications on the multi-dimensional first-passage time problem of arm retraction of star polymers. The FFS simulation results are compared with theoretical predictions from both one-dimensional and multi-dimensional solutions of arm re-

traction dynamics. In the third chapter, a combinational method of FFS and the slip-spring model is implemented to investigate the dynamics of arm-retraction in star polymers. With a controllable precision, this method allows direct comparison between the slip-spring model and the tube theory for well-entangled star polymers of arm length up to 16 entanglements. Moreover, a study is conducted on the extraction of experimentally measurable observables from FFS simulations, such as the end-to-end relaxation and stress relaxation functions. We believe this work will not only expand the application of FFS method to polymer dynamics by reproducing full dynamic spectrum rather than just the first-passage time, but also to many other scientific areas. In the fourth chapter, we present a multi-scale computer simulation study on the relaxation dynamics of various branched polymers, including symmetric and asymmetric stars, and H-polymers. The slip-spring model is updated for branched polymers by incorporating a parameter free mechanism, whose results are compared with the fully flexible Kramer-Grest model [49]. The conclusions are given in the last chapter.

1.2 Polymer Chain Models

This section introduces the static properties of polymers by focusing on the single-chain conformation. By comparing the static properties of the ideal chain and the real chain, the fundamental concept of "universality" on chain conformation is concluded.

1.2.1 Ideal Chains

Consider a chain formed by $n + 1$ monomers that are connected in sequence via n bonds, as shown in Fig. 1.2. If the monomers several bonds apart do not interact with each other, this chain is called **ideal chain**. For example, in an ideal chain, there is no interaction between monomer i and monomer $i + j$ ($j \gg 1$), even though
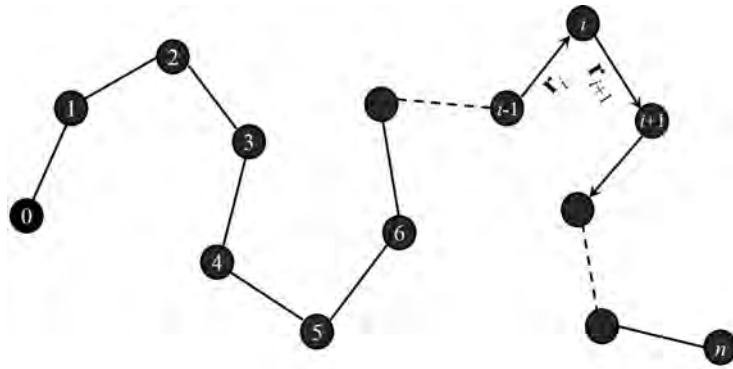
Figure 1.2: Freely jointed chain model.
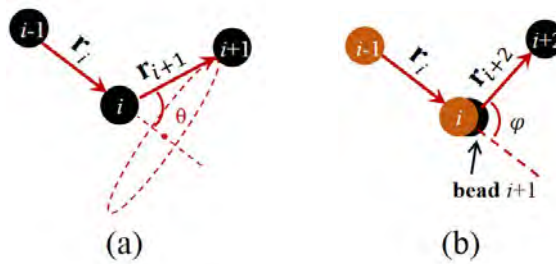
Figure 1.3: (a) Freely rotating chain model; (b) Hindered rotation model.

they might be very close in space. The simplest ideal chain model is the **freely jointed chain model**, in which the bond length is fixed while the orientation of bonds is random. Based on this model, more features could be included to resemble the polymer chains. For example, the orientational priority of the bonds can be introduced by fixing the bond angle θ, which is called the **freely rotating chain model** (Fig. 1.3(a)). Likewise, a torsion potential $U(\varphi)$ could be introduced to represent the steric hindrance between functional groups, which is called the **hindered rotation model** (Fig. 1.3(b)).

An important quantity to characterize the static property of a polymer chain is the **end-to-end vector**, $\mathbf{R}_{\mathrm{e}}$, which is the vector between the end beads, $\mathbf{R}_{\mathrm{e}} = \mathbf{r}_n - \mathbf{r}_0$ or the sum of the bond vectors, $\mathbf{R}_{\mathrm{e}} = \sum_{i=1}^{n} \mathbf{r}_i$. For an ideal chain that is long enough,

the average end-to-end vector $\langle \mathbf{R}_e \rangle$ is zero, but the average mean-square end-to-end distance is non-zero:

$$\langle \mathbf{R}_e^2 \rangle \cong C_\infty n l^2 \tag{1.1}$$

where l is the bond length, C_∞ is called **Flory's characteristic ratio** that determines the local stiffness of the chain. C_∞ for different models are listed as below:

Freely Jointed Chain Model	$C_\infty = 1$
Freely Rotating Chain Model	$C_\infty = \dfrac{1 + \cos\theta}{1 - \cos\theta}$
Hindered Rotation Model	$C_\infty = \left(\dfrac{1 + \cos\theta}{1 - \cos\theta} \right) \left(\dfrac{1 + \langle\cos\varphi\rangle}{1 - \langle\cos\varphi\rangle} \right)$

Eq. 1.1 indicates a universal property of the ideal chains: the models having various stiffnesses show similar behaviors at length scales larger than $C_\infty l$. Coarse-graining C_∞ monomers into one monomer, these ideal chains are equivalent to a freely jointed chain with N bonds:

$$\langle \mathbf{R}_e^2 \rangle \cong N b^2, \quad N = n/C_\infty, \quad b = C_\infty l.$$

where the length b is called **Kuhn length**.

1.2.2 Entropic Elasticity

Consider a freely jointed chain with $N + 1$ monomers. The N bonds connecting these monomers have a fixed bond length b. The conformation of the chain can be visualised as a 3D random walk with a constant step length b. In each direction, the 3D random walker could be decomposed into 1D random walk, whose mean-square step length is $b^2/3$. Such 1D random walk follows an **Ornstein-Uhlenbeck** process, thus the end-to-end distance of the chain in each direction follows Gaussian distribution:

$$P_{1d}(N, R_{e,\alpha}) = \sqrt{\frac{3}{2\pi N b^2}} \exp\left(-\frac{3 R_{e,\alpha}^2}{2 N b^2} \right),$$

where α is the Cartesian component. Therefore, the end-to-end vector $\mathbf{R}_e$ of an ideal chain also follows Gaussian distribution, which is a product of the 3 components:

$$P_{3d}(N, \mathbf{R}_e) = P_{1d}(N, R_{e,x})P_{1d}(N, R_{e,y})P_{1d}(N, R_{e,z}) = \left(\frac{3}{2\pi Nb^2}\right)^{3/2} \exp\left(-\frac{3\mathbf{R}_e^2}{2Nb^2}\right).$$

$$(1.2)$$

The distribution above indicates that the free chain is keen to collapse into coil with a *zero* end-to-end vector (chain ends tend to overlap). If the chain is stretched with an end-to-end vector of $\mathbf{R}_e$, the free energy F increases by

$$\Delta F = F(N, \mathbf{R}_e) - F(N, \mathbf{0}) = -T\Delta S = -k_BT\left(\ln\Omega(N, \mathbf{R}_e) - \ln\Omega(N, \mathbf{0})\right),$$

where S is the entropy, k_B is the Boltzmann constant, $\Omega(N, \mathbf{R}_e)$ is the number of the states with end-to-end vector equal to $\mathbf{R}_e$. Then the statistical weight of the conformations with the end-to-end vector equal to $\mathbf{R}_e$ is given by

$$P_{3d}(N, \mathbf{R}_e) = \frac{\Omega(N, \mathbf{R}_e)}{\int \Omega(N, \mathbf{R}_e)d\mathbf{R}_e}.$$

Then we have,

$$\ln\Omega(N, \mathbf{R}_e) = \ln(P_{3d}(N, \mathbf{R}_e)) + Const = -\frac{3}{2}\frac{\mathbf{R}_e^2}{Nb^2} + Const.$$

Therefore, the increase of the free energy ΔF is a quadratic function:

$$\Delta F = \frac{3}{2}\frac{k_BT}{Nb^2}\mathbf{R}_e^2,$$

$$(1.3)$$

which is effectively equal to a harmonic spring with an elastic constant $3k_BT/Nb^2$. The elasticity of a ideal chain due to the change of the entropy is called **entropic elasticity**.

1.2.3   Real Chain

Different from the ideal chains, a real chain has long-range interactions, which means that two monomers in one chain can interact even if they are chemically well-separated by many bonds. Such interactions can be evaluated by the **excluded**

volume, which is the negative integral of the **Mayer f-function**:

$$f(r) = \exp\left(-\frac{U(r)}{k_{\mathrm{B}}T}\right) - \exp\left(-\frac{0}{k_{\mathrm{B}}T}\right) = \exp\left(-\frac{U(r)}{k_{\mathrm{B}}T}\right) - 1,$$

where $U(r)$ is the potential between two monomers with a distance of r. According to this equation, the Mayer f-function describes the difference between the Boltzmann factors of two potential fields: one is $U(r)$, the other is $U(r) = 0$ as $r \to \infty$. The excluded volume v is an integral of $f(r)$ over the whole space,

$$v = -\int f(r)\mathrm{d}^3 r = \int \exp\left(-\frac{0}{k_{\mathrm{B}}T}\right) \mathrm{d}^3 r - \int \exp\left(-\frac{U(r)}{k_{\mathrm{B}}T}\right) \mathrm{d}^3 r.$$

Therefore, the excluded volume is a quantity that determines whether the net interaction between two monomers is attractive($v < 0$) or repulsive($v > 0$).

In polymer solvent, the interaction between monomers is affected by the solvent molecules. When the monomers like to stay with the solvent molecules more than with each other, v is positive and thus this solvent is called "good" solvent. When the monomers are more likely to stay with each other, v is negative and thus the solvent is called "poor" solvent. When $v = 0$, the state is called "θ-state" and the solvent is called "θ-solvent". In a polymer melt, the polymers are the θ-solvent of themselves, because the monomers cannot distinguish which polymer chain they come from. Therefore, the static properties of the polymer chains in melts can be evaluated by the same scaling of ideal chains. Our discussions throughout the thesis will be restricted to the melt state.

1.2.4   Gaussian Chain

Since the end-to-end vector of the ideal chain follows Gaussian distribution, one can also conclude that the distribution of the vector between monomers i and j also follows Gaussian, as long as the chain segment length between them is much longer than the Kuhn length b. It seems that the freely jointed chain model is already good enough to give the static properties of flexible polymers in melt state. But this
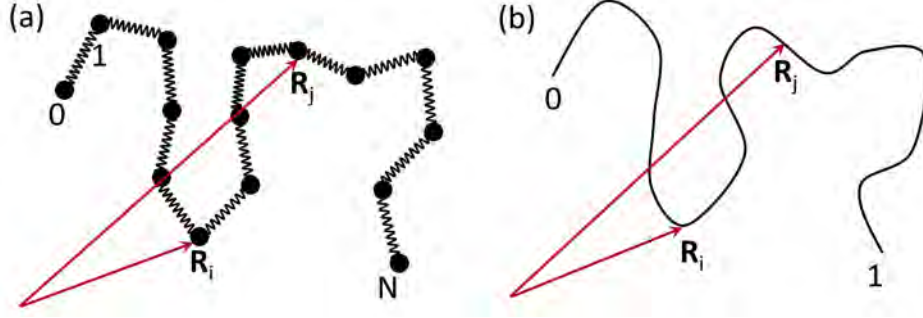
Figure 1.4: The discrete (a) and continuous (b) Gaussian chain model.

model is not the simplest in mathematics. The simplest model is called **Gaussian chain model**, which assumes the chain follows Gaussian distribution over all length scales.

The discrete Gaussian chain model is shown in Fig. 1.4(a). $N + 1$ beads are connected by N harmonic springs, whose potential is given by

$$U_{\text{bond}}(\mathbf{R}_{i+1} - \mathbf{R}_i) = \frac{3k_{\text{B}}T}{2b^2}(\mathbf{R}_{i+1} - \mathbf{R}_i)^2, \qquad i = 0, 1...N$$

The vector between any two monomers also follows Gaussian distribution

$$P(i - j, \mathbf{R}_i - \mathbf{R}_j) = \left(\frac{3}{2\pi|i - j|b^2}\right)^{3/2} \exp\left(-\frac{3(\mathbf{R}_i - \mathbf{R}_j)^2}{2|i - j|b^2}\right).$$

This notation can be written into a continuous formula, in which $\mathbf{R}_i - \mathbf{R}_{i-1}$ is replaced by $\partial\mathbf{R}_n/\partial n$, where n ranging from 0 to 1 is the coordinate of the points on the continuous chain (Fig. 1.4(b)). Then the last equation can be written as

$$P[\mathbf{R}_n] = C \exp\left(-\frac{3}{2b^2}\int_0^N dn \left(\frac{\partial\mathbf{R}_n}{\partial n}\right)^2\right), \tag{1.4}$$

where C is a constant.

1.3 Observables for Polymer Dynamics

In this section, we will introduce a few observables to describe the relaxation dynamics for linear rheology.

1.3.1 Stress Relaxation

One important observable to describe the relaxation dynamics is the stress tensor [17]. To define the stress tensor of a homogeneous system, one can consider a volume V, which is divided by a hypothetical plane perpendicular to β-axis. The boundary of the volume along β-axis is 0 and L. The stress tensor $\sigma_{\alpha\beta}$ is the component of force per unit area on the plane (α-axis is orthogonal to β-axis and thus parallel to the hypothetical plane):

$$\sigma_{\alpha\beta} = \frac{\langle F_\alpha \rangle}{A} = \frac{1}{AL} \int_0^L dh \, \langle F_\alpha(h) \rangle \,,$$

where A is the area of the plane, and the angular bracket is the ensemble average, the force F_α is force which the upper part exerts on the lower part through the plane. Defining X_α as the integral for $F_\alpha(h)$, we have

$$X_\alpha = \int_0^L dh \, \langle F_\alpha(h) \rangle = \sum_{n,m} \left\langle F_{mn\alpha} \int_0^L dh \Theta(h - R_{m\beta})\Theta(R_{n\beta} - h) \right\rangle,$$

where $F_{mn\alpha}$ is the component force along α-axis that monomer n exerts on monomer m, $R_{m\beta}$ is the coordinate of monomer m on β-axis, h is the coordinate of the plane along β-axis, $\Theta(x)$ is the Heaviside step function which restricts that the hypothetical plane must be in the between of monomer m and n. Since the integral is non-zero only when the hypothetical force is in the middle of monomer m and n, the last equation could be written as

$$X_\alpha = \left\langle \sum_{m,n} F_{mn}^\alpha \left(R_{n\beta} - R_{m\beta} \right) \Theta \left(R_{n\beta} - R_{m\beta} \right) \right\rangle.$$

Exchanging m and n, and using Newton's third law: $F_{mn\alpha} = -F_{nm\alpha}$, we have

$$X_\alpha = \left\langle \frac{1}{2} \sum_{m,n} F_{mn\alpha} \left(R_{n\beta} - R_{m\beta} \right) \left[\Theta \left(R_{n\beta} - R_{m\beta} \right) + \Theta \left(R_{m\beta} - R_{n\beta} \right) \right] \right\rangle$$

$$= \left\langle -\frac{1}{2} \sum_{m,n} F_{mn\alpha} \left(R_{m\beta} - R_{n\beta} \right) \right\rangle$$

Defining $\mathbf{F}_m$ as the sum of the forces acting on monomer m: $\mathbf{F}_m = \sum_n \mathbf{F}_{mn}$, the stress tensor of a homogeneous polymer melt is given by

$$\sigma_{\alpha\beta} = \frac{1}{AL} \left\langle -\frac{1}{2} \sum_{m,n} F_{mn\alpha} R_{m\beta} + \frac{1}{2} \sum_{m,n} F_{mn\alpha} R_{n\beta} \right\rangle = -\frac{1}{V} \left\langle \sum_m F_{m\alpha} R_{m\beta} \right\rangle,$$

After a small step strain γ_0 along x axis, in xy plane the stress relaxes in the form of

$$\sigma_{xy}(t) = \gamma_0 G(t),$$

where $G(t)$ is so-called **stress relaxation modulus** or **stress relaxation function**. In experiments, $G(t)$ can be easily measured by rheometer with oscillating mode, where the oscillating strain changes with time, $\gamma_{(t)} = \gamma_0 \sin(\omega t)$, where ω is the frequency of oscillation. The stress response due to elasticity is instantaneous to the strain, and thus the in-phase response is called **storage modulus** $G'(\omega)$. The stress response due to viscosity is proportional to the shear rate, and the out-of-phase response is called **loss modulus** $G''(\omega)$. $G'(\omega)$ and $G''(\omega)$ are respectively sine and cosine Fourier transform of $G(t)$:

$$G'(\omega) = \omega \int_0^\infty \sin(\omega t) G(t) dt; \quad G''(\omega) = \omega \int_0^\infty \cos(\omega t) G(t) dt. \qquad (1.5)$$

In experiments, $G'(\omega)$ and $G''(\omega)$ are useful to characterize the relaxation regimes. In computer simulation, it is easy to measure $G(t)$. According to the **fluctuation-dissipation theorem** [71, 72], the response of a system in thermodynamic equilibrium to a weak external field (e.g., magnetic and electric field) is the same as its response to a spontaneous fluctuation, and the change of a physical quantity is a linear function of the field. Using the fluctuation-dissipation theorem, $G(t)$ of an isotropic system is given by

$$G(t) = \frac{V}{k_B T} \left\langle \sigma_{\alpha\beta}(t) \sigma_{\alpha\beta}(0) \right\rangle, \qquad (1.6)$$

where the angular brackets indicates ensemble average, α and β are any two orthogonal directions and $G(t)$ is averaged over all pairs of α and β.

1.3.2 End-to-End Vector Relaxation

In computer simulation, the end-to-end vector relaxation function of a polymer chain can be easily calculated by the autocorrelation function:

$$\Phi(t) = \frac{\langle \mathbf{R}_{\mathrm{e}}(t) \cdot \mathbf{R}_{\mathrm{e}}(0) \rangle}{\langle \mathbf{R}_{\mathrm{e}}(0)^2 \rangle}$$

In experiments, $\mathbf{R}_{\mathrm{e}}$ of the polymers whose molecular dipoles are parallel to backbone can be directly measured by **dielectric spectroscopy** [8]. By applying an external electric field, the polymer would be polarized. For each chain, the sum of the molecular dipoles is equal to the induced polarization $\mathbf{P}(t)$, which is proportional to end-to-end vector $\mathbf{R}_{\mathrm{e}}(t)$. Therefore, the end-to-end vector relaxation is given by

$$\Phi(t) = \frac{\langle \mathbf{P}(t) \cdot \mathbf{P}(0) \rangle}{\langle \mathbf{P}(0)^2 \rangle}. \tag{1.7}$$

1.3.3 Mean-Square Displacement

Mean-square displacement (MSD) is a quantity to describe the diffusion of particles. The mean-square displacement of monomer i is given by

$$g_1(i,t) = \left\langle \left(\mathbf{R}_i(t) - \mathbf{R}_i(0) \right)^2 \right\rangle. \tag{1.8}$$

The center-of-mass mean-square displacement is given by

$$g_3(t) = \left\langle \left(\mathbf{R}_{\mathrm{cm}}(t) - \mathbf{R}_{\mathrm{cm}}(0) \right)^2 \right\rangle,$$

which is widely measured in experiments to give diffusion coefficient of the chain [73, 74].

1.4 Rouse Model

The Rouse model provides analytical solutions for almost all observables in unentangled polymer melts. In this section, we will introduce the analytical solution for the relaxation time of the Rouse model, which is related to the discussion in chapter 2. For other quantities, their scaling behaviours will be briefly introduced.

1.4.1 Rouse Chain

The schematic plot of the **Rouse chain** is identical to the discrete Gaussian chain as shown in Fig. 1.4(a). Consider a chain with $N + 1$ beads that are connected by N harmonic springs of an average bond length b. The potential of the chain U_r is the sum of the free energies of the springs

$$U_\mathrm{r}\left(\mathbf{R}_0 \ldots \mathbf{R}_N\right) = \frac{3k_\mathrm{B}T}{2b^2} \sum_{i=0}^{N-1} \left(\mathbf{R}_{i+1} - \mathbf{R}_i\right)^2. \tag{1.9}$$

In melt state, the non-bonded interaction applied to a given monomer due to the collision of surrounding particles could be represented by a random force satisfying

$$\langle \mathbf{f}_i(t) \rangle = 0, \quad \langle f_{i\alpha}(t) f_{j\beta}(t') \rangle = 2k_\mathrm{B}T\xi\delta_{ij}\delta_{\alpha\beta}\delta\left(t - t'\right).$$

where i and j are the monomer index, α and β are the Cartesian components, and ξ is the friction coefficient of the beads. Then the equation of motion of the monomer i is given by

$$m\frac{\mathrm{d}^2\mathbf{R}_i}{\mathrm{d}t^2} = -\frac{\partial U\left(\mathbf{R}_0, \ldots, \mathbf{R}_N\right)}{\partial \mathbf{R}_i} - \xi\frac{\mathrm{d}\mathbf{R}_i}{\mathrm{d}t} + \mathbf{f}_i(t).$$

In an "overdamped" system, the left term of the above equation can be neglected, giving the Langevin or stochastic equation:

$$\xi\frac{\mathrm{d}\mathbf{R}_i}{\mathrm{d}t} = -\frac{\partial U\left(\mathbf{R}_0, \ldots, \mathbf{R}_N\right)}{\partial \mathbf{R}_i} + \mathbf{f}_i(t). \tag{1.10}$$

1.4.2 Rouse Modes

In matrix notation, the Langevin equation for all monomers can be combined into a simple equation:

$$\xi\frac{\mathrm{d}\mathbf{R}_i}{\mathrm{d}t} = -\frac{3k_\mathrm{B}T}{b^2} \sum_{j=0}^{N} A_{ij}\mathbf{R}_j + \mathbf{f}_i(t). \tag{1.11}$$

A_{ij} is a N-order **connectivity matrix**,

$$
A = \begin{pmatrix}
1 & -1 & . & . & & & & \\
-1 & 2 & -1 & . & & & & \\
. & . & . & . & . & . & . \\
& & & . & 2 & -1 & . \\
& & & . & -1 & 2 & -1 \\
& & & . & . & -1 & 1
\end{pmatrix},
$$

where only the non-zero elements are presented. It is difficult to directly give a analytical solution for Eq. 1.11, because the motion of the monomers are correlated with their neighbours. But some independent behaviours could be decomposed. These behaviours are coherent on certain length scales. For example, the mechanical wave on an oscillated string is a coherent motion of the points on the string, which could be described by a cosine function. On a chain, similar coherent motions can be extracted by diagonalizing the matrix A_{ij}. Hence the equations of motion are transformed to the normal coordinates

$$
\xi_p \frac{\mathrm{d}\mathbf{X}_p}{\mathrm{d}t} = -k_p \mathbf{X}_p + \mathbf{f}_p(t), \quad p = 0 \dots N, \tag{1.12}
$$

where $\mathbf{X}_p$ defines the coherent motion of a chain section of length N/p and is called **Rouse mode**, which is a function of $\mathbf{R}_i$,

$$
\mathbf{X}_p = \frac{1}{N+1} \sum_{i=0}^{N} \mathbf{R}_i \cos\left(\frac{\pi p(i+1/2)}{N+1}\right). \tag{1.13}
$$

The dynamics of each mode is equivalent to the diffusion in a quadratic potential field. The elastic coefficient of the potential field k_p and the effective friction coefficient ξ_p are respectively given by

$$
k_p = \begin{cases}
0 & (p = 0) \\
\dfrac{24k_{\mathrm{B}}T(N+1)}{b^2} \sin^2\left(\dfrac{\pi p}{2(N+1)}\right) & (p = 1, \dots, N)
\end{cases} \tag{1.14}
$$

and

$$\xi_p = \begin{cases} (N+1)\xi & (p=0) \\ 2(N+1)\xi & (p=1\ldots N) \end{cases} \tag{1.15}$$

The inverse transform from $\mathbf{X}_p$ to monomer coordinate is given by

$$\mathbf{R}_i = \mathbf{X}_0 + 2\sum_{p=1}^{N} \mathbf{X}_p \cos\left(\frac{\pi p\,(i+1/2)}{N+1}\right) \tag{1.16}$$

For a Rouse chain, $\mathbf{X}_p$ is a sum of cosine functions whose wave length varies in respect of p (See Eq. 1.13,). Apart from $\mathbf{X}_0$ which represents the diffusion of the center of mass, other modes represent the coherent motion of a chain section containing N/p monomers. For example, $\mathbf{X}_1$ describes the relaxation over the whole chain length.

1.4.3 Relaxation Times

Eq. 1.12 is a **stochastic differential equation (SDE)** of a Ornstein-Uhlenbeck process,

$$\xi_p \mathrm{d}\mathbf{X}_p = -k_p\mathbf{X}_p\mathrm{d}t + \sqrt{2k_\mathrm{B}T\xi_p}\mathrm{d}\mathbf{W},$$

where T is the temperature, and $\mathbf{W}$ is a **Wiener process**. The solution of this SDE is

$$\mathbf{X}_p(t) = \mathbf{X}_p(0)\exp\left(-t/\tau_p\right) + \sqrt{2D_p}\int_0^t \exp\left(-\frac{t-t'}{\tau_p}\right)\mathrm{d}\mathbf{W}',$$

$$\tau_p = \xi_p/k_p, \qquad D_p = \frac{k_\mathrm{B}T}{\xi_p}. \tag{1.17}$$

The autocorrelation function of $\mathbf{X}_p$ is

$$\langle X_{p\alpha}(t)X_{q\beta}(t')\rangle = \delta_{pq}\delta_{\alpha\beta}\langle X_{p\alpha}(0)X_{p\beta}(0)\rangle \exp\left(-\frac{t+t'}{\tau_p}\right)$$

$$+D_p\tau_p\left(\exp\left(-\frac{|t-t'|}{\tau_p}\right) - \exp\left(-\frac{t+t'}{\tau_p}\right)\right) \tag{1.18}$$

Let $t' = 0$ and $t > 0$, it becomes

$$\langle X_{p\alpha}(t)X_{q\beta}(0)\rangle = \delta_{pq}\delta_{\alpha\beta}\langle X_{p\alpha}(0)X_{q\beta}(0)\rangle \exp\left(-\frac{t}{\tau_p}\right); \quad \langle X_{p\alpha}^2\rangle = D_p\tau_p = \frac{k_{\mathrm{B}}T}{k_p}.$$

$$(1.19)$$

Thus τ_p is the characteristic time or relaxation time of Rouse mode p. According to Eqs. 1.14, 1.15 and 1.17, τ_p is given by

$$\tau_p = \frac{\xi b^2}{12k_{\mathrm{B}}T}\sin^{-2}\left(\frac{\pi p}{2(N+1)}\right) \approx \frac{\xi b^2 N^2}{3\pi^2 k_{\mathrm{B}}Tp^2}. \tag{1.20}$$

The relaxation time for the slowest mode is the so-called **Rouse time**,

$$\tau_{\mathrm{R}} \equiv \tau_1 = \frac{\xi b^2}{12k_{\mathrm{B}}T}\sin^{-2}\left(\frac{\pi}{2(N+1)}\right) \approx \frac{\xi b^2 N^2}{3\pi^2 k_{\mathrm{B}}T}. \tag{1.21}$$

For the fastest mode, the relaxation time is

$$\tau_N = \frac{\xi b^2}{12k_{\mathrm{B}}T}\sin^{-2}\left(\frac{\pi N}{2(N+1)}\right) \approx \frac{\xi b^2}{12k_{\mathrm{B}}T}. \tag{1.22}$$

In the qualitative discussion on scaling behaviours [75], it is also common to use τ_0 to denote the fastest mode,

$$\tau_0 = \frac{\tau_{\mathrm{R}}}{N^2}, \tag{1.23}$$

which is in fact 2.5 times smaller than τ_N.

1.4.4 Monomer Mean-Square Displacement

When $p = 0$, the solution of Eq. 1.17 gives the center of mass mean-square displacement of the chain:

$$g_{1,\mathrm{mass}}(t) = \langle(\mathbf{X}_0(t) - \mathbf{X}_0(0))^2\rangle = \frac{6k_{\mathrm{B}}Tt}{(N+1)\xi}.$$

This equation simply follows the **Einstein-Smoluchowski relation**, thus the whole chain could be visualized as an effective Brownian particle with a diffusion coefficient $D \approx k_{\mathrm{B}}T/N\xi$.

The monomer mean-square displacement, $g_1(t)$, is more complicated. At the time scales $t < \tau_0$, the monomers are not aware of that they are part of a chain, thus

experiencing free diffusion. After τ_0, the monomers follow Rouse motion. According to Eqs. 1.20 and 1.23, the relaxation time for a Rouse mode τ_p can be written as

$$\tau_p = \left(\frac{1}{p}\right)^2 \tau_R = \left(\frac{N}{p}\right)^2 \tau_0.$$

During τ_p, the monomers on average move a distance of the order of $(N/p)b^2$, which is the mean-square size of the sections containing N/p monomers. Substituting t for τ_p, we have

$$p = \left(\frac{\tau_R}{t}\right)^{1/2} = N\left(\frac{\tau_0}{t}\right)^{1/2}, \tag{1.24}$$

which means, at the time scale t, the index of relaxed modes must be higher than p. The monomer mean-square displacement is of the order of the mean-square size of the section involved in the coherent motion at this time scale:

$$g_1(t) \approx \left(\frac{t}{\tau_0}\right)^{1/2} b^2 \qquad (\tau_0 < t < \tau_R). \tag{1.25}$$

For $t > \tau_R$, the monomer follows free diffusion, the mean-square displacement is linear in time. In summary, $g_1(t)$ for Rouse model has 3 regimes:

$$g_1(t) \sim \begin{cases} t, & t < \tau_0 \\ t^{1/2}, & \tau_0 < t < \tau_R \\ t, & t > \tau_R \end{cases} \tag{1.26}$$

1.4.5 Stress Relaxation and Viscosity

After a step-strain, each unrelaxed mode contributes the energy of the order of $k_B T$ to the stress relaxation modulus. Therefore, at the time scales $\tau_0 < t < \tau_R$, the stress relaxation modulus $G(t)$ is proportional to the number density of sections with N/p monomers at time τ_p, where p is given by Eq. 1.24, leading to

$$G(t) \approx \frac{\phi}{Nb^3} k_B T p = \frac{\phi}{b^3} k_B T \left(\frac{t}{\tau_0}\right)^{-1/2} \qquad (\tau_0 < t < \tau_R), \tag{1.27}$$

where ϕ is the polymer volume fraction, $G(t)$ decays with the time as $t^{-1/2}$. The analytical solution of $G(t)$ for a long chain is given by

$$G(t) = \frac{\phi k_B T}{Nb^3} \sum_{p=1}^{\infty} \exp\left(-\frac{2t}{\tau_p}\right).$$

According to this equation, we can estimate the power laws in the short and terminal regimes. At the time scales shorter than τ_0, the fastest mode has not yet fully relaxed. According to the expansion of single exponential, $e^{-2t/\tau_0} \approx 1 - t/(2\tau_0)$, the early relaxation shows linear decay, $G(t) \sim 1 - t/(2\tau_0)$. Beyond the longest relaxation time τ_R, the stress relaxation modulus has a single-exponential decay:

$$G(t) \approx \frac{\phi k_B T}{N b^3} \exp\left(-\frac{2t}{\tau_R}\right) \qquad (t > \tau_R).$$

In summary, there are 3 regimes in the stress relaxation function of Rouse chain:

$$G(t) \sim \begin{cases} 1 - \dfrac{t}{2\tau_N}, & t < \tau_0 \\ \quad t^{-1/2}, & \tau_0 < t < \tau_R, \\ \dfrac{1}{N} \exp(-2t/\tau_R), & t > \tau_R \end{cases} \qquad (1.28)$$

The viscosity of the Rouse chain can be calculated from the time integral of $G(t)$:

$$\eta_0 = \int_0^\infty G(t)dt = \frac{\phi \tau_R}{2N b^3} k_B T \sum_{p=1}^{N} \frac{1}{p^2} = \frac{\phi \xi}{36 b} N,$$

which explains the linear relationship between viscosity η_0 and molecular weight M for unentangled polymers.

1.4.6   End-to-End Vector Relaxation

The analytical solution of the End-to-end vector correlation function is derived using the inverse transform of Rouse mode (see Eq. 1.16), and the end-to-end vector is

$$\mathbf{R}_e = \mathbf{R}_N - \mathbf{R}_0 = -4 \sum_{p=1,\text{odd}}^{N} \cos\left(\frac{\pi p}{2(N+1)}\right) \mathbf{X}_p.$$

Substituting this equation into Eq. 1.7, the correlation function becomes

$$\Phi(t) = \frac{2}{N(N+1)} \sum_{p=1,\text{odd}}^{N} \tan^{-2}\left(\frac{\pi p}{2(N+1)}\right) \exp\left(-\frac{t}{\tau_p}\right).$$

Since $\sum_{p=1,\mathrm{odd}}^{N} \tan^{-2}\left(\pi p/2(N+1)\right) = N(N+1)/2$, this function would start from 1. $\Phi(t)$ also has 3 regimes:

$$\Phi(t) = \begin{cases} 1 - \dfrac{6k_{\mathrm{B}}T}{\xi N b^2}t & t < \tau_0 \\[2ex] 1 - \dfrac{4}{\pi^{3/2}}\sqrt{\dfrac{t}{\tau_{\mathrm{R}}}} & \tau_0 < t < \tau_{\mathrm{R}} \\[2ex] \dfrac{8}{\pi^2}\exp\left(-\dfrac{t}{\tau_{\mathrm{R}}}\right) & t > \tau_{\mathrm{R}}. \end{cases} \tag{1.29}$$

From $t = 0$ to τ_0, $\Phi(t)$ decays from 1 to $1 - 1/(2N)$, this early time decay is hard to observe when $N \gg 1$. Therefore, unlike the stress relaxation modulus $G(t)$, $\Phi(t)$ is not sensitive to early time relaxation.

1.5   Tube Model

In this part, we will introduce the tube model. This model originated from the study of rubber elasticity [12, 15], then was expanded to uncrosslinked systems by de Gennes [16], and formulated by Doi and Edwards [17]. Afterwards, theories for entangled polymers have been for half century primarily based on the tube model, which is considered as one of the most successful models in polymer dynamics.

1.5.1   Mean-field Tube

The diffusion of an entangled polymer is much slower than that of the free Rouse chain due to the topological interactions with surrounding chains which prevent them from crossing each other. Consider a chain confined in a polymer network, the topological constraints imposed on the probe chain could be described by a set of obstacles scattered around the chain, as shown in Fig. 1.5. These obstacles do not affect the static properties of the probe chain, but significantly change dynamics. Since the transverse fluctuation of the chain is restricted to a "tube-like" region (dashed curves in Fig. 1.5), the chain can be assumed as confined in an effective tube with a constant diameter. Such mean-field assumption captures the essence of
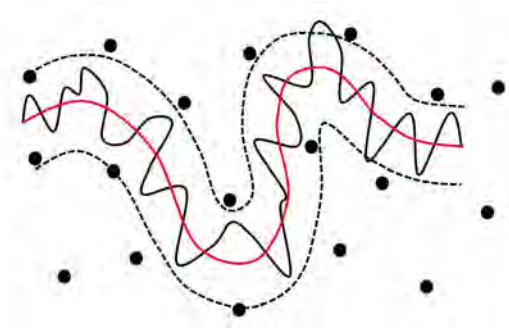
Figure 1.5: A schematic plot of the tube model.

entanglement and allows relatively simple mathematical treatment. Along the tube contour, the shortest path between the two chain ends is called the "primitive path", as shown by the red curve in Fig. 1.5. On the primitive path, the projected chain is called the "primitive chain", which has a contour length L.

Defining the primitive chain in a continuous manner, say $\mathbf{R}(s,t)$ is the position of the chain segment s at time t, $s \in [0, \dots, L]$. The tangent vector on s is given by

$$\mathbf{u}(s,t) = \frac{\partial \mathbf{R}(s,t)}{\partial s}.$$

The original tube mode has two assumptions about the primitive chain. The first one is that the contour length of the primitive chain does not fluctuate. This assumption significantly simplifies the theoretical treatment, but introduces a non-trivial error (see Sec. 1.5.5). The second assumption is that the correlation of the tangent vectors $\mathbf{u}(s,t)$ and $\mathbf{u}(s',t)$ decays quickly with $|s - s'|$, such that the primitive chain is Gaussian. With these two assumptions, the primitive path could be visualized as a random walk with a step length a, which is the length of the **tube statistical segments** (or "tube segments"). Since the mean-square end-to-end vector of the primitive chain is equal to that of the 3D chain, we have

$$\left\langle \mathbf{R}_{\mathrm{e}}^2 \right\rangle = Za^2 = Nb^2,$$

where Z is the number of tube segments or entanglements per chain. The contour

length L of the primitive chain is then given by

$$L = Za = \frac{Nb^2}{a}.$$

According to Eq. 1.3, the free energy of a chain reaches its minimum when the end-to-end distance is zero, which seems to imply a chain confined in a tube should collapse into a coil. To understand the paradoxical result, one must distinguish the effective tube from the infinite long tube. In the tube model, the chain ends are not confined in the tube, but can freely explore the polymer network. Therefore, the chain ends have higher degree of freedom than middle monomers, acting as a hypothetical tensile force applied at the chain ends to keep a contour length L:

$$f_{\mathrm{eq}} = \frac{3k_{\mathrm{B}}T}{Nb^2}L = \frac{3k_{\mathrm{B}}T}{a}.$$

According to this equation, the virtual force only depends on the tube segment length a.

In a tube segment, the average number of monomers is $N_{\mathrm{e}} = N/Z$, thus a is given by

$$a = \sqrt{N_{\mathrm{e}}}b$$

In the discussion of scaling behaviours, a is also regarded as the **tube diameter**. At the length scales smaller than a, the monomers are not aware of the tube confinement, and thus follow Rouse motion. Therefore, the entanglement strand with N_{e} monomers relaxes with a characteristic time τ_{e}:

$$\tau_{\mathrm{e}} = N_{\mathrm{e}}^2 \tau_0,$$

which is the Rouse time of a tube segment.

1.5.2   Reptation

The breakthrough that makes the tube model applicable to describe polymer dynamics was brought by de Gennes [16], who proposed a **"reptation"** model to depict
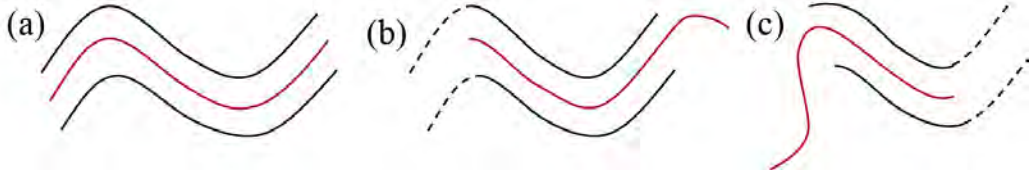
Figure 1.6: Reptation of the primitive chain.

the "snake-like" motion of the chain in a fixed network. In the "reptation" picture (see Fig. 1.6), the primitive chain moves forward and backward along the tube contour with a friction proportional to the number of monomers, $N\xi$, such that the diffusion coefficient of the primitive chain is

$$D_{\mathrm{c}} = \frac{k_{\mathrm{B}}T}{N\xi}.$$

During reptation, the chain ends will extend out of the original tube and create new tube segments with random orientations. In this way, the original tube will be forgotten gradually. The time for the chain to completely diffuse out of the original tube is the "reptation time", which could be estimated by

$$\tau_{\mathrm{rep}} \approx \frac{\langle L^2 \rangle}{D_c} \approx \frac{\xi N_{\mathrm{e}}^2 b^2}{k_{\mathrm{B}}T} \left(\frac{N}{N_{\mathrm{e}}} \right)^3 = \frac{\xi N_{\mathrm{e}}^2 b^2}{k_{\mathrm{B}}T} Z^3. \tag{1.30}$$

As shown in Fig. 1.6(b) and (c), a tube segment is released when either chain ends passes through it. The survival probability of the segment s after time t, $\psi(s,t)$, can be obtained by solving the diffusion equation:

$$\frac{\partial \psi(s,t)}{\partial t} = D_c \frac{\partial^2 \psi(s,t)}{\partial s^2},$$

with the boundary conditions:

$$\psi(s,0) = 1; \quad \psi(0,t) = 0; \quad \psi(L,t) = 0.$$

The solution of the equation is

$$\psi(s,t) = \sum_{p=1,odd}^{\infty} \frac{4}{\pi p} \sin\left(\frac{\pi p s}{L} \right) \exp\left(-\frac{p^2 t}{\tau_{\mathrm{rep}}} \right), \quad \tau_{\mathrm{rep}} = \frac{L^2}{\pi^2 D_c}. \tag{1.31}$$

The analytical solution of τ_{rep} is smaller than the scaling approximation (Eq. 1.30) by a factor of $1/\pi^2$. The fraction of the tube segments that live longer than t is an integral of $\psi(s,t)$ over the contour length:

$$\mu(t) = \frac{1}{L} \int_0^L \psi(s,t)\mathrm{d}s = \frac{8}{\pi^2} \sum_{p=1,odd}^{\infty} \frac{1}{p^2} \exp\left(-\frac{p^2 t}{\tau_{\text{rep}}}\right) \qquad (1.32)$$

The tube model assumes that once a tube segment is deleted, any deformation associated to it is forgotten, therefore $\mu(t)$ is proportional to the end-to-end vector relaxation function $\Phi(t)$:

$$\Phi(t) = \frac{\langle \mathbf{R}_{\text{e}}(t) \cdot \mathbf{R}_{\text{e}}(0) \rangle}{\mathbf{R}_{\text{e}}^2} = \mu(t).$$

1.5.3   Stress Relaxation and Viscosity

At the time scales $\tau_0 < t < \tau_{\text{e}}$, the monomers follows Rouse motion, such that the stress relaxation modulus $G(t)$ is the same as Eq. 1.27:

$$G(t) = G_0 \left(\frac{t}{\tau_0}\right)^{-1/2} = \frac{\phi k_{\text{B}} T}{b^3} \left(\frac{t}{\tau_0}\right)^{-1/2} \qquad (\tau_0 < t < \tau_{\text{e}})$$

On the time scale $t = \tau_{\text{e}}$, each entanglement strand contributes order of $k_{\text{B}} T$ to the stress relaxation modulus G_{e}:

$$G_{\text{e}} = G(\tau_{\text{e}}) = \frac{G_0}{N_{\text{e}}} = \frac{\phi k_{\text{B}} T}{N_{\text{e}} b^3} = \frac{\rho R T}{M_{\text{e}}},$$

where ρ is the density of the melt, R is the idea gas constant. At time scales $t > \tau_{\text{e}}$, the chains are relaxed by reptation. Thus the stress relaxation modulus $G(t)$ is proportional to the survival fraction of the tube segments (Eq. 1.32):

$$G(t) = G_{\text{e}}\mu(t) = \frac{8}{\pi^2}G_{\text{e}} \sum_{p=1,\text{odd}}^{\infty} \frac{1}{p^2} \exp\left(-\frac{p^2 t}{\tau_{\text{rep}}}\right), \qquad (1.33)$$

Due to the factor $1/p^2$ in Eq. 1.33, the longest relaxation time τ_{rep} dominates $G(t)$. At the timescales $\tau_{\text{e}} < t < \tau_{\text{rep}}$, $G(t)$ shows a plateau regime. Thus, G_{e} is also termed as the "plateau modulus", analogous to a permanent polymer network.

The viscosity predicted by the reptation model is given by the time integral of $G(t)$:

$$\eta_0 = \int_0^\infty G(t)dt = \frac{\pi^2}{12}G_e\tau_{\text{rep}}.$$

Since G_e is independent of the molecular weight M and τ_{rep} is proportional to M^3, the viscosity η_0 is proportional to M^3. However, experimental results indicate a power law $\eta_0 \sim M^{3.4}$ [4–7], whose exponent 3.4 is significantly larger than the prediction of reptation picture.

1.5.4 Monomer Mean-Square Displacement

At time scales smaller than τ_e, the monomers are not aware of the tube confinement, thus the monomer mean-square displacement follows the Rouse behaviour same as Eq. 1.25:

$$g_1(t) \approx b^2 \left(\frac{t}{\tau_0}\right)^{1/2} \quad (\tau_0 < t < \tau_e).$$

After τ_e, the monomer displacement perpendicular to the primitive path on the length scales larger than a is prohibited by the effective tube confinement, while the diffusion along the tube contour is free. At the time scales $\tau_e < t < \tau_R$, the monomers are involved in the coherent Rouse motion of the chain sections containing $(t/\tau_0)^{1/2}$ monomers, thus the 1D curvilinear mean-square displacement of the monomers is of the order of the mean-square size of the chain sections:

$$\langle(\Delta s\,(t))^2\rangle \approx b^2 \left(\frac{t}{\tau_0}\right)^{1/2} = a^2 \left(\frac{t}{\tau_e}\right)^{1/2} \qquad \tau_e < t < \tau_R. \tag{1.34}$$

However, the displacement of such subdiffusive motion is much shorter in 3D space, because the primitive path is effectively a random walk in 3D space with a step length equal to the tube segment length a. Since the primitive length of the random walk along the tube is $\sqrt{\langle(\Delta s\,(t))^2\rangle}$, the monomer mean-square displacement in 3D is the product of the step length and the primitive length:

$$g_1(t) \approx a\sqrt{\langle(\Delta s\,(t))^2\rangle} \approx a^2 \left(\frac{t}{\tau_e}\right)^{1/4} \qquad \tau_e < t < \tau_R.$$

At $t = \tau_R$, $g_1(t) \approx Nb^2$ indicates the monomer mean-square displacement is of the order of the mean-square end-to-end distance $\mathbf{R}_e^2$. At the time scales larger than τ_R, the monomers are involved in the reptation of the primitive chain, thus the 1D mean-square displacement is

$$\langle (\Delta s(t))^2 \rangle \approx D_c t = \frac{k_B T}{N\xi} t \qquad \tau_R < t < \tau_{\text{rep}}.$$

The corresponding mean-square displacement in 3D space is

$$g_1(t) \approx a\sqrt{\langle (\Delta s(t))^2 \rangle} = a\sqrt{\frac{k_B T}{N\xi} t} \qquad \tau_R < t < \tau_{\text{rep}}.$$

At the time scales $t > \tau_{\text{rep}}$, the whole chain follows free diffusion, $g_1(t) \sim t$.

In summary, the mean-square displacement of the monomers $g_1(t)$ have 4 regimes in reptation model:

$$g_1(t) \sim \begin{cases} t^{1/2}, & \tau_0 < t < \tau_e \\ t^{1/4}, & \tau_e < t < \tau_R \\ t^{1/2}, & \tau_R < t < \tau_{\text{rep}} \\ t, & t > \tau_{\text{rep}} \end{cases} \tag{1.35}$$

1.5.5 Contour Length Fluctuation

In the reptation model, the primitive chain or primitive path is assumed to have a constant length L. Doi [18] suggested that the contour length can fluctuate due to the Rouse motion of the chain. Thus, one can expect that the characteristic time of the contour length fluctuation (CLF) is the Rouse time τ_R. According to Eq. 1.34, the inherent curvilinear leads to contour length fluctuation:

$$\langle [L(t) - L(0)]^2 \rangle^{1/2} \approx b \left(\frac{t}{\tau_0} \right)^{1/4} \qquad (\tau_0 < t < \tau_R).$$

The contour length fluctuations at the early times slightly reduce the stress relaxation modulus $G(t)$, because a fraction of tube is released:

$$G(t) \approx G_e \frac{\langle L \rangle - \langle [L(t) - L(0)]^2 \rangle^{1/2}}{\langle L \rangle} \approx G_e \left[1 - \frac{N_e}{N} \left(\frac{t}{\tau_e} \right)^{1/4} \right] \qquad (\tau_e < t < \tau_R).$$

$$\tag{1.36}$$

Since $(\tau_\mathrm{R}/\tau_\mathrm{e})^{1/4}$ is proportional to $N^{1/2}$, the difference between G_e and $G(\tau_\mathrm{R})$ decreases as the chain length N increases. Therefore, the contour length fluctuation is more important on relatively short chains.

According to Eq. 1.36, the stress relaxation modulus at the Rouse time of the chain is lower than G_e:

$$G(\tau_\mathrm{R}) \approx G_\mathrm{e} \left[1 - \frac{N_\mathrm{e}}{N} \left(\frac{\tau_\mathrm{R}}{\tau_\mathrm{e}} \right)^{1/4} \right] \approx G_\mathrm{e} \left(1 - \mu \sqrt{\frac{N_\mathrm{e}}{N}} \right),$$

where μ is a coefficient of order unity [75]. The reptation time is also reduced by a factor of $\left(1 - \mu \sqrt{N_\mathrm{e}/N} \right)^2$:

$$\tau_\mathrm{rep} \approx \frac{\langle L^2 \rangle}{D_\mathrm{c}} \left(1 - \mu \sqrt{\frac{N_\mathrm{e}}{N}} \right)^2 \approx \tau_0 \frac{N^3}{N_\mathrm{e}} \left(1 - \mu \sqrt{\frac{N_\mathrm{e}}{N}} \right)^2.$$

The viscosity can be estimated by the product of the dominate reptation time and the stress relaxation modulus at τ_rep:

$$\eta_0 \approx G(\tau_\mathrm{rep}) \tau_\mathrm{rep} \approx \frac{\tau_0 k_\mathrm{B} T}{b^3} \frac{N^3}{N_\mathrm{e}^2} \left(1 - \mu \sqrt{\frac{N_\mathrm{e}}{N}} \right)^3$$

Over a reasonable range of molecular weight, this equation predicts that the molar mass dependence of viscosity, $\eta_0 \sim M^{3.4}$ [18], which explains the difference between the predictions of reptation model and the experimental results. For very long chains, the contribution of the contour length fluctuations become less important, thus the exponent will slowly fall back to 3.0 with increasing chain length.

1.5.6 Constraint Release

The model combining reptation and contour length fluctuation can describe the dynamics of polymer chains in a matrix of much longer chains or in a fixed network. In a monodisperse system, the chains imposing topological constraints to a probe chain also experience reptation and contour length fluctuations in their own tubes. Therefore, the tube segments of the probe chain can fluctuate when some of these
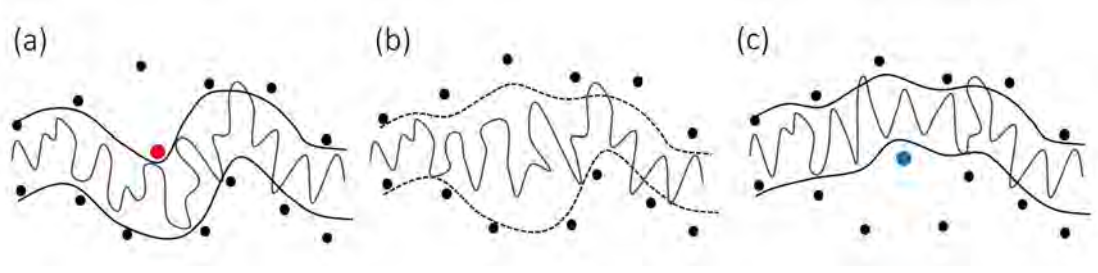
Figure 1.7: The schematic plot of constraint release.

chains move away by CLF or reptation. As shown in Fig. 1.7(a), the departure of a neighboring chain is represented by the disappearing of one obstacle (red), which leaves a vacant volume of dimension of a^3. The probe chain can explore this volume as shown in Fig. 1.7(b). If a new chain moves in, as shown by the inserted obstacle (blue) in Fig. 1.7(c), the probe chain effectively hop a distance of a. The local rearrangement of the tube segments due to the exchange of the surrounding chains is called constraint release.

The constraint release process could be modelled by the Rouse motion of the tube consisting of N/N_e segments, called constraint release Rouse (CR Rouse) motion [25]. The hopping frequency of tube segments is inversely proportional to the reptation time τ_{rep}^s of the surrounding chains that impose constraints [76, 77]. Therefore, the relaxation time of CR Rouse motion of the tube is

$$\tau_{CR} \approx \tau_{rep}^s \left(\frac{N}{N_e} \right)^2.$$

For monodisperse systems, τ_{CR} is proportional to N^5, which is much longer than the reptation time, $\tau_{rep} \sim N^3$. Therefore, one should not expect the constraint release to affect the terminal relaxation time τ_{rep} or the end-to-end relaxation $\Phi(t)$ strongly, because they are dominated by reptation of the chain itself.

Combining both reptation and constraint release, the diffusion coefficient of a probe chain could be approximated as

$$D \approx \frac{\langle \mathbf{R}_e^2 \rangle}{\tau_{rep}} + \frac{\langle \mathbf{R}_e^2 \rangle}{\tau_{CR}}. \tag{1.37}$$

In monodisperse systems, τ_{rep} is much shorter than τ_{CR}, and thus the second term on the right-hand side of Eq. 1.37 is negligible. In polydisperse systems, the contribution of constraint release on chain diffusion can be non-trivial. Consider the binary blend of polymers with drastically different molecular weights, where the long chains are confined in the matrix of the short chains. When the reptation time of the surrounding chains is much shorter than the reptation time of the long chain, the diffusion coefficient is dominated by constraint release effect.

Due to the broad distribution of the hopping rates of the tube segments, significant amount of constraint release events happen much earlier than the reptation time of the probe chain, whose effect needs to be taken into account for predicting stress relaxation, even for monodisperse systems [78, 79]. The stress relaxation caused by the CR Rouse motion of the tube is proportional to $t^{-1/2}$ (see Eq. 1.27):

$$G_{\mathrm{CR}}(t) \sim \left(\frac{t}{\tau_{\mathrm{rep}}^{\mathrm{s}}}\right)^{-1/2}.$$

Accordingly, certain fraction of the stress would be released at $\tau_{\mathrm{rep}}^{\mathrm{s}}$. The CR contribution to the stress relaxation modulus of monodisperse systems was first deduced by Graessley [80]:

$$G(t) = G_{\mathrm{e}}\mu(t)R(t),$$

where $G(t)$ is proportional to the product of the fraction of the surviving tube at t, $\mu(t)$, and contribution due to CR Rouse motion of the tube, $R(t)$. In the "double reptation" model, $R(t) \sim \mu(t)$, we have $G(t) \sim \mu(t)^2$ [20]. Rubinstein and Colby [21] presented a self-consistent model to describe the stress relaxation of the binary blends, in which the stress modulus is calculated using a linear mixing rule of the stress relaxation moduli of the two components:

$$G(t) = G_{\mathrm{e}}\left(\phi_{\mathrm{L}}\mu_{\mathrm{L}}(t)R_{\mathrm{L}}(t) + \phi_{\mathrm{S}}\mu_{\mathrm{S}}(t)R_{\mathrm{S}}(t)\right),$$

where "L" and "S" represent the long and short chains, and $\phi_{\mathrm{L,S}}$ refer to their volume fractions.

1.6 Multiscale Computer Simulations

1.6.1 Molecular Dynamics Simulation

Due to the rapid advances of the computer technology, molecular dynamics (MD) simulation is widely used in the study of polymer dynamics. With well-defined potential field, the motion of the molecules can be obtained by integrating the equations of motion, e.g., the Newton's equation. Comparing to coarse-grained models, MD simulations based on bead-spring models carry much more fine details and can provide microscopic understanding that are generally not accessible by experiments. However, MD simulation requires much longer simulation time than the coarse-grained models. A typical MD simulation system for polymer dynamics usually has to simulate more than $10^4 \sim 10^5$ particles, with a simulation time span over nine decades. Such computational cost strongly limits their applications to the entanglement dynamics at large time scales.

For studying dynamics in polymer melts, a well-developed generic bead spring model is the **Kremer-Grest (KG) model** [49, 50]. In this model, the non-bonded interactions are given by the truncated-shifted **Lennard-Jones (LJ) potential**,

$$U_{\mathrm{LJ}}(r) = \begin{cases} 4\epsilon \left[\left(\dfrac{\sigma}{r}\right)^{12} - \left(\dfrac{\sigma}{r}\right)^{6} + \dfrac{1}{4} \right] & r < r_c \\ 0 & r > r_{\mathrm{c}} \end{cases} \tag{1.38}$$

where r is the distance between two beads, ϵ is the depth of the potential well, σ is the diameter of the beads, $r_{\mathrm{c}} = 2^{1/6}\sigma$ is a typical cutoff-distance beyond which the potential is zero. ϵ and σ are used as the units for potential and distance. The corresponding LJ time unit is $\tau_{\mathrm{LJ}} = \sigma(m/\epsilon)^{1/2}$, where m is the mass of the beads. In the KG model, the bonding potential between two adjacent particles in a chain is given by the **finitely extensible nonlinear elastic (FENE) potential**,

$$U_{\mathrm{FENE}}(r) = \begin{cases} -\dfrac{1}{2}kR_0^2 \ln\left(1 - \left(\dfrac{r}{R_0}\right)^{1/2}\right) & r \leq R_0 \\ \infty & r > R_0 \end{cases} \tag{1.39}$$
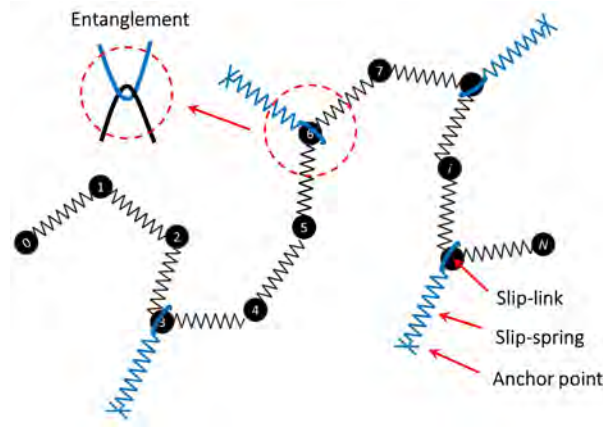
Figure 1.8: The schematic plot of the slip-spring model.

where $k = 30\epsilon/\sigma^2$ is the spring constant, $R_0 = 1.5\sigma$ is the maximum bond length. FENE potential can effectively prevent chain crossing, thus the KG model is applicable to entangled polymers. In the KG model, the particle density is $\rho = 0.85\sigma^{-3}$, and the average bond length is $\langle l^2 \rangle^{1/2} = 0.97\sigma$.

In addition, using harmonic bending potential is considered as an effective way to introduce chain stiffness and consequently more entanglements to the chain. A typical bending potential is given by

$$U_{\mathrm{bend}}(\theta) = k_\theta \left(1 - \cos\theta\right),$$

where the coefficient k_θ is usually set to be 2ϵ or 3ϵ. θ is the angle of the neighboring bond vectors.

1.6.2 Slip-Spring Model

Model Construction

The basic building block of the slip-spring model is the Rouse chain. Consider a Rouse chain constituted by $N + 1$ monomers. The bonding potential between the

neighbouring monomers i and $i + 1$ is harmonic:

$$U_{\text{bond}}(i, i + 1) = \frac{3k_{\text{B}}T}{b^2} \left(\mathbf{R}_i - \mathbf{R}_{i+1} \right)^2 .$$

The topological constraints imposed by the surrounding chains are represented by a set of virtual springs, as shown in Fig. 1.8. Each virtual spring has one end ("anchor point") anchored in space, and the other end connected to the chain via the slip-link. The slip-links are the small rings that the chain can pass though, due to reptation or CLF. The potential of virtual springs is harmonic,

$$U_{\text{ss}}(j) = \frac{3k_{\text{B}}T}{N_s b^2} \left(\mathbf{a}_j - \mathbf{R}_{x_j} \right)^2 ,$$

where $\mathbf{a}_j$ is the coordinate of the anchor point of the j-th virtual spring, x_j is the index of the bead that the slip-link sits on, N_{s} is the number of monomers in the virtual spring. The average number of slip-springs on each chain is equal to $Z^{\text{SS}} = N/N_{\text{e}}^{\text{SS}}$. There are thus on average one slip-link per chain segment of N_{e}^{SS} monomers. N_{e}^{SS} and N_{s} are a pair of adjustable parameters in the slip-spring model, their combination determines the plateau modulus G_{e}^{SS} and terminal properties [66]. The total energy of a chain is a sum of the potential of the bonds and the virtual springs:

$$U_{\text{chain}} = \sum_{i=0}^{N-1} U_{\text{bond}}(i, i + 1) + \sum_{j=1}^{Z^{\text{SS}}} U_{\text{ss}}(j).$$

The equation of motion of the Rouse beads in the slip-spring model is similar to Eq. 1.10:

$$\xi \frac{\text{d}\mathbf{R}_i}{\text{d}t} = -\frac{\partial U_{\text{chain}}}{\partial \mathbf{R}_i} + \mathbf{f}_i(t). \tag{1.40}$$

Algorithms for Slip-Link Motion

In the slip-spring model, an algorithm is required to govern the diffusion of the slip-links along the chain. There are two versions of slip-spring models with different slip-link motion algorithms. The original version uses Brownian dynamics that allows the slip-links to slide along the chain continuously [66, 81, 82]. The friction of slip-links

ξ_{sl} is artificially defined, but must be much smaller than the frictions of the Rouse beads ξ, i.e., $\xi_{\mathrm{sl}} = 0.1\xi$ in Ref. [66]. A small friction ξ_{sl} ensures that the slip-links does not affect the chain diffusion. But in accompany with it, a small time-step Δt must be employed, e.g., the standard time-step is $0.01\tau_0$ for integrating the equation of motion of the Rouse beads and slip-links, where τ_0 is the slip-spring unit time.

In order to increase Δt, an updated slip-spring model employs Monte-Carlo method to govern the motion of the slip-links [83]. Specifically, at each time-step, a slip-link hops between the nearest neighbouring monomers with a frequency of f^{SS}. The hopping is governed by the Metropolis-Hasting algorithm: the hopping from monomer i to j ($j = i \pm 1$) is accepted with a probability of $\exp(-\Delta E/k_{\mathrm{B}}T)$. ΔE is the change of the potential energy due to the hopping:

$$\Delta E = \frac{3k_{\mathrm{B}}T}{N_{\mathrm{s}}b^2} \left(\mathbf{R}_j^2 - \mathbf{R}_i^2 + 2\mathbf{a} \cdot (\mathbf{R}_i - \mathbf{R}_j) \right),$$

where $\mathbf{a}$ is the position of the anchor point. When $\Delta E < 0$, the hopping will always be accepted because $\exp(-\Delta E/k_{\mathrm{B}}T) > 1$.

Constraint Release

With the assumption that the entanglements are binary events, the slip-spring model can easily incorporate constraint release effect by simulating an ensemble of chains. The algorithm is based on the "duality" of the constraint release: disentanglement between a pair of chains takes place when either chain moves away by reptation or contour length fluctuation. Particularly, each slip-link is paired with another slip-link sitting on another chain in the ensemble. When one slip-link is deleted from the end of one chain, the paired slip-link will also be released instantaneously, leading to a CR event. To ensure a constant number of the slip-springs in the ensemble, a new pair of slip-springs would be added back immediately after the removal of the old pair: one slip-spring is attached to the end of a randomly selected chain, while the paired one would be added on a random bead of another chain. Because the slip-links cannot sit on the same bead, the newly added slip-slinks must be added

on the beads without slip-links. It should be noted that the slip-links on the same chain are not coupled, because the fraction of the self-entanglement in this model is not fully consistent with the real system.

Chapter 2

The First-Passage Time Problem of One-Dimensional Rouse Chain

2.1 Overview

The simplest branched polymer is 3-arm symmetric stars. In the description of the tube model, star arms are confined in their own tubes. Reptation is highly suppressed because one arm has to simultaneously drag all other arms into the same tube to reptate. In order to relax, arms must retract some distance towards the branch point along the primitive path, and poke out to create new tube segments. By repeating this process, the old tube segments that have been visited by the arm free end will be forgotten, whereby the stress associated with them would be relaxed. An arm is fully relaxed when its free end retracts all the way back to the branch point. Due to the steeply growing quadratic potential field, the arm retraction process, essentially analogous to contour length fluctuation, is a thermally activated process, whose relaxation time can be obtained from the solution of the first-passage problem (or Kramers problem [31]) for a diffusing chain [27].

Consider the primitive chain as a 1D Rouse chain along the tube contour with one end fixed to the branch point and the other end stretched by a virtual tensile force

[17]. The arm retraction problem is a multi-dimensional first-passage problem, whose dimensionality is equal to the number of Rouse modes. Milner and McLeish [30] solved this problem by treating the whole chain as one bead attached to the branch point via a harmonic spring, which essentially reduces the multi-dimensional problem into a 1D case by only considering the slowest mode, which might overestimate the relaxation time.

As the simplest stochastic model of polymer dynamics, the 1D Rouse model almost has everything solved analytically, such as the stress and end-to-end relaxation functions. A notable exception is the first-passage problem, which in fact is a general challenge for the study of rare events [84]. To cope with such problems, many advanced numerical methods have been developed to accelerate computer simulations in order to provide reliable numerical solutions [68–70, 85–87]. These numerical methods, which have been shown to be remarkably successful in other scientific areas, should also be applicable to the first-passage problem of the 1D Rouse chain model.

At the beginning of this chapter, we introduce the solution of the Milner-McLeish theory without constraint release and an asymptotic solution for multi-dimensional first-passage problems. In order to examine these two theoretical predictions, we employ advanced numerical methods, including the forward flux sampling (FFS) and weighted ensemble (WE) method, which have been reported with excellent performance for solving other first-passage problems. Before being applied to the arm-retraction problem, both methods are tested on a simple 2D case, which is the simplest multi-dimensional first-passage problem. Then we choose the FFS method to investigate the extension problem of 1D Rouse chain, which is analogous to the arm-retraction problem. The mean first-passage time $\tau(z)$ is measured when the free end of the chain extends over a certain distance z away from the origin (fixed end). The results show that the mean first-passage time is getting shorter if the Rouse chain is represented by more beads, which validates the prediction of the

asymptotic solution.

2.2 Theoretical Solutions of Arm Retraction

2.2.1 From Retraction to Extension

Consider an arm confined in an effective tube as shown in Fig. 2.1(a). At length scales shorter than the tube diameter a, the monomers are not aware of the confining tube, and thus the dynamics follows Rouse motion. Above the length scale of a, one can use the primitive chain to describe the dynamics. Consider the primitive chain as a 1D Rouse chain along the tube contour, whose one end is fixed to the branch point and the other end is free to move, leading to creation or deletion of tube segments (see Fig. 2.1(b)). Because the arm free end is able to explore more directions in the polymer melt than the middle monomers, the primitive chain has a non-zero average length due to the entropy gain at the end:

$$\bar{L} = (N/N_e)a$$

where N is the number of monomers, a is the tube diameter, and N_e is the entanglement segment length. The entropic tensile force acting on the chain end is given as (Fig. 2.1(c)):

$$f_{eq} = \frac{3k_BT}{Nb^2}\bar{L} = \frac{3k_BT}{a},$$

where k_B is the Boltzmann constant, T is the temperature, and b is the Kuhn length. Define z as the length of the tube sections that have been visited by the free end during arm retraction, as shown in the Fig. 2.1(b) and (c). The energy barrier for the arm end required to retract a distance z is given by [27]:

$$U(z) = \frac{3k_BT}{2Nb^2}z^2. \tag{2.1}$$

This potential function takes the same form as for a 1D Rouse chain with one end fixed to extend over a distance z, as shown in Fig. 2.1(d). Therefore the Rouse
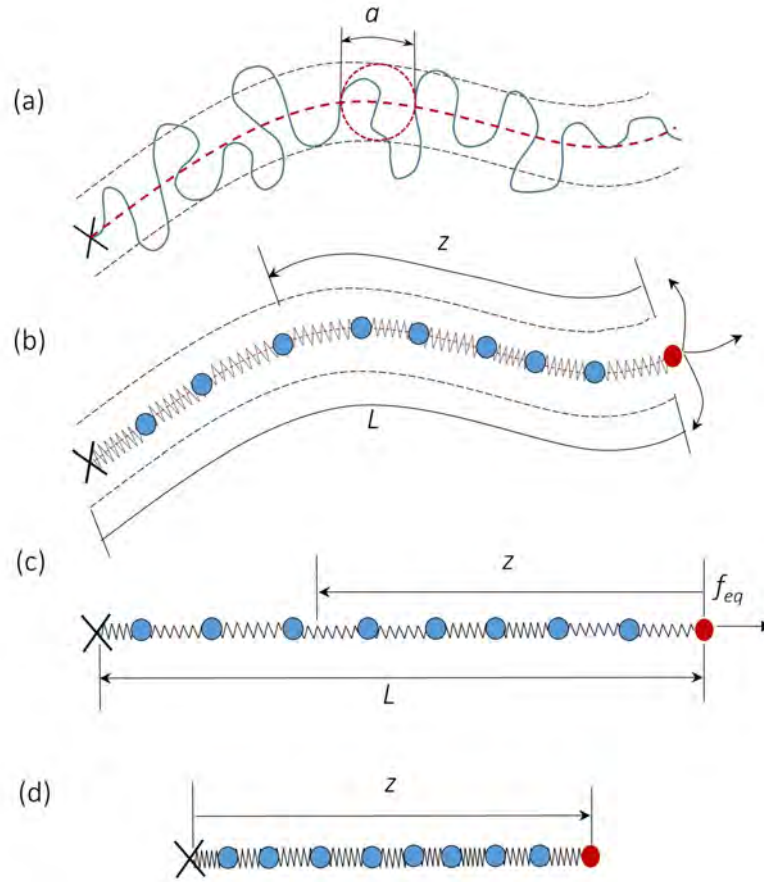
Figure 2.1: A schematic plot of the transformation from the arm-retraction problem to an extension problem of a 1D Rouse chain.

chain extension is a reverse process of arm retraction, and so can be mathematically treated in the same way. Due the steeply growing energy barrier, the first-passage time to retract a distance z can be approximated by

$$\tau(z) = \tau_0 \exp\left(\frac{U(z)}{k_{\mathrm{B}}T}\right),$$

where τ_0 was intuitively considered as the Rouse time τ_{R} of the 1D Rouse chain with one end fixed [26].

Figure 2.2: Rouse chain with one end fixed.

2.2.2 Rouse Chain with One End Fixed

Consider a Rouse chain with one end fixed, whose N beads are connected by $N-1$ harmonic springs with an elastic constant $k = 3k_{\mathrm{B}}T/b^2$. The first bead $i = 1$ is connected to the origin by another harmonic spring, as shown in Fig. 2.2. Using a N-order connectivity matrix, the equations of motion of beads can be written as:

$$\xi_0 \mathrm{d}\mathbf{R}_i = -kA_{ij}\mathbf{R}_j \mathrm{d}t + \sqrt{2k_{\mathrm{B}}T\xi_0}\mathrm{d}\mathbf{W}_i, \qquad i = 1, ..., N \tag{2.2}$$

where ξ_0 is the friction coefficient of beads, $\mathbf{W}$ is a Wiener process, A_{ij} is the element of the connectivity matrix:

$$\mathbf{A} = \begin{pmatrix} 2 & -1 & . & . & & & & \\ -1 & 2 & -1 & . & & & & \\ . & . & . & . & . & . & . & . \\ & & & . & 2 & -1 & . \\ & & & . & -1 & 2 & -1 \\ & & & . & . & -1 & 1 \end{pmatrix}$$

Multiplying $\mathbf{R}_i$ by matrix Φ which consists of the eigenvectors of $\mathbf{A}$, the equations of motion are transformed into normal modes:

$$\xi_p \mathrm{d}\mathbf{X}_p = -k_p\mathbf{X}_p\mathrm{d}t + \sqrt{2k_{\mathrm{B}}T\xi_p}\mathrm{d}\mathbf{W}_p, \tag{2.3}$$

where the Rouse mode $\mathbf{X}_p$ is given by

$$\mathbf{X}_p = \frac{1}{N+1/2} \sum_{i=1}^{N} \mathbf{R}_i \sin\left(\frac{\pi p\,(i+1/2)}{N+1/2}\right), \qquad p = 1, 2, ..., N, \qquad (2.4)$$

and the friction coefficient ξ_p and the elastic constant k_p are given by

$$\xi_p = 2(N+1/2)\xi_0, \quad k_p = \frac{24 k_\mathrm{B} T (N+1/2)}{b^2} \sin^2\left(\frac{\pi(p-1/2)}{2(N+1/2)}\right). \qquad (2.5)$$

The inverse transform from $\mathbf{X}_p$ to monomer coordinate is given by

$$\mathbf{R}_i = 2\sum_{p=1}^{N} \mathbf{X}_p \sin\left(\frac{\pi i\,(p-1/2)}{N+1/2}\right). \qquad (2.6)$$

For each mode, the relaxation time τ_p is given by

$$\tau_p = \frac{\xi_p}{k_p} = \frac{\xi_0 b^2}{12 k_\mathrm{B} T} \sin^{-2}\left(\frac{\pi\,(p-1/2)}{2\,(N+1/2)}\right), \qquad p = 1, \ldots, N,$$

Thus, the relaxation time of the fastest mode is $\tau_N \approx \xi_0 b^2 / 12 k_\mathrm{B} T$, and the Rouse time τ_R is given by,

$$\tau_\mathrm{R} = \tau_1 \approx \frac{4\xi_0 b^2 N^2}{3\pi^2 k_\mathrm{B} T}, \qquad (2.7)$$

which is 4 times larger than τ_R of the chain with both ends free.

2.2.3   The Kramers Problem in Arm Retraction

According to Eq. 2.3, the extension of 1D Rouse chain can be decomposed into independent Rouse modes, whereby the bead coordinates R_i are converted into X_p via Eq. 2.4 (italic rather than bold font is for 1D case). Since each mode corresponds to one degree of freedom, this extension problem can be treated as a particle diffusing in an N-dimensional space. Therefore, the arm retraction problem is equivalent to the following first-passage problem: a particle is injected at the origin and deleted when it reaches the absorbing boundary satisfying

$$z = 2\sum_{p=1}^{N} X_p \sin\left(\frac{\pi N\,(p-1/2)}{N+1/2}\right), \qquad z \gg a, \qquad (2.8)$$

while the potential in each dimension is given by

$$U(X_p) = \frac{1}{2}k_p X_p^2. \tag{2.9}$$

In the Milner-McLeish theory [30, 37], this multi-dimensional problem is simplified into a 1D case by coarse-graining the whole chain into a single bead connected to the origin via a harmonic spring, whose elastic constant is $3k_{\mathrm{B}}T/Nb^2$. The equation of motion of the bead is

$$\xi_{\mathrm{eff}}\frac{dx}{dt} = -\frac{3k_{\mathrm{B}}T}{Nb^2}x + f(t), \tag{2.10}$$

where x is the coordinate of the particle, $f(t)$ is the random force satisfying $\langle f(t)f(t')\rangle = 2\xi_{\mathrm{eff}}k_{\mathrm{B}}T\delta(t-t')$, $\xi_{\mathrm{eff}} = N\xi_0/2$ is the effective friction coefficient. ξ_{eff} is half of the chain friction because the center of mass travels half the distance of the free end. The relaxation time $\tau_{\mathrm{MM}}(z)$ is the first-passage time that the bead extends over a distance of z.

2.2.4   Exact Solution of 1D Kramers Problem

In this subsection, we start from a general solution of the Kramers problem without specifying the dimensionality. Then we will introduce the exact solution of 1D Kramers problem and use it to calculate $\tau_{\mathrm{MM}}(z)$.

Consider a Brownian particle in a deep potential well, $U(\mathbf{R})$. To escape from the potential well, the particle has to overcome an extremely high energy barrier at the boundary $\mathbf{R}_s$, $U(\mathbf{R}_s) \gg k_{\mathrm{B}}T$. Define $\psi(\mathbf{R}, t)$ as the probability density to find the particle at coordinate $\mathbf{R}$ and time t. $\psi(\mathbf{R}, t)$ can be obtained by solving the Smoluchowski equation:

$$\xi\frac{\partial\psi}{\partial t} = \nabla\left(\nabla U(\mathbf{R}) + k_{\mathrm{B}}T\nabla\right)\psi.$$

If there is no absorbing boundary, ψ is independent of t and follows Boltzmann distribution:

$$\psi(\mathbf{R}) = \frac{1}{\mathcal{N}}\exp\left(-\frac{U(\mathbf{R})}{k_{\mathrm{B}}T}\right), \quad \mathcal{N} = \int\exp\left(-\frac{U(\mathbf{R})}{k_{\mathrm{B}}T}\right)d\mathbf{R}. \tag{2.11}$$

With an absorbing boundary, one can find a **steady state** solution for ψ. In steady state, ψ is time-independent. The current $\mathbf{J}(\mathbf{R})$ is given by **Fick's law**,

$$\mathbf{J}(\mathbf{R}) = -\frac{1}{\xi}\psi(\mathbf{R})\nabla U(\mathbf{R}) - \frac{k_{\mathrm{B}}T}{\xi}\nabla\psi(\mathbf{R}). \tag{2.12}$$

Assuming that ψ follows Boltzmann distribution in most places apart from the small region close to the absorbing boundary, it is convenient to change the unknown $\psi(\mathbf{R})$ in this case to

$$\phi(\mathbf{R}) \equiv \psi(\mathbf{R})\exp\left(\frac{U(\mathbf{R})}{k_{\mathrm{B}}T}\right) \tag{2.13}$$

Substituting $\phi(\mathbf{R})$ into Eq. 2.12, we have

$$\mathbf{J}(\mathbf{R}) = -\frac{k_{\mathrm{B}}T}{\xi}\exp\left(-\frac{U(\mathbf{R})}{k_{\mathrm{B}}T}\right)\nabla\phi(\mathbf{R}). \tag{2.14}$$

In a 1D case, $\mathbf{R}$ is reduced to x. $\mathbf{J}$ is constant everywhere, which can be replaced by J. Then we can rewrite the above equation into

$$\frac{\mathrm{d}\phi(x)}{\mathrm{d}x} = -\frac{\xi J}{k_{\mathrm{B}}T}\exp(\frac{U(x)}{k_{\mathrm{B}}T}).$$

At the absorbing boundary $x = x_{\mathrm{s}}$, we have $\phi(x_{\mathrm{s}}) = 0$, thus the solution of the last equation can be written as

$$\phi(x) = \frac{J\xi}{k_{\mathrm{B}}T}\int_{x}^{x_{\mathrm{s}}}\exp(\frac{U(x')}{k_{\mathrm{B}}T})dx'$$

The mean-first passage time is given by

$$\tau = \frac{1}{J}\int_{-\infty}^{x_{\mathrm{s}}}\psi(x)dx = \frac{1}{J}\int_{-\infty}^{x_{\mathrm{s}}}\phi(x)\exp\left(-\frac{U(x)}{k_{\mathrm{B}}T}\right)dx$$

Substituting Eq. 2.15 to the last equation gives

$$\tau = \frac{\xi}{k_{\mathrm{B}}T}\int_{-\infty}^{x_{\mathrm{s}}}dx\exp\left(-\frac{U(x)}{k_{\mathrm{B}}T}\right)\int_{x}^{x_{\mathrm{s}}}\exp\left(\frac{U(x')}{k_{\mathrm{B}}T}\right)dx'$$

The inner integral is dominated by x close to x_s, one can expand $U(x)$ near x_s, $U(x) \approx U(x_s) + (x - x_s)U'(x_s)$. The outer integral is dominated by the minimum

of the potential where $x = x_{\mathrm{b}}$, we can expand $U(x) \approx U(x_b) + (U''(x_b)/2) (x - x_b)^2$. Then the mean first-passage time is given by

$$\tau \approx \frac{\xi}{U'(x_{\mathrm{s}})} \sqrt{\frac{2k_{\mathrm{B}}T\pi}{U''(x_b)}} \exp\left(\frac{U(x_{\mathrm{s}}) - U(x_{\mathrm{b}})}{k_{\mathrm{B}}T}\right).$$

In Milner-McLeish theory, we have $U(x) = 3k_{\mathrm{B}}Tx^2/(2Nb^2)$, $\xi = N\xi_0/2$, $x_{\mathrm{b}} = 0$ and $x_{\mathrm{s}} = z$. Setting $k_{\mathrm{B}}T$ to 1, we get the relaxation time:

$$\tau_{\mathrm{MM}}(z) \approx \frac{\pi^{5/2}}{4\sqrt{6}}\tau_{\mathrm{R}}\frac{1}{s}\exp\left(\frac{3s^2}{2}\right), \tag{2.15}$$

where $s = z/\sqrt{Nb^2}$, τ_{R} is given by Eq. 2.7.

2.2.5 Asymptotic Solution

Base on the early works of Kifer [88], the asymptotic solution for the N-dimensional Kramers problem was obtained and proved rigorously by Meerkov [84, 89]. With a similar idea, Cao et al. [34] proposed an asymptotic solution, which gives

$$\tau(\Omega) \approx \frac{\xi}{U'_x(x_s, \mathbf{Y}_s)} \sqrt{\frac{2\pi k_{\mathrm{B}}T\det(\boldsymbol{\Sigma})}{\det(\Lambda_{ij})}} \exp\left(\frac{U(x_s, \mathbf{Y}_s)}{k_{\mathrm{B}}T}\right), \tag{2.16}$$

In this equation, the potential field $U(\mathbf{R})$ is redefined by rotated coordinates, as shown in Fig. 2.3. After rotation, the x-axis is perpendicular to the absorbing boundary Ω, $\mathbf{Y} = \{y_i\}$ are the axes of other dimensions orthogonal to x. The current close to Ω is assumed parallel to the x-axis, and dominated by the minimum of the potential on Ω: $(x_s, \mathbf{Y}_s)$. Λ is the Hessian matrix of the potential computed at the minimum of the potential in the original coordinates. $\boldsymbol{\Sigma}$ is a covariance matrix. Applying it to the arm-retraction problem, the relaxation time $\tau(z)$ in the limit of large N is given by

$$\tau(z) = \frac{\pi^{5/2}}{2\sqrt{6}}\frac{\tau_{\mathrm{R}}}{N}\frac{\sqrt{N}b}{z}\exp\left(\frac{3z^2}{2Nb^2}\right) \tag{2.17}$$

where τ_{R} is given by Eq. 2.7. This asymptotic solution is $2/N$ times smaller than the prediction of Milner-McLeish theory without constraint release (Eq. 2.15).
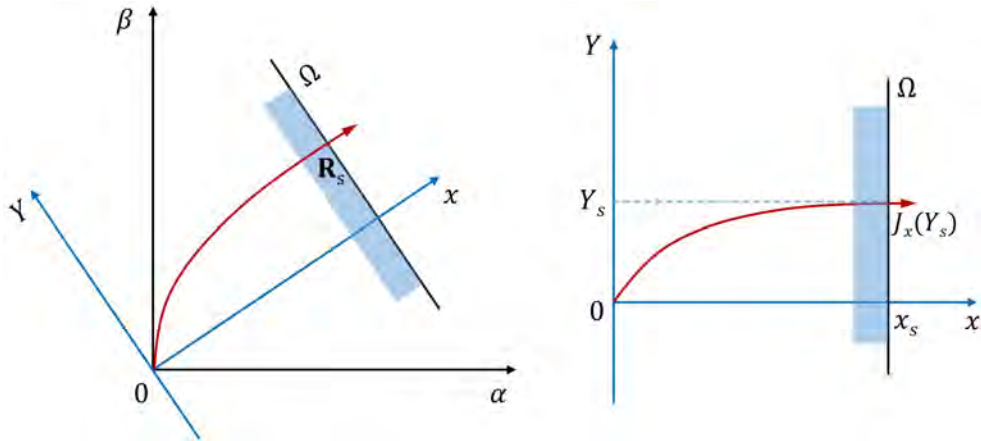
Figure 2.3: Coordinate rotation according to the absorbing boundary in the asymptotic theory. The left and right plots are before and after the coordinate rotation.

2.3   Advanced Numerical Methods

In the previous sections, we have shown some analytical solutions for the first-passage problems. These solutions can only predict the first-passage time in the limit of the infinitely high barrier. Apart from these analytical solutions, one can use numerical solutions, such as computer simulations, to solve the problems. However, rare events occur in a extremely low frequency, making them hardly observed in brute-force simulations.

In the past a few decades, great efforts have been put into the development of numerical methods that can accelerate the computer simulations on rare events. Starting from the initial idea of "reactive flux" [90, 91], several classes of methods have been developed, such as the "transition path sampling", the "conformation dynamics", and the "reactive trajectory sampling". In this part, we will test two advanced methods that have been reported with excellent performance on first-passage problems, namely the forward flux sampling [68] and weighted ensemble [69, 70, 85–87] methods, which belong to transition path sampling and reactive trajectory sampling respectively.

2.3.1 2D Kramers Problem

To test their performance, we will use the FFS and WE methods to solve the simplest multi-dimensional Kramers problem: the escaping time of a Brownian particle from a 2D harmonic potential well. The potential field is given by

$$U(x, y) = \frac{1}{2}\beta_x x^2 + \frac{1}{2}\beta_y y^2. \tag{2.18}$$

The equation of motion of the particle is

$$\xi \mathrm{d}\mathbf{r} = -\frac{\partial U(\mathbf{r})}{\partial \mathbf{r}}\mathrm{d}t + \sqrt{2\xi k_\mathrm{B}T}\mathrm{d}\mathbf{W}, \tag{2.19}$$

where $\mathbf{r} = (x, y)$. The absorbing boundary locates at

$$z = x + y. \tag{2.20}$$

This toy model is intrinsically analogous to the extension model of a 1D Rouse chain with only 2 beads.

The minimum of the potential on the absorbing boundary is at the point $(x_\mathrm{s}, y_\mathrm{s})$:

$$x_\mathrm{s} = \frac{\beta_y z}{\beta_x + \beta_y}, \quad y_\mathrm{s} = \frac{\beta_x z}{\beta_x + \beta_y}.$$

When $U(x_\mathrm{s}, y_\mathrm{s}) \gg k_\mathrm{B}T$, the current on $(x_\mathrm{s}, y_\mathrm{s})$ will dominate the flux through absorbing boundary. According to the asymptotic solution in Eq. 2.16, the first-passage time for this toy model is

$$\tau(z) = \left(\frac{\beta_x + \beta_y}{\beta_x \beta_y}\right)^{3/2} \left(\frac{k_\mathrm{B}T\pi}{2}\right)^{1/2} \frac{1}{z} \exp\left(\frac{\beta_x \beta_y z^2}{2(\beta_x + \beta_y)k_\mathrm{B}T}\right).$$

When the elastic coefficients are equal, $\beta_x = \beta_y$, this problem will be reduced into 1D case. Thus we should set different coefficients, e.g., $\beta_x = 1$ and $\beta_y = 10$. Then the analytical solution is given by

$$\tau(z) = \left(\frac{11}{10}\right)^{3/2} \left(\frac{k_\mathrm{B}T\pi}{2}\right)^{1/2} \frac{1}{z} \exp\left(\frac{5z^2}{11k_\mathrm{B}T}\right), \tag{2.21}$$

which will be compared with the FFS and WE results to test their accuracy.

2.3.2 Forward Flux Sampling Method

Unlike most transition sampling methods, FFS requires no *prior*-knowledge about the phase space density, but needs a clear definition of the **reaction coordinate**. The reaction coordinate could be any quantity that can characterize the transition process, whose choice in principle only affects the efficiency. Using the reaction coordinate, a sequence of non-intersecting interfaces λ_i $(i = 0 \ldots m)$ can be defined to divide the phase space into many layers. Through these interfaces, a set of consecutive samplings are performed instead of the brute-force simulation.
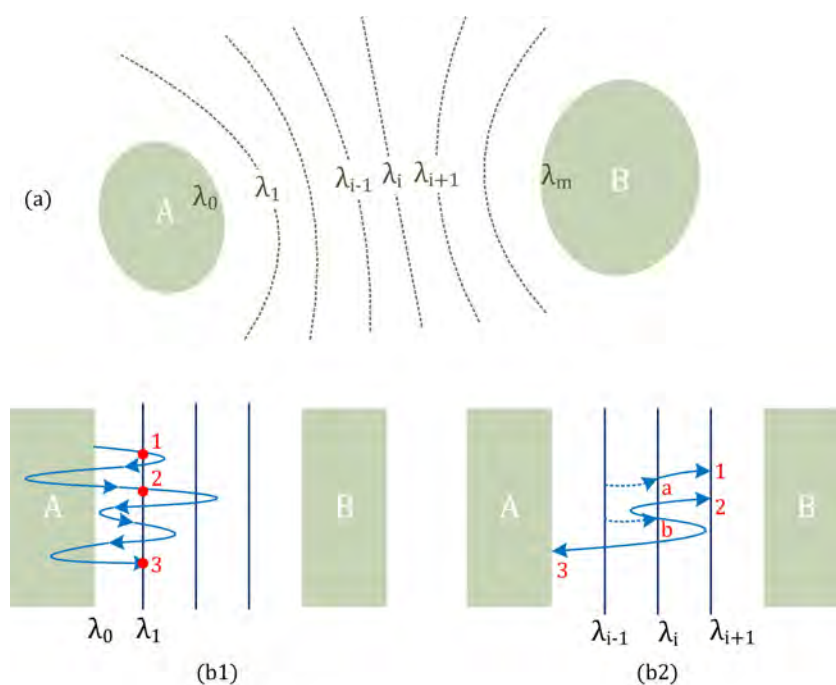
Figure 2.4: (a) The schematic plot of the interface definition in FFS for a general transition from state A to B. (b) The schematic plot of two FFS stages.

Consider a general transition from state A to B as shown in Fig. 2.4(a), and assume that the potential of state B is much higher than that of state A. The space between the two states have been divided by a set of interfaces, while the first interface λ_0 and the last interface λ_m are the borders of A and B. The standard FFS

method proceeds in two stages. In the first stage, a long simulation starting from A is continuously performed to explore the space. During this stage, the trajectory will cross the interface λ_1 many times, as shown in Fig. 2.4(b1). Among the crossing points, we count those last crossed interface λ_0 rather than λ_1, and recorded them in the database for λ_1, e.g., the 3 labeled crossing points in Fig 2.4(b1) will be counted. The result of this stage is the attempt frequency:

$$\nu_0 = N_0/T_0, \tag{2.22}$$

where N_0 is the number of counted crossings and T_0 is the simulation time.

In the second stage, a series of short consecutive samplings are performed from interface λ_1 to λ_{m-1}. For the interface λ_i, the sampling simulations start from the points on the interface (randomly selected from the database), as shown in Fig. 2.4(b2). These simulations finish when their trajectories either reach the next interface λ_{i+1} (successful run), or go back to the first interface λ_0 (unsuccessful run). The first arriving points of the successful runs on λ_{i+1} are recorded in the database for λ_{i+1}, e.g., points 1 and 2 in Fig. 2.4(b2). The fraction of successful runs gives an estimate of the probability to progress from one interface to the next, $P(\lambda_{i+1}|\lambda_i) = N_i/M_i$, where M_i is the total number of runs from λ_i to λ_{i+1}, and N_i is the number of successful runs. Thus the mean first-passage time from state A to a interface λ_n $(n \gg 1)$ is given by

$$\tau(\lambda_n) = \frac{1}{\nu_0} \left(\prod_{i=1}^{n-1} P(\lambda_{i+1}|\lambda_i) \right)^{-1}. \tag{2.23}$$

As shown in Fig. 2.5, the application of FFS method to the 2D Kramers problem is straightforward. Defining the reaction coordinate by $\lambda = x + y$. The first and last interfaces are $\lambda_0 = 0$ and $\lambda_m = z$. Other interfaces λ_i, $i = 1 \ldots m - 1$, are equally inserted between λ_0 and λ_m, demanding that the transition from A to B must cross all of them in sequence.
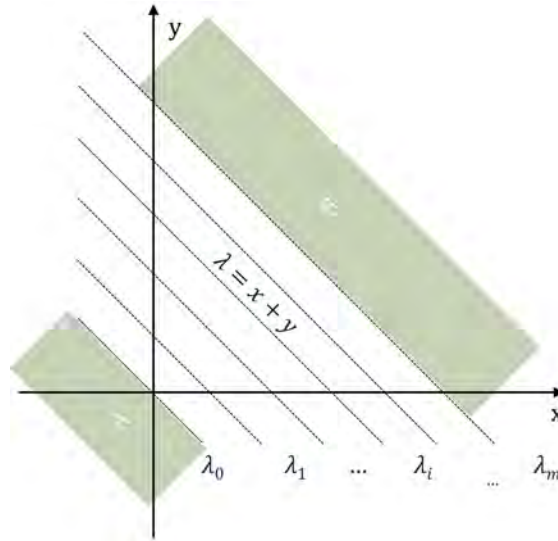
Figure 2.5: Application of the FFS method to the 2D Kramers problem.

Time-Step

In a Brownian dynamics simulation, the continuous trajectory is represented by the discrete movement steps, whose variance is proportional to the time-step Δt. Thus the precision of the simulation results strongly depends on Δt, because the variance of the movement steps determines the probability of an unobservable crossing event as shown in Fig. 2.6(a): a movement step (solid arrow line) shows no crossing while its real trajectory (dashed arrow line) has actually crossed the interface. Without counting these crossings, the first-passage time will be surely overestimated. In Fig. 2.7, the first-passage time τ from direct simulation are plotted at different Δt (circles). One can find τ decreases quickly with the reducing Δt. Fitting the data by a parabolic function, the extrapolated τ at $\Delta t = 0$ is 665, which is still smaller than $\tau = 690$ obtained at $\Delta t = 10^{-4}$. Therefore, the systematic error is non-negligible even with a small time-step.

To cope with this problem, Öttinger [92] presented an algorithm to predict the probability of the unobservable crossings. As shown in Fig. 2.6(a), l_1 and l_2 are the
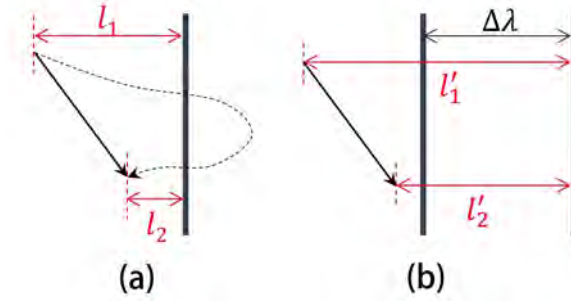
Figure 2.6: Setting parameters according to the Öttinger's algorithm: (1) time-step Δt, (b) interface distance $\Delta\lambda$.

distance of the particle to the interface before and after a time-step. The crossing probability of the real trajectory during this step is given by

$$P_{\text{cross}} = \exp(-\frac{l_1 l_2}{D\Delta t})., \tag{2.24}$$

where $D = k_{\text{B}}T/\xi$ is the short time diffusion coefficient of the reactive coordinate. Thus one can use a random number uniformly generated on $[0..1]$ and compare it with P_{cross} to determine whether the crossing happened or not. The results of the direct simulation optimized by this algorithm are the cubics in Fig. 2.7. For all time-steps, the results agree well with the extrapolated τ at $t = 0$ from direct simulations without Öttinger's algorithm.

Interface Distance

Intuitively, a small interface distance is in favour to enhance the transition rates between the neighbouring interfaces, especially for those with a steep potential barrier [93]. However, the Öttinger's algorithm requires that the interfaces distance cannot be too small, because it gives only the probability to cross one interface. When the interface are very close, the probability that the particle crosses more than one interfaces in Δt is non-negligible, which may cause a significant systematic error by underestimating the transition rate. To prevent this problem, a safe interface
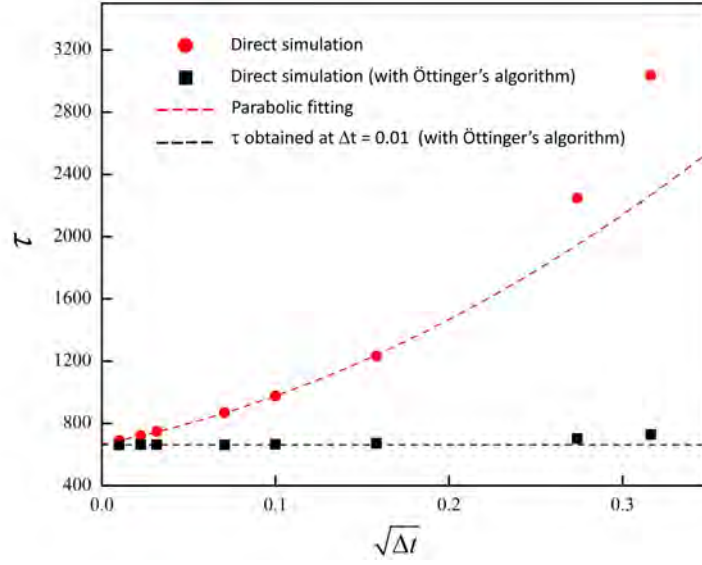
Figure 2.7: A comparison between the first-passage time τ obtained from the direct simulations with and without Öttinger's algorithm. The simulations are performed on the 2D toy model with an absorbing boundary at $z = 4$

distance should be calculated according to P_{cross}.

Define l_1' and l_2' as the distance of the particle to the second interface before and after a time-step Δt, as shown in Fig. 2.6(b). The probability to cross the second interface P_{2nd} must obey

$$P_{\text{2nd}} = \exp\left(-\frac{l_1' l_2'}{D\Delta t}\right) \leq \exp\left(-\frac{\Delta\lambda^2}{D\Delta t}\right), \tag{2.25}$$

where $\Delta\lambda$ is the interface distance. In the 2D case, the diffusion coefficient $D = 2$ when the friction coefficient on each axis ξ_0 and the energy $k_{\text{B}}T$ are set to unity. Assuming the crossing probability of the 2nd interface is negligible when it is smaller than 0.01, the safe distance can be obtained at different Δt, e.g., $\Delta\lambda > 0.3$ when $\Delta t = 0.01$, and $\Delta\lambda > 0.09$ when $\Delta t = 0.001$.

It must be noted that the distance $\Delta\lambda_0$ between λ_0 and λ_1 should be larger than other interface distances. Because the crossing points on λ_1 are obtained during a continuous simulation in the first stage, when λ_0 and λ_1 are too close, these

crossing points will be strongly correlated. In order to reduce the correlation, one should choose a larger distance, $\Delta\lambda_0$, and a longer simulation time, T_0. In our simulations, we set $\Delta\lambda_0$ to be 2.0, and other interface distances smaller: $\Delta\lambda = 0.5$ when $\Delta t = 0.01$, and $\Delta\lambda = 0.1$ when $\Delta t = 0.001$.

Systematic Error and Averaging Method

In a multi-dimensional problem, the exploration of the phase space is very expensive (there could be more than 100 dimensions in the 1D Rouse chain problem!). In the meantime, the FFS method works in a consecutive manner, which restricts the application of advanced techniques, such as the parallel computing. Therefore, instead of getting the first-passage time by a very long FFS simulation, it is better to conduct a series of short independent FFS runs (on different CPUs) and calculate the first-passage time by averaging their results, such that the computational cost on each CPU is much cheaper.

In order to investigate the errors due to the averaging methods, we perform the FFS simulations on the 2D case with an absorbing boundary at $\lambda_m = 14$, where the potential barrier is higher than $88k_{\mathrm{B}}T$. For all independent runs, the sampling number from each interfaces, M_i, must be identical to ensure an equal statistical weight of each trajectory. For convenience, M_i for all interfaces is set to be a constant. We compare the averaged results using two different sets of parameters: (1) $M_i = 10^4$ and $N_{\mathrm{ffs}} = 100$, (2) $M_i = 10^5$ and $N_{\mathrm{ffs}} = 10$, where N_{ffs} is the number of independent FFS runs in each case. One can find both sets have exactly the same total sampling numbers, $N_{\mathrm{ffs}}M_i$. M_i in first set is 10 times smaller than in the second one, thus the variance of its results is bigger, which means larger statistical error. For both parameter sets, the time step Δt is 0.001, and the interfaces distance $\Delta\lambda$ is 0.1.

In Fig. 2.8, $\tau(\lambda)$ is normalized by a factor $\lambda\exp^{-1}(U_{\mathrm{min}}(\lambda))$, such that $\tau(\lambda)$ should approach to a plateau when $\lambda \gg 1$ (see Eq. 2.21). The triangle symbols in
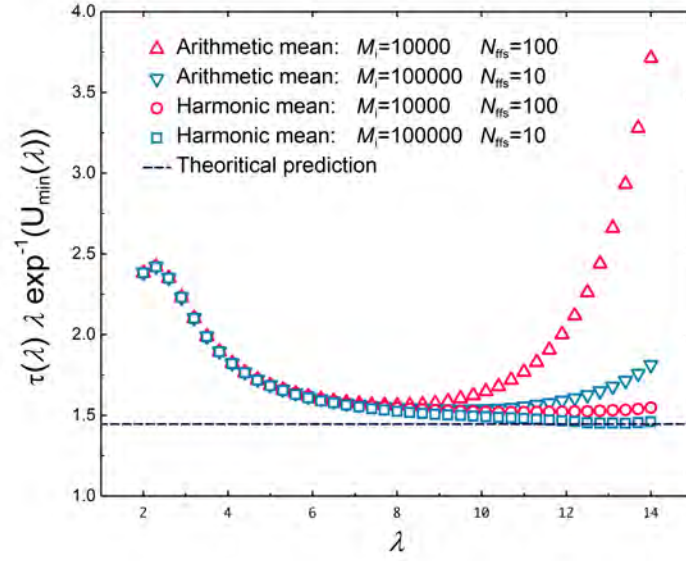
Figure 2.8: First-passage time $\tau(\lambda)$ obtained by arithmetic and harmonic means from the 2D Kramers problem.

Fig. 2.8 represent the results by **arithmetic mean**,

$$\tau(\lambda) = \frac{1}{N_{\text{ffs}}} \sum_{k=1}^{N_{\text{ffs}}} \tau_k(\lambda)$$

where $\tau_k(\lambda)$ is the mean first-passage time obtained in k-th independent run. When $\lambda < 4$, $\tau(\lambda)$ is much higher than the asymptotic solution, due to the low energy barrier at the early stages. With increasing λ, $\tau(\lambda)$ is suppose to gradually converge to the predicted value (dashed line in Fig. 2.8). However, after $\lambda = 8$, the normalized $\tau(\lambda)$ values obtained by using the first parameter set deviate from the plateau value and increases sharply. For the second parameter set, similar deviation happens at slightly larger λ (after $\lambda = 10$), and the growth rate is lower than that using the first set. Also, such unexpected behaviour seems related to the sampling number M_i. If we keep increasing M_i, the deviation of $\tau(\lambda)$ from predicted value happens at larger λ.

We consider this deviation as a systematic error arising from the averaging

method. Arithmetic mean is valid only when these independent runs have exactly the same statistical weights. In FFS, there are a few samples which have very long $\tau(\lambda)$ (many times of the expected value), which will dominate the arithmetic mean and so lead to unrealistic large mean value. We can compare this averaging method with one direct simulation. In a continuous long run, $\tau(\lambda)$ can be calculated by the total simulation time divided by the number of first crossings on the boundary λ (those last crossed λ_0 now crosses λ), because the time spent from λ back to λ_0 is negligible comparing to $\tau(\lambda)$. In a continuous run, the trajectories that arrive λ with a shorter period of time will also return to the λ_0 immediately to start another trip to λ, which means these faster trajectories have higher probability or higher statistical weights. It implies that $\tau(\lambda)$ should be calculated by the **harmonic mean**

$$\tau(\lambda) = \frac{N_{\mathrm{ffs}}}{\sum_{k=1}^{N_{\mathrm{ffs}}} 1/\tau_k(\lambda)}. \tag{2.26}$$

As shown in Fig. 2.21, the circles and squares representing the harmonic means are very close to each other and both converge to the asymptotic line. Additionally, a general observable A associated to the interface (eg. the first-passage point on the interface) could be averaged by the following equation:

$$A(\lambda) = \frac{\sum_{k=1}^{N_{\mathrm{ffs}}} A_k(\lambda)/\tau_k(\lambda)}{\sum_{k=1}^{N_{\mathrm{ffs}}} 1/\tau_k(\lambda)}, \tag{2.27}$$

where $A_k(\lambda)$ is the observable obtained in k-th FFS run. Replacing $A_k(\lambda)$ by $\tau_k(\lambda)$, this equation is exactly the same as Eq. 2.26.

It should be noted that the harmonic mean is not an universal averaging method for all first-passage time problems. For example, we will use arithmetic mean in the first-passage problem of slip-spring model discussed in next chapter. This is because there are many starting states, while the transitions between them are also rare events. In that case, the faster arriving trajectories have the same statistical weight as the slower ones.

2.3.3   Weighted Ensemble Method

The WE method was first proposed by Hurber and Kim [69], who employed it in Brownian dynamics simulations to study binding process in protein. Rojnuckarin et al. [85] used this method to explore the configuration space of folded coarse-grained proteins. Later, Zhang et al [70] extend the WE method to a broad class of stochastic dynamics. Recently, Darve et al. [86, 87] improved the resampling algorithm, making it applicable to various transition problems.

In the WE method, the phase space is divided into many non-overlapping domains, as shown in Fig. 2.9. These domains could be hexagons (Fig. 2.9(a)), layers (Fig. 2.9(b)), or any other arbitrary shapes. For convenience, the domains in the 2D Kramers problem are defined by the non-intersecting interfaces similar to the FFS method; therefore, we call the domains as "layers" in discussion. In simple words, the WE method works as running a lot of parallel brute-force simulations with different priorities. Such priority is weighted by so-called **"resampling"** algorithm.
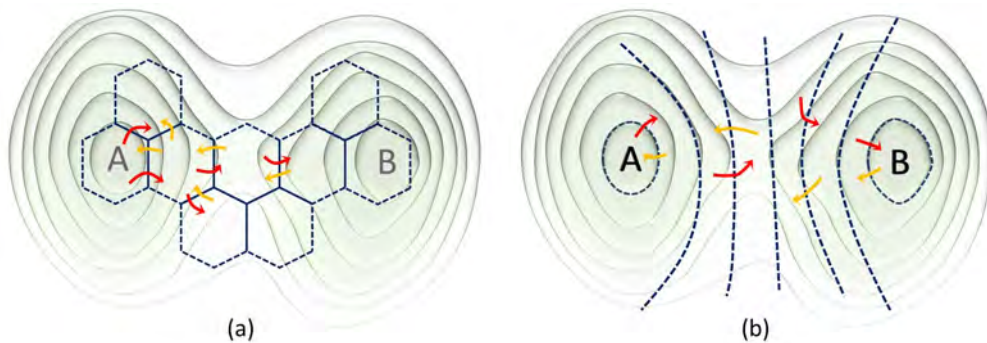
Figure 2.9: Domains in WE method.

Before applying the WE method to a specific problem, it is necessary to introduce the general idea of resampling. Resampling is a flexible algorithm that duplicates or kills the sample elements without changing their distributions. Consider a collection of numbers which follow the Gaussian distribution with an average of 0. For convenience, we set the weights of the numbers to be 1. If we randomly delete half

of the numbers, and double the weights of the rest (or keep their weights to be 1 but duplicates the rest of the numbers), the distribution and the sum of weights does not change. Supposing we are more interested in the numbers larger than 0, another resampling algorithm with two steps could be taken: (1) find all the numbers smaller than 0, delete half of them and increase the weights of the other half to 2; (2) find all the numbers larger than 0, randomly duplicate half of them and let their copies take half of their weights. With these resampling steps, a new collection of numbers are created, which is dense in the particular part of interest and sparse on the rests.

In the WE method, the mean first-passage time to an absorbing boundary λ is calculated by

$$\tau(\lambda) = \frac{W_0 t}{\sum_{j=1}^{N_\lambda} w_j^\lambda}, \tag{2.28}$$

where t is the simulation time, N_λ is the total number of trajectories which have crossed the interface λ, w_j^λ is the weight of j-th trajectory that has crossed λ, the constant W_0 is the total weight of the trajectories in the system. Similar to Eq. 2.27, a general observable associated to λ, $A(\lambda)$, can be calculated by

$$A(\lambda) = \frac{\sum_{j=1}^{N_\lambda} w_j^\lambda A_j(\lambda)}{\sum_{j=1}^{N_\lambda} w_j^\lambda} \tag{2.29}$$

Resampling Algorithm

Apparently, one can design his resampling procedure. However, it is rather difficult to find a balance between efficiency and accuracy. In the early WE method for Brownian dynamics, new trajectories are created by splitting the weights of the older ones, leading to a strong polarisation on the weights of trajectories in each layer, i.e. some trajectories have very large weights while the others are very small. Such polarisation makes the results hard to converge to the correct value. Recently, an advanced resampling algorithm without suffering such polarisation has been proposed [87]. Briefly, this resampling algorithm tend to delete the elements with small weights and split the elements with large weights; therefore, this method not only

keeps a constant number of elements but also keeps the weight of the elements equal in each domain.

We use Fig. 2.10(a1) and 2.10(a2) to explain the resampling algorithm adopted in the 2D case. In Fig. 2.10(a1), there are 3 trajectories labelled by different colours in the first layer Λ_1. Define the weight of the red, blue and grey trajectories are, respectively, w_r, w_b and w_g ($w_r > w_b > w_g$). Suppose the expected number of trajectories in each layer is $M_\Lambda = 2$, the first step of the resampling algorithm is to kill one trajectory and give its weight to another. Because the red trajectory carries the greatest weight, the choice would be made between the other two trajectories. Since the survival probability of a trajectory is proportional to its weight, one can uniformly generate a random number on [0...1]; if it is larger than $w_g/(w_b + w_g)$, we kill the grey trajectory and add its weight to the blue one, and vice versa. In the example of the layer Λ_1 in Fig. 2.10(a2), we keep the blue trajectory, whose weight becomes $w_b' = w_b + w_g$. If $w_r = w_b'$, the resampling is finished, otherwise further steps must be taken. For example, in layer Λ_2 of Fig. 2.10(a1), the red trajectory has larger weight than the blue one, $w_r > w_b$, and their average is $\bar{w} = w_r + w_b$. Because $w_r > \bar{w}$, we split the red trajectory into two, their weights are $w_r' = \bar{w}$ and $w_r'' = w_r - \bar{w}$, respectively. Now, it turns into the situation in layer Λ_1, and one should repeat the previous step. The iteration terminates when the trajectory number is M_Λ in layer Λ and their weights are equal.

Parameters

For the 2D case, the simplest layer definition is equally dividing the phase space by a set of interfaces as in the FFS method. But this definition can be further improved by adjusting the width of the layers. Since the total weight of trajectories in each layer roughly follows Boltzmann distribution at steady state, it is reasonable to set density of the interfaces sparse at the bottom of the potential field and dense close to the absorbing boundary, as shown in Fig. 2.10(b). Because only the absorbing
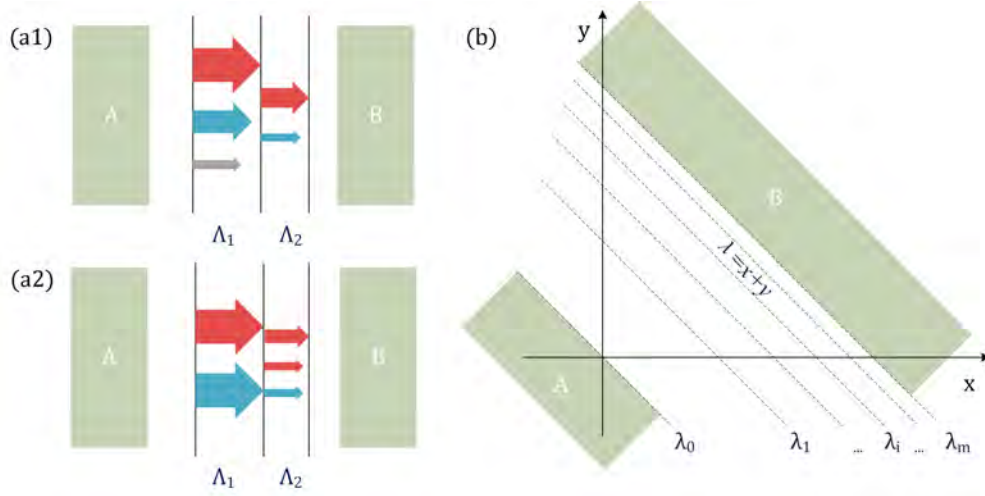
Figure 2.10: (a) Resampling algorithm. (b) Definition of interfaces for the WE method in the 2D Kramers problem.

boundary λ_m requires the judgement of crossing by the Ötinger's algorithm, small interface distance is not an issue in WE simulations. In our case, the coordinates of interfaces are given by

$$\lambda_i = -\frac{z}{m^2}i^2 + \frac{2z}{m}i \quad i = 1, 2, ..., m,$$

(2.30)

which is a parabolic function whose maximum locates at $\lambda_m = z$.

Apart from the layer definition, the performance of the WE methods also depends on a few parameters, i.e., the resampling frequency f_{rs}, the number of layers m, and the expected trajectory number m_Λ in each layer. We separately investigated these parameters on the 2D Kramers problem with an absorbing boundary at $\lambda = 9$. As shown in Fig. 2.11(a), higher resampling frequency is always in favour to raise the hitting rate on the absorbing boundary, $N_\lambda/t_{\mathrm{cpu}}$, where t_{cpu} is the CPU time. Therefore, the resampling procedure should be taken every time-step. In Fig. 2.11(b), we fix M_Λ to 20 for all layers, and change m from 10 to 30. The real-time first-passage time τ^{we} has been normalized by the asymptotic value τ^{asy} from Eq. 2.21, such that it should converge to 1. On can find that the convergence rate with
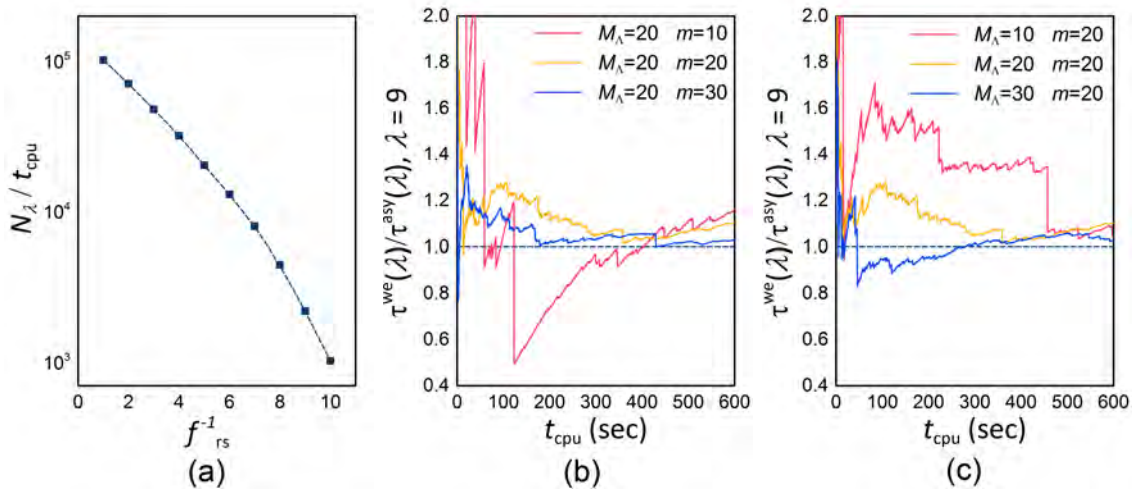
Figure 2.11: WE method performance with different parameters: (a) the resampling frequency f_{rs}, (b) the number of layers m, (c) the expected trajectory number in each layer M_Λ.

more layers is higher than that with less layers. In Fig. 2.11(c), the number of layers is fixed, M_Λ changes from 10 to 30. It is found that the convergence rate for $M_\Lambda = 30$ is much higher than the other two. In addition, such convergent behaviour implies that one should let the system to relax before collecting the data, which can significantly reduce the noise at the beginning.

2.3.4 A Comparison Between FFS and WE Methods

In this section, we will compare the results of the FFS and WE methods on the 2D Kramers problem. The simulations are perform on the same CPU core (Intel Xeon E5-2620). The parameters are set as follows. The time-step Δt is 0.01 for both methods. In the FFS simulations, the interfaces distance $\Delta \lambda$ is 0.5. For each interface, the number of sampling M_i is 10^5. The number of independent FFS runs is $N_{ffs} = 100$, which is sufficient to provides good statistics. In the WE simulations, layer definition is given by Eq. 2.30 with m equals 20. Each layer contains $M_\Lambda = 20$
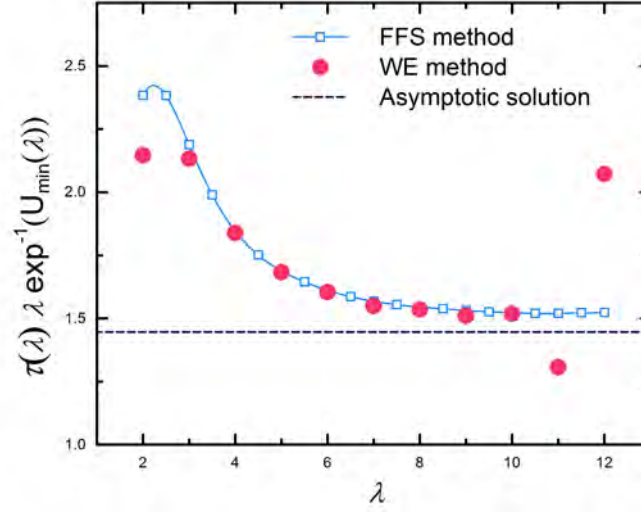
Figure 2.12: First-passage time obtained from the FFS and WE methods (symbols) and the theoretical predictions of Eq. 2.21 (dashed line).

trajectories. All WE simulations must have a relaxation period over 600 seconds before collecting the data.

The mean first-passage time $\tau(\lambda)$ obtained by different methods are shown in Fig. 2.12. Owing to their mechanisms, the FFS method manages to get the spectrum of $\tau(\lambda)$ for all interfaces in a single run, while the WE method has to set up independent runs for each interface λ. Generally, the results from both methods are consistent apart from the early region $\lambda < 4$ and the late region $\lambda > 10$. When $\lambda < 4$, the energy barrier is relatively low. Since the WE simulation is close to brute-force simulation, the results from the WE method are more precise for lower energy barrier, while the FFS method is precise only when the energy barrier is much higher than $k_{\mathrm{B}}T$. When $\lambda > 10$, the WE data show a sharp deviation from the plateau and fails to converge even after a long run. The deviations are random and could be alleviated by increasing m and M_Λ. Nevertheless, it reveals a risk of the WE method on solving the first-passage time problems, because the users cannot predict if the parameters are still safe for current potential barrier. In contrast, the precision of
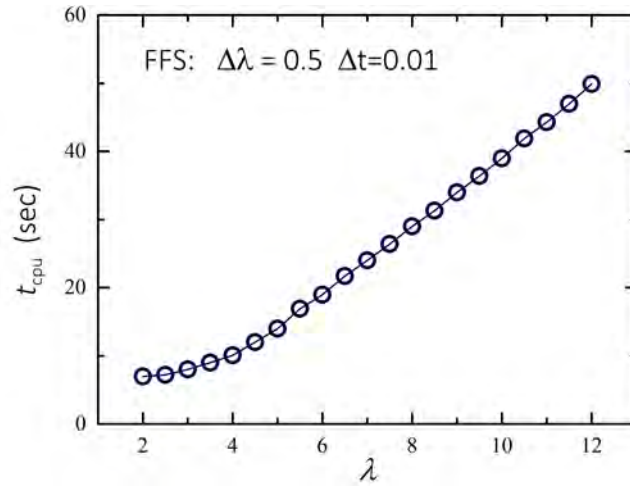
Figure 2.13: Time-cost of the FFS simulation to reach each interface in the 2D Kramers problem.

FFS method is controllable by monitoring the conditional probability $P(\lambda_{i+1}|\lambda_i)$. When $P(\lambda_{i+1}|\lambda_i)$ drops to a dangerous level, one can accordingly increase M_i. As a consequence, the FFS method is more advanced on the accuracy and stability.

On efficiency, both methods have good performance. The WE method approximately takes less than 600 seconds to converge as shown in Fig. 2.11, while a single FFS simulation is even faster, which requires merely about 50 seconds to reach $\lambda = 12$, as shown in Fig. 2.13. On parallel computing, WE is stronger than FFS, but the latter allows a remedy by simulating lots of independent runs. Considering its advantage on exploring the whole spectrum in one run, FFS is still a better choice.

Apart from $\tau(\lambda)$, there are some other observables related to the interfaces could be obtained via Eq. 2.27 and Eq. 2.29. For example, the coordinates of the average first arriving points on interfaces, $(x_{\mathrm{fp}}(\lambda), y_{\mathrm{fp}}(\lambda))$. Since $x_{\mathrm{fp}}(\lambda) + y_{\mathrm{fp}}(\lambda) = \lambda$, we only plot $y_{\mathrm{fp}}(\lambda)$ in Fig. 2.14. It is found that $y_{\mathrm{fp}}(\lambda)$ obtained by FFS and WE method are consistent. The first arriving points are all on one side of $y_{\mathrm{s}}(\lambda)$, but gradually converge to it.
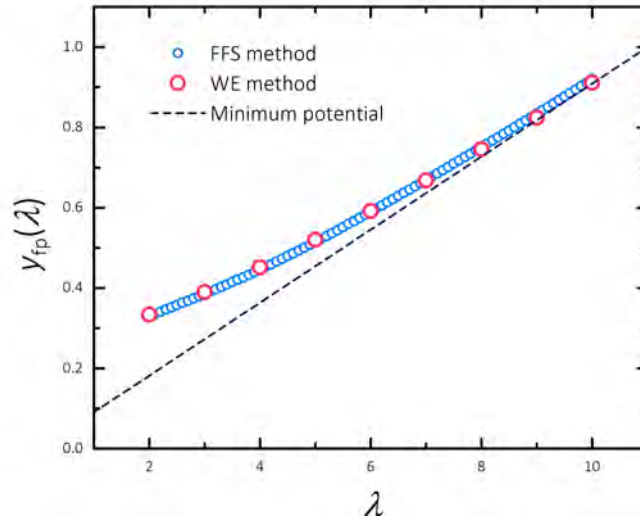
Figure 2.14: First arriving point on each interface $y_{\text{fp}}(\lambda)$ obtained from the WE and FFS simulations for the 2D Kramers problem (circles) and the minimum of the potential (dashed line).

In conclusion, the FFS method performs better than the WE method in this 2D case, and will be employed in the following study on the 1D Rouse chain model. Nevertheless, it must be noted that WE method still has some remarkable advantages over FFS method, such as the flexibility on defining the domains and its mechanism close to the brute-force simulation, which makes it widely applicable to some complicated rare events, such as the protein folding.

2.4 Computer Simulation Study on 1D Rouse Chain Model

In Sec. 2.2.1 and 2.2.2, we have introduced the relationship between the arm retraction and the extension of the 1D Rouse chain with one end fixed. By coarse-graining, Milner and McLeish [30, 37] reduced the multi-dimensional first-passage problem into a 1D Kramers problem, and proposed an approximate solution (see

Sec. 2.2.3 and 2.2.4). Cao et al. [34] proposed an exact asymptotic solution for multi-dimensional first-passage problems and predicted a result smaller than the prediction of Milner-McLeish theory (see Sec. 2.2.5). In this section, both the direct (brute-force) and FFS simulations will be applied to the 1D Rouse chain model to examine the analytical solutions.

We perform computer simulations with variable number of beads representing the Rouse chain. The bead friction ζ_0, energy $k_B T$, and statistical segment length b are set to be unity in the simulations without loss of generality, whereby the units for length, time and energy are respectively b, $\zeta_0 b^2/k_B T$, and $k_B T$. The predictor corrector method [94] was employed in simulations. The detection of trajectories crossings on interfaces is improved by Öttinger's algorithm [92].

2.4.1 Direct Simulation

Direct simulation results are plotted in Fig. 2.15. The horizontal axis is $s = z/\sqrt{Nb^2}$, where z is the end-to-end distance or extension length, N increases from 1 to 128. In a continuous simulation, when the free end last crossing $s_0 = 0$ reaches $s > 0$ for the first time, its time cost is recorded as the first-passage time for s. Fig. 2.15(a) shows decimal logarithm of the mean first-passage time. Clearly, the time grows very fast with s, approximately as $\exp\left(3s^2/2\right)$ as expected. The direct simulation can approach $\tau(s) \approx 10^7$ or so. Fig. 2.15(b) shows the same data but normalized by $\tau(s)s\tau_R^{-1}\exp\left(-3s^2/2\right)$. For clarity, both predictions by Milner-McLeish theory and asymptotic solution are divided by the trivial factor $\exp\left(-3s^2/2\right)$. Such normalization brings all data with one decade in vertical scale and allows clear comparison between theories and simulations. In particular, the direct simulation are significantly faster than the Milner-McLeish prediction (dotted-dashed line) when N is larger.
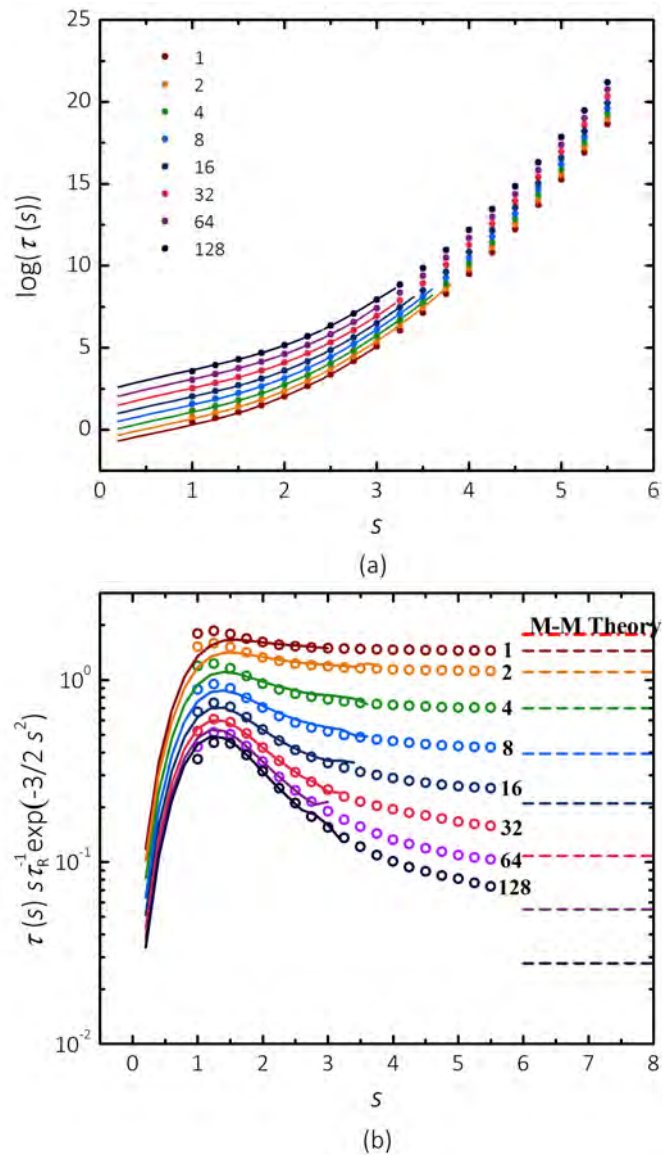
Figure 2.15: (a) The decimal logarithm of first-passage time $\tau(s)$ for FFS simulations (dots) and direct simulations (solid lines). (b) Normalized $\tau(s)$ versus s for FFS simulations (circles) and direct simulations (solid lines), the dashed lines are the prediction of Eq. 2.17. Milner-McLeish Theory is shown by the red dotted-dashed line
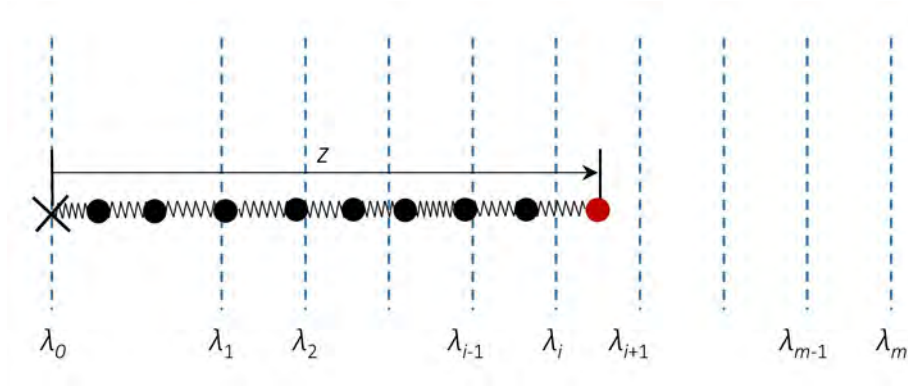
Figure 2.16: Applicaiton of FFS method onto 1D Rouse chain extension model

2.4.2   FFS Simulation

In order to extend simulation results to longer times and facilitate detailed theory verification and calibration, we also performed FFS simulation of the same model. First of all, we need to define the reaction coordinates and the non-intersecting interfaces, which is quite straightforward in this model. As shown in Fig. 2.16, the extension length z is employed as the reaction coordinate. The original interface λ_0 is define at $z = 0$, other interfaces are placed according to

$$\lambda_i = (1 + 0.25 \times (i - 1)) \, N^{1/2} b, \quad i = 1, 2, \ldots \tag{2.31}$$

Such interface definition avoids the systematic errors due to very small interface distance and large statistical errors due to large interface distance.

The simulation then proceeds in two stages. In the first stage, we run one long simulation for time T_0 and count the number of crossings, N_0, of the first interface λ_1 by the trajectories which last crossed interface λ_0, rather than λ_1. Besides counting the crossings, we store the full chain configurations at the moments of these crossings.

In the second stage, we run many short consecutive simulations for interfaces 1 to $n - 1$ in sequence. For the interface λ_i, the simulation starts from the stored points on the interface λ_i (selected at random from the database) and finish when they either reach the next interface λ_{i+1}(successful run), or go back to the 0-th interface

(unsuccessful run). The fraction of successful runs N_i/M_i gives an estimate of the probability to progress from one layer to the next, $P(\lambda_{i+1}|\lambda_i)$, where M_i is total number of runs from layer i, and N_i is the number of successful runs. Thus, the mean first-passage time is given by Eq. 2.23.

The value of M_i has a decisive effect on the statistical error of the final outcome, with the best strategy to increase M_i for higher energy barriers between the layers to ensure an approximately constant N_i. A simple way to determine M_i is to run a few simulations with smaller M_i and get the rough ratio of $P(\lambda_{i+1}|\lambda_i)$, and estimate M_i for an expected N_i. Ref. [93] recommends selecting interface distances such that $P(\lambda_{i+1}|\lambda_i) > 0.3$. Our selection satisfies this criteria. By running a quick simulation for $N = 1$, the proper M_i can be obtained. Using the same M_i and the same distance defined by s for $N = 1$, a proper ratio $P(\lambda_{i+1}|\lambda_i)$ for larger N is also guaranteed since the $P(\lambda_{i+1}|\lambda_i)$ increases with larger N.

In Sec. 2.3.2, the difference between the harmonic and arithmetic means has been discussed. In Fig. 2.17, we compare the two averaging methods on the chain with 32 beads. The averaging are performed on two samples: (1) $N_i = 10^3$ and $N_{\text{ffs}} = 100$, (2) $N_i = 10^4$ and $N_{\text{ffs}} = 10$. Despite the variance $\langle(\tau(s) - \langle\tau(s)\rangle)^2\rangle$ for $N_i = 10^4$ is much larger than that for $N_i = 10^3$, their harmonic means are consistent, allowing us to reduce the computational cost of a single run by performing a lot of independent runs on different CPUs. This method is very useful when the extension length is long.

The mean first-passage time $\tau(s)$ for different chain lengths N are presented in Fig. 2.15. Comparing with direct simulations, a disagreement can be found at $s < 1.5$. In this region, the first-passage time given by the FFS method is inaccurate since the energy barrier is lower than $3.5k_BT$. In the region of $s > 1.5$, two simulation methods are consistent with each other. FFS method is able to predict the first-passage time till $s = 5.5$, with the chain length up to $N = 128$.

In the normalized plot in Fig. 2.15(b), all curves show a fast decay for the
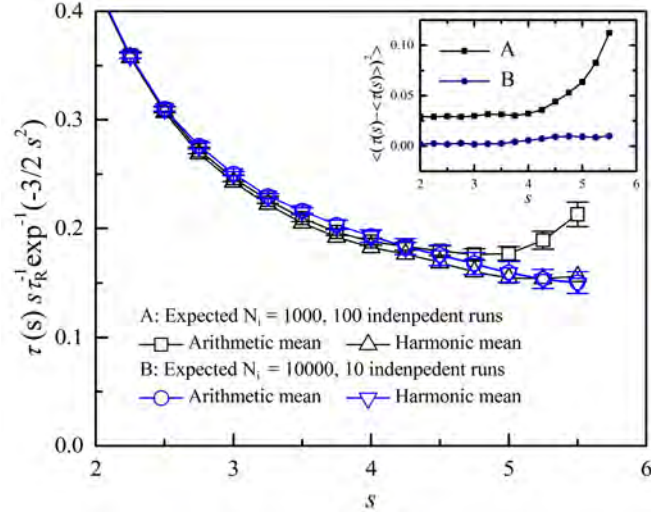
Figure 2.17: A comparison between arithmetic and harmonic mean for averaging independent FFS runs of 1D Rouse chain model.

intermediate values of s and then gradually saturate around certain transition length s_t with clear plateau reached in the systems with small N values. The slopes of the curves from the peak to s_t increases with increasing N. In the mean time, the transition length s_t also increases. One finds that the result differs from the Milner-McLeish theory significantly. When increasing N, the first-passage time becomes much shorter than their prediction, leading to the difference of a factor of 10 at $s = 3$ and $N = 128$, and even bigger for larger s and N. This shows conclusively that the one mode assumption of the Milner-McLeish theory is inadequate and better theory must be developed. Note that this discrepancy is much bigger than the 20% reported by Vega et.al. [95].

The results of FFS simulations verifies asymptotic solution in the limit of large extension ($z \sim Nb$), where the prefactor of $\tau(z)$ has z^{-1} scaling. In the intermediate regime, FFS results show different scaling behaviour, which is roughly $\tau(z) \sim z^{-3}$. In Ref. [34], Cao et al. combined the asymptotic solution at large s and the one in the intermediate regime (calculated by so-called **"minimum action path"**), and

proposed an empirical expression:

$$\tau(s) = \left(\frac{C_1(N)}{Ns} + \frac{C_2(N)}{s^3}\right) \tau_{\mathrm{R}} \exp\left(\frac{3s^2}{2}\right), \tag{2.32}$$

where $C_1(N)$ is given by

$$C_1(N) = \sqrt{\frac{32\pi}{3}} N^2 \sin^2\left(\frac{\pi}{4(N + 1/2)}\right), \tag{2.33}$$

$C_2(N)$ is a fitting parameter. By fixing $C_1(N)$, $C_2(N)$ is obtained by fitting the FFS simulation results, whereby a combination of the theory and FFS simulation leads to a simple expression for the first-passage time

$$\tau(s) = \tau_{\mathrm{R}} \left(\frac{3.57}{Ns} + \frac{1}{(N^{-1.41} + 0.83)\, s^3}\right) \exp\left(\frac{3s^2}{2}\right). \tag{2.34}$$

2.5 Conclusions

In this work, we have studied the first-passage problem of the 1D Rouse chains, as a proxy for dynamics of arm retraction of isolated star polymers in a network. In the widely known Milner-McLeish theory, star arms are represented by Rouse chains inside their confining tubes and further replaced by one bead attached to the branch point by a harmonic spring [30]. The mean disengagement time of a tube segment is $\tau(z) \sim z^{-1} \exp\left(U(z)/k_{\mathrm{B}}T\right)$. In order to check the validity of the Milner-McLeish theory, Cao et al. [34] proposed an asymptotic solution to solve the multi-dimensional Kramers problem. This asymptotic solution is only valid in the limit of very large extensions $z \sim Nb$, corresponding to a fully extended chain. The results show that the mean first-passage time drops significantly if the arm is represented by Rouse chain with more beads instead of a single bead.

Because the large deviations of the 1D Rouse chain rarely happen, the verification of the asymptotic theory by a direct simulation is practically impossible. To cope with it, we can employ the advanced numerical methods for first-passage problems. Two advanced methods, i.e., forward flux sampling and weighted ensemble methods,

were tested on a 2D Kramers problem, which is a simplest multi-dimensional first-passage problem. Considering their performance on all aspects, such as accuracy, efficency and stability, the FFS method was chosen to investigate the 1D Rouse chain model. The results of the FFS simulations are in good agreement with the asymptotic solutions at very large extension. In the intermediate regime, $\tau(z)$ shows richer scaling behaviours.

Chapter 3

Arm Retraction Dynamics of Entangled Star Polymers: The First-Passage Problem in Slip-Spring Model

3.1 overview

Development of quantitative theories for predicting the dynamic and rheological properties of entangled branched polymers is of both fundamental and practical importance. In the past decades, theoretical efforts have been primarily based on the concept of tube model originally proposed by de Gennes, Doi and Edwards [16, 17, 24]. Different from entangled linear polymers where reptation, contour length fluctuations (CLF) and constraint release (CR) are the main relaxation mechanisms, reptation in branched polymers is strongly suppressed due to the effectively localized branch points. In the simplest case of symmetric star polymers, the stress relaxation is conjectured to proceed via CLF or arm retraction by which the free end of an arm retracts inward along the primitive path to escape from the original

76

tube segments and pokes out again to explore new tube. Since arm retraction is entropically unfavorable and so thermally activated, this process can be formulated into a first-passage (FP) problem or Kramers problem.

A star arm retracting in a fixed network experiences a potential barrier theoretically described by a quadratic function $U(s) = \nu k_{\mathrm{B}} T Z s^2$ where k_{B} is the Boltzmann constant, $Z = M/M_{\mathrm{e}}$ is the number of entanglements per arm, M the arm molecular weight, M_{e} the entanglement molecular weight and ν a constant [26]. The fractional coordinate s measures the retraction depth of the arm free end. Pearson and Helfand predicted an exponential dependence of the arm terminal relaxation time, τ_{d}, and correspondingly the viscosity, η_0, on the arm molecular weight, $\eta_0 \sim \tau_{\mathrm{d}} \sim \exp(\nu M/M_{\mathrm{e}})$ [27]. This prediction however shows large discrepancy from experimental data obtained in star polymer melts due to the neglect of CR effects. Ball and McLeish [28] took into account the CR effects by applying the dynamic tube dilution (DTD) hypothesis [29] where the relaxed arm segments are considered to work as effective solvent for the unrelaxed materials. Milner and McLeish further improved this theory by including the contributions of fast Rouse fluctuations at early times and solving the first-passage problem of a diffusing end monomer to retract a fractional distance s to get the arm relaxation spectrum $\tau(s)$ at late times [30, 37]. The Milner-McLeish theory predicts the stress relaxation of symmetric star polymer melts reasonably well, but not the dielectric or arm end-to-end vector relaxation function. It also encounters difficulty in using a single set of model parameters to describe the rheological behaviors of asymmetric star polymers with different short arm lengths [36]. In recent years computational models based on the framework of Milner-McLeish theory have been developed for describing the linear viscoelasticity of branched polymers with arbitrary architectures and their general mixtures [39, 42, 44, 47, 96]. These models have been shown to provide predictions in reasonably good agreement with experimental data for a variety of systems, but are facing problems in describing the linear rheology of some simple mixtures,

such as the star-linear blends, especially at low fractions of star polymers [44, 97]. Therefore more quantitative theories that can simultaneously predict different dynamic and rheological properties of entangled branched polymers are still highly desired. The development of such theories requires the analytical solution of the multi-dimensional FP problem of arm retraction [34].

On the other hand, the coarse-grained slip-link or slip-spring (SS) simulation models have demonstrated strong potential in describing dynamics and rheology of entangled polymers [59, 60, 64, 66, 98–101]. For example, the single-chain slip-spring model developed by Likhtman [66] can provide simulation results on multiple experimentally measurable observables, such as neutron spin echo, linear rheology, dielectric relaxation and diffusion. Using a limited number of fitting parameters, the predictions of this model match the results obtained from both experiments and molecular dynamics (MD) simulations on linear and symmetric star polymers very well [81–83, 101]. The SS model serves as an intermediate between tube theory and MD simulations. As a discrete model, it not only naturally builds in all the relaxation mechanisms of the tube model, but also carries more system details, such as explicit polymer chains and entanglements [102]. At higher level of coarse-graining, the SS model is significantly more efficient than MD simulations using bead-spring polymer model, which is of great advantage in the study of branched polymers. Furthermore, the slip-spring model can separate the contributions from different relaxation mechanisms by enabling some of them while disabling others. This is particularly helpful for examining assumptions made in current theoretical models and providing valuable information for developing more quantitative models. One typical application is to evaluate the magnitude of constraint release effects by comparing simulation results obtained from entangled polymer systems with and without CR.

Since deep arm retractions are rare events due to the high energy barrier, the time and length scales accessible to standard slip-spring simulations are still much

shorter than those in well-entangled experimental systems where the tube models are supposed to work best. Similar problems have also been seen in brute force simulations of many other rare events, such as crystal nucleation [103, 104], biological switches [68] and protein folding [105]. The required computational time may take up to several decades [106]. Advanced numerical techniques, such as the umbrella sampling [107] and transition path sampling [108] methods, have to be employed to accelerate the simulations. Recently the forwards flux sampling (FFS) method has been proposed [68, 93, 109] and proven to be successful in molecular dynamics and Monte Carlo (MC) studies of rare events [106, 110].

In this chapter, we will combine the FFS method with the slip-spring model for studying the dynamics of entangled symmetric star polymers. This is a proof-of-concept work. To our knowledge there seems no other reported work in the literature on applying the transition path sampling methods to study entangled polymer dynamics, especially on arm retraction dynamics. We will mainly focus on the systems without constraint release for the following reasons: 1) It is relatively convenient to implement the FFS method and find an appropriate reaction coordinate in the non-CR systems; 2) The terminal relaxation times in the systems without CR are much longer than those with CR, allowing us to test the computational efficiency and limit of the combined method; 3) Reliable simulation data on the FP times of arm retractions without CR are highly desired for examining analytical solutions of the multiple-dimensional Kramers problem [34]; 4) The extension of the method developed in the non-CR case to the CR case is fairly straightforward, as will be shown in Sec. 3.5. With an optimized selection of the reaction coordinate, which is the index of the monomer that the innermost slip-link sits on, we first validate the proposed simulation method by producing simulation results on the terminal relaxation times τ_d of mildly entangled star arms up to 8 entanglements in good agreement with those obtained from SS model simulations. The FFS simulations are then extended to longer arms with lengths up to 16 entanglements and so reach

$\tau_{\rm d}$ values about 6 decades beyond that accessible by brute force simulations (from 6×10^6 to 3×10^{12} SS unit time). The FP times of other original slip-links along the arm can be calculated using similar FFS simulations as for the innermost one, which consequently provides the entire arm relaxation spectrum $\tau(s)$. Moreover, we propose a numerical route to construct the arm end-to-end vector correlation functions, $\Phi(t)$, and stress relaxation functions, $G(t)$, from the discrete data stored at each interface during the FFS runs. Such time correlation functions are generally not discussed in other FFS studies. Our simulation results will contribute to the development of theoretical models for describing the dynamics of entangled branched polymers and also the general first-passage problems in multi-dimensional systems. The simulation methodology developed in this work should also be applicable to the study of rare events in other scientific areas.

The rest of this chapter is organized as follows. In Sec. 3.2, we introduce the single-chain slip-spring model for entangled star polymers in the absence of CR. The detailed description of the combined FFS and SS model is given in Sec. 3.3. The simulation results obtained in the non-CR systems are presented and discussed in Sec. 3.4, including the terminal relaxation times $\tau_{\rm d}$, the arm retraction spectra $\tau(s)$ and the numerical route for constructing $\Phi(t)$ and $G(t)$. In Sec. 3.5, the simulation method is extended to study the arm retraction dynamics of star polymers in the presence of CR. We draw conclusions in Sec. 3.6.

3.2 Slip-spring Model for Entangled Symmetric Star Polymers

3.2.1 Model Description

In the single-chain slip-spring model for entangled symmetric stars, each star arm is represented by a Rouse chain with $N + 1$ monomers linked by N harmonic springs

[14, 66], as shown in Fig. 1.8. One end monomer with index 0 of the chain is treated as the branch point which is fixed in space, while the other end with index N moves freely. The topological constraints on the arm are modelled by a set of virtual springs each of $N_{\mathrm{s}}^{\mathrm{SS}}$ beads. Each virtual spring has one end connected to the Rouse chain by a slip-link that can slide along the chain, and the other end, called anchor point, is fixed in space. The slip-spring model effectively assumes a binary picture of entanglements, which is qualitatively supported by recent MD simulation studies [52, 54, 111]. There is on average one slip-spring every $N_{\mathrm{e}}^{\mathrm{SS}}$ monomers. The values of $N_{\mathrm{e}}^{\mathrm{SS}}$ and $N_{\mathrm{s}}^{\mathrm{SS}}$ are adjustable for describing the intensity of entanglements. It should be noted that $N_{\mathrm{e}}^{\mathrm{SS}}$ is not necessarily equal to the entanglement length N_{e} used in tube theory. Their relation will be discussed in Sec. 3.4.2. To be consistent with previous publications [34, 66, 82], we choose $N_{\mathrm{e}}^{\mathrm{SS}} = 4$ and $N_{\mathrm{s}}^{\mathrm{SS}} = 0.5$. Other parameters, such as the bead friction coefficient ζ_0, the average bond length b of the Rouse chain, the temperature $k_{\mathrm{B}}T$ and consequently the time scale $\tau_0 = \xi_0 b^2 / k_{\mathrm{B}}T$, are all set to unity.

The Hamiltonian of the SS model is determined by the potential energies of both the harmonic bonds of the Rouse chains and the virtual springs. The trajectories of the Rouse monomers are obtained by solving their Langevin equations of motion. In the original slip-spring model [66, 81, 82], the slip-links are assumed to travel continuously along the straight lines between adjacent monomers and so can sit anywhere on the chain. In a latter version of this model [83], the slip-links move discretely by hopping from one monomer to one of its nearest neighbors with the acceptance rate controlled by a Metropolis Monte Carlo algorithm. The long-time behavior of the system is not sensitive to the details of the slip-link motion. For simplicity and computational efficiency, we employ the discrete motion approach in the current work. The slip-links are not allowed to sit on or pass through the branch points of the star arms. In the systems without constraint release, such as star polymers in a fixed polymer network, the destruction and creation of slip-links can only take

place at the free ends of the star arms. Different from the systems with CR [66], the slip-links are not coupled with each other. In addition, the slip-links on the same arm are not allowed to pass over each other or occupy the same monomer. This assumption introduces an effective excluded volume interaction between the slip-links, which is consistent with the low swapping rate between neighboring entanglements as revealed in a recent MD simulation of symmetric star polymer melts [54] .

The previous slip-spring simulations were typically carried out in an ensemble of chains and the total number of slip-links in the system is kept constant [66]. In the non-CR case, when one slip-link is deleted from a chain end, another slip-link will be added to the end of a randomly selected chain in the ensemble. For convenient installation of the FFS method, we modify the SS model for the non-CR case by simulating each entangled arm individually. The destruction of slip-links on a given arm is still incurred by the retraction of the arm free end (monomer index N), but the addition of new slip-links to the same arm end is now determined by a probability P_{add} which satisfies the detailed balance condition

$$(1 - \rho_{\text{sl}}) \left(P_{\text{add}} + \rho_{\text{sl}} P_{N-1,N} \right) = \rho_{\text{sl}} \left(P_{\text{loss}} + (1 - \rho_{\text{sl}}) P_{N,N-1} \right), \qquad (3.1)$$

where $\rho_{\text{sl}} = 1/N_{\text{e}}^{\text{SS}}$ is the average number of slip-links sitting on each monomer. $P_{i,j}$ is the transition probability for a slip-link to move from monomer i to monomer j and P_{loss} is the probability for a slip-spring sitting on the arm free end to be destructed after one time step, respectively. Eq. 3.1 thus represents the balance between the flux of slip-links to and from the end monomer. Assuming $P_{N-1,N} = P_{N,N-1}$ without loss of generality, Eq. 3.1 gives $P_{\text{add}} \approx 0.167$ for the system parameters $N_{\text{e}}^{\text{SS}} = 4$ and $P_{\text{loss}} = 0.5$. The modified SS model is validated by studying the static properties of the simulation system.
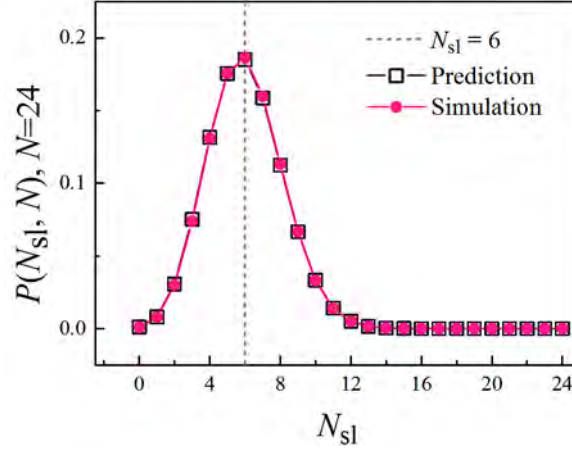
Figure 3.1: Slip-spring model simulation results (solid circles) and predictions of Eq. 3.2 (open squares) on the probability distribution of number of slip-links per arm, $P(N_{\mathrm{sl}}, N)$, for symmetric star polymers with arm length $N = 24$.

3.2.2 Static Properties

The static property of the slip-spring model system of entangled symmetric star polymers can be well characterized by the distribution of slip-links along the star arms. Considering the effective excluded volume interactions between the slip-links, the problem is similar to one-dimensional real gas in equilibrium. The probability distribution of finding N_{sl} slip-links on a star arm of N monomers is simply given by

$$P(N_{\mathrm{sl}}, N) = C_N^{N_{\mathrm{sl}}} \rho_{\mathrm{sl}}^{N_{\mathrm{sl}}} (1 - \rho_{\mathrm{sl}})^{N - N_{\mathrm{sl}}}, \tag{3.2}$$

where $C_N^{N_{\mathrm{sl}}} = \dfrac{N!}{N_{\mathrm{sl}}!(N - N_{\mathrm{sl}})!}$. Fig. 3.1 shows the good agreement between the prediction of Eq. 3.2 and the SS model simulation results on $P(N_{\mathrm{sl}}, N)$ for the system with $N = 24$. It can be seen that the peak value of N_{sl} is located at $N_{\mathrm{sl}} = 6$ in consistence with the expected average number of slip-links per arm, $\langle N_{\mathrm{sl}} \rangle = \rho_{\mathrm{sl}} N = 6$.

When there are N_{sl} slip-links on a given arm, the probability to find the i-th

slip-link on the monomer x is

$$P(x, i, N_{sl}, N) = \frac{C_{x-1}^{i-1} C_{N-x}^{N_{sl}-i}}{C_N^{N_{sl}}}, \quad (i \leq x \leq N - N_{sl} + i) \tag{3.3}$$

where the numerator is a product of the possibilities to find $i - 1$ slip-links on the arm segment from monomer 1 to $x - 1$ and to find $N_{sl} - i$ slip-links on another segment from monomer $x + 1$ to N. It should be noted that in the star polymer systems without CR the slip-links do not change their ordering along the star arms. In Eq. 3.3 the index i is considered to increase from 1 for the innermost slip-link to higher values toward the arm free end. Combining Eqs. 3.2 and 3.3, we obtain the ensemble-averaged probability to find the i-th slip-link on the monomer x:

$$P(x, i, N) = \sum_{N_{sl}=1}^{N} P(x, i, N_{sl}, N) P(N_{sl}, N). \tag{3.4}$$

Fig. 3.2 presents the SS simulation results on $P(x, i, N)$ for the slip-links with indices $i = 1$ to 6 on star arms of length $N = 24$, together with the predictions of Eq. 3.4. The good agreement between the two sets of data indicates that the simulation systems are in equilibrium state and the randomly assigned locations of the anchor points can well preserve the equilibrium distribution of the slip-links. This is also reflected by the fact that the average number of slip-links found on each individual monomer is equal to $\rho_{sl} = 0.25$, see the horizontal line in Fig. 3.2.

3.3 Combined FFS and SS Method For Entangled Star Polymers without CR

In the systems without CR, the topological constraints or entanglements imposed on a target arm are released hierarchically by the retraction of the arm free end. The terminal relaxation time τ_d of the system is defined as the average first-passage time that takes the free end of an arm to reach the branch point starting from a random initial conformation. For well-entangled star arms, τ_d grows exponentially
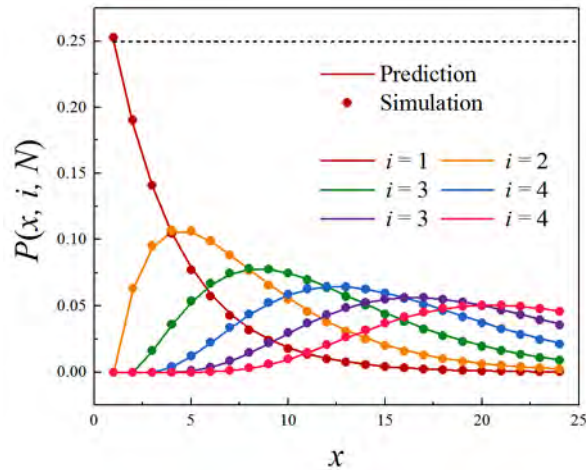
Figure 3.2: Slip-spring model simulation results (symbols) and predictions of Eq. 3.4 (lines) on the probabilities of finding i-th slip-link on monomer x, $P(x, i, N)$, for the symmetric star polymers with arm length $N = 24$. The horizontal dashed line shows the simulation results on the average number of slip-links found on each individual monomer.

with the number of entanglements per arm Z [27]. However, full arm retraction rarely happens at large Z and so is generally not accessible by standard brute force simulations. There is also no exact analytical solution of this multi-dimensional FP problem. Therefore the forward flux sampling method introduced in Ref. [68] is employed in order to study these rare events. A successful application of the FFS method on studying the FP time of 1D Rouse chain with one fixed end can be found in Ref. [34].

3.3.1 Forward Flux Sampling Method

In FFS the phase space is divided by a sequence of no-crossing interfaces denoted by λ_i $(i = 0, \ldots, m)$, as sketched in Fig. 3.3(a). The starting states of the dynamic process are on the first interface λ_0, and the reactive or terminal states are on the
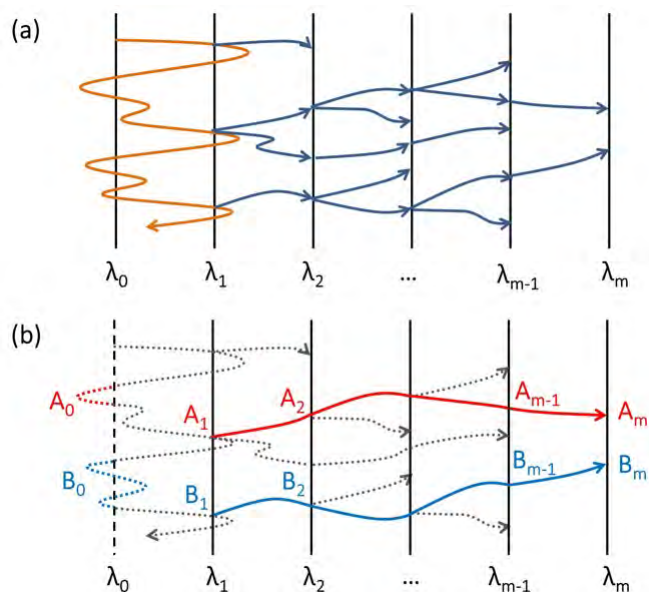
Figure 3.3: (a) Schematic diagram of the FFS method. The continuous yellow trajectory is the continuous simulation in the first stage, and the blue trajectories are the successful shooting simulations in the second stage; (b) Algorithm for building continuous arm relaxation pathways from the piecewise shooting trajectories shown in (a).

last interface λ_m. These interfaces are defined by a reaction coordinate, which can be any parameter evolving during the process, but different choices could result in significantly different performance. More detailed discussion about the reaction coordinate is given in Sec. 3.3.2.

The FFS method is operated in two stages. In the first stage, a very long continuous simulation is performed in order to calculate the frequency μ_0 at which the trajectory crosses the interfaces λ_0 and λ_1 in sequence. In the second stage, a set of consecutive shooting simulations are carried out from interface λ_i to interface λ_{i+1} for $i = 1, \ldots, m-1$, which provide the transition probabilities $P(\lambda_{i+1}|\lambda_i)$ that a system starting from λ_i will first reach λ_{i+1} rather than return to λ_0. The first-passage time τ_n for the system starting from the first interface λ_0 and ending on the

interface λ_n $(1 \ll n \leq m)$, is then given by

$$\tau_n = \frac{1}{\mu_0 \prod_{i=1}^{n-1} P(\lambda_{i+1}|\lambda_i)}, \quad 1 \ll n \leq m \tag{3.5}$$

3.3.2   Reaction Coordinate

A key issue in applying the FFS method is the choice of the reaction coordinate. Starting from a random initial configuration, the relaxation of a star arm in the system without CR proceeds by the retraction of the arm free end along the primitive path, passing through all the original slip-links on the arm sequentially until none left between it and the branch point. The terminal relaxation time is determined by the moment at which the innermost slip-link is released. During this process, the number of surviving original slip-links, N_{sl}, on the arm drops with time from its initial value to 0, making it an intuitively simple choice for the reaction coordinate. Considering that the value of N_{sl} is statistically proportional to the length of the surviving tube or primitive path, this choice would be consistent with a recent FFS study on the FP time for the free end of a 1D Rouse chain to reach a certain distance z from the fixed end where z was selected as the reactive coordinate [34]. The 1D Rouse chain study is closely related to the current work, because arm extension is essentially the reverse process of arm retraction. However, when using N_{sl} as the reaction coordinate, our FFS simulation results on the terminal arm retraction times are found to be significantly smaller than those obtained from standard SS model simulations. The problem arises from the difficulty in choosing equivalent starting states for the FFS runs. In the slip-spring model system, both the instantaneous number of slip-links and their distribution along the arm are subject to strong fluctuations, especially on the outer arm segments which undergo fast Rouse motion. In the FFS runs using N_{sl} as the reaction coordinate, the starting states are collected in the first-stage continuous simulation as the configurations where the number of slip-links on the arm is equal to the ensemble-averaged value of $\langle N_{sl} \rangle = N\rho_{sl}$. Shooting from these starting configurations, only the samples in which the values of N_{sl} decrease
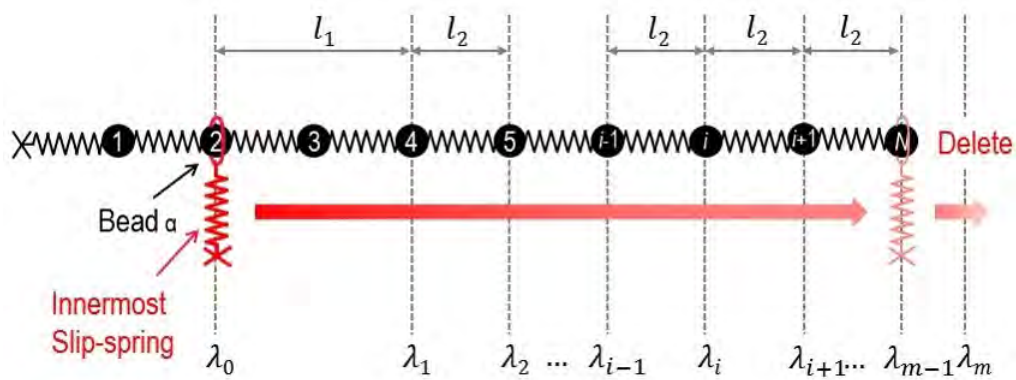
Figure 3.4: Application of FFS method for studying the retraction dynamics of an entangled star arm described by the slip-spring model. The cross (Monomer 0) on the left represents the branch point that is fixed in space. The interfaces λ_i (vertical lines) used in the FFS simulations are placed on the monomers of the arm.

monotonically are considered to reach interface λ_1 successfully. This biased strategy is thus in favor of the samples where the initial slip-link densities on the outer arm segments are higher than ρ_{sl}, because in such cases the probability to lose slip-links at short times is higher than to gain ones. Therefore a relatively large proportion of slip-links on a sample arm are released by shallow arm retractions at early times, leaving fewer than average number of slip-links on the surviving segments of the primitive path. As a consequence the terminal relaxation times obtained from the FFS simulations are shorter than those obtained from standard SS simulations where the ensemble-averaged initial distribution of slip-links is uniform. These results imply that the reaction coordinate should be selected close to the branch point in order to minimize the influence of the fast fluctuating arm end.

Since the terminal arm relaxation time is determined by the release of the innermost slip-link from the arm free end, one can track the motion of this particular slip-link along the arm by defining the index of the monomer that it sits on as the reaction coordinate. As shown in Fig. 3.4 where the 3D Rouse chain is sketched as

a straight line for convenience of discussion, the first interface λ_0 used in FFS is set on monomer α (2 in this case) where the innermost slip-link originally sits on. Any initial configuration of the confined arm in which the innermost slip-link locates on monomer α can be taken as the starting state of the FFS simulation. The second last interface λ_{m-1} is placed on the outermost monomer N of the arm, and the last interface λ_m is right outside of the arm free end, marking the final or reactive state that the arm free end has passed through the innermost slip-link and the arm is fully relaxed. The other $m-2$ interfaces are placed on the monomers in between α and N.

According to the standard FFS method, a database containing a large number of configurations is accumulated on each interface. In the first stage of the continuous simulation, the database on λ_1 is a collection of configurations whose innermost slip-link lastly crossed λ_0 before crossing λ_1. In the second stage, consecutive shooting simulations are performed from interface λ_i to λ_{i+1}, $i = 1, \ldots, m-1$ using starting configurations randomly selected from the database on λ_i. Among the M_i shooting samples, the ones whose innermost slip-links reach λ_{i+1} before going back to λ_0 are considered as successful samples and will be stored in the database of λ_{i+1}.

3.3.3 Simulation Details

Apart from the reaction coordinate, the performance of the FFS algorithm can also be affected by some other factors. One factor is that the configurations saved in the database of interface λ_1 during the first-stage continuous simulation could be strongly correlated with each other due to the limited running time at this stage in comparison with τ_{d}. This may introduce systematic errors in the simulation results if the size of the database is fixed. This problem can be resolved by increasing the interval l_1 between the interfaces λ_0 and λ_1, as shown in Fig. 3.4, and recording configurations on λ_1 at a lower frequency ω. For example, rather than recording every event that the innermost slip-link crosses λ_1 when coming from λ_0, one can

record once for every $1/\omega$ crossings. Another factor is the choices of the interface interval l_2 between λ_i and λ_{i+1} ($i = 1, \ldots, m-2$) and the number of shooting samples M_i from each λ_i which determine the performance of the FFS in the second stage. Since l_2 controls the transition probabilities $P(\lambda_{i+1}|\lambda_i)$, a smaller l_2 is normally preferred for accelerating the shooting simulations. The number M_i can then be chosen according to $P(\lambda_{i+1}|\lambda_i)$ and the desired accuracy.

In the current work we take $l_1 = 2$ and $l_2 = 1$ which separate the first two interfaces λ_0 and λ_1 by one bead and then set one interface on every bead along the arm. The recording frequency ω has to be reduced for longer arms in order to reduce the conformational correlations on λ_1 and is empirically taken to be $\omega = 1/(N-15)$ for arm length $N \geq 16$. Since the reaction coordinate is defined by the location of the innermost original slip-link, the transition probability $P(\lambda_{i+1}|\lambda_i)$ increases with i towards the arm free end. In order to achieve good statistics for the first few interfaces close to the branch point, M_i should be large enough. A number of samples $M_i = 40,000$ is thus used for λ_i, $i = 1, 2, \ldots, m-1$ in all of the FFS simulation runs. As shown in Fig. 3.2, there is a non-negligible fraction of initial configurations where the innermost slip-links are many monomers away from the branch point and could be released by shallow arm retractions. The terminal relaxation times of such arms are thus much shorter than those of the arms with uniform slip-link distributions. Actually their terminal times have been reached in the first-stage continuous simulations without going into the second stage of FFS. These τ_d data are still counted for calculating the distribution and the mean value of the terminal relaxation times.
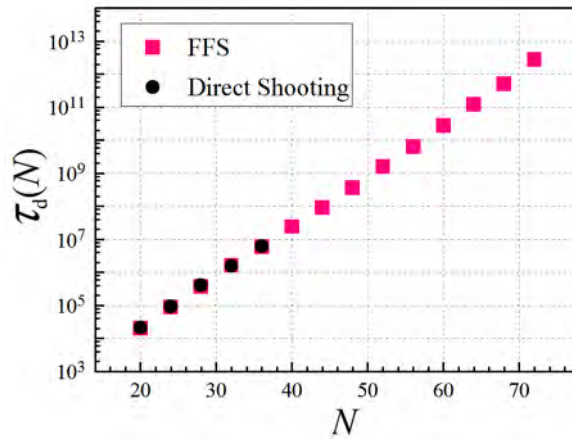
Figure 3.5: Simulation results on the terminal arm retraction time τ_{d} obtained from FFS and direct shooting simulations as a function of arm length N.

3.4 Results and Discussions for Systems Without Constraint Release

3.4.1 Terminal Time of Arm Retraction

The terminal time τ_{d} of the arm retraction process is the main and most straightforward output of the FFS simulations. Fig. 3.5 presents the FFS results on τ_{d} as a function of the arm length N. For comparison, we have also included the τ_{d} data obtained from the so-called direct shooting simulations which start from the first interface λ_0 and stop at the last interface λ_m without intermediate steps. These runs are equivalent to the slip-spring simulations using initial configurations randomly picked from the database on interface λ_0 and running continuously until the innermost original slip-spring being deleted by the arm free end. For each arm length, the direct shooting simulation results are averaged over $10,000$ independent samples, while in the FFS simulations τ_{d} is averaged over $2,000$ independent runs. Since in each FFS run there are $40,000$ samples recorded on λ_1, the average is actually taken over a much bigger ensemble than that of the direct shooting runs. Considering the
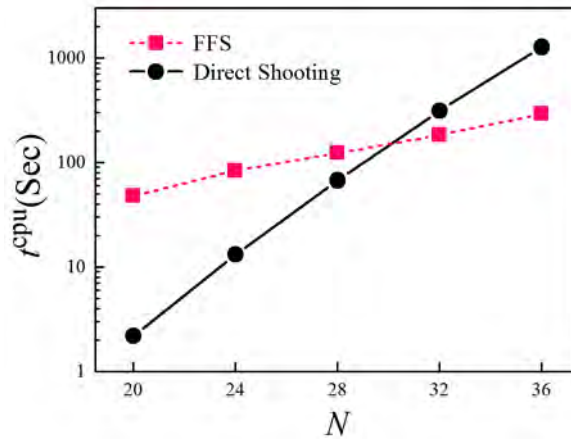
Figure 3.6: Average computational times required for completing a single FFS and a single direct shooting run on a single Intel Xeon processor.

---

high computational cost, the direct shooting simulations are only performed for arm lengths from $N = 20$ to 36, corresponding to about 4 to 8 entanglements per arm estimated with $N_e \approx 4.47$ as discussed in Sec. 3.4.2. In this range of N, the FFS and direct shoot simulation results in Fig. 3.5 show very good agreement with the relative differences less than 5%. The combined FFS and SS method and the choice of the reaction coordinate are thus well justified.

Fig. 3.6 compares the average computational times required to complete a single direct shooting and a single FFS run on a single CPU (Intel Xeon E5-2620). The direct shooting simulation is faster at short arm lengths, but its computational time grows exponentially with N and overtakes that of the FFS when $N \geq 32$. The FFS method allows us to study much longer arms. For entangled star polymers with arm length $N = 72$ in the absence of CR, the terminal relaxation time is found to be $\tau_d \approx 2.85 \times 10^{12}$ which is about 8 orders of magnitude longer than that of stars with $N = 20$ and is basically inaccessible to any type of direct simulations.

3.4.2 Comparison with Theoretical Model Predictions

The τ_d data in Fig. 3.5 show a clear exponential dependence on the arm length N, which is expected from the Pearson-Helfand theory for star arms retracting in a fixed network [27]. These results can be further compared with the predictions of more detailed theoretical models [30, 34, 37]. The Milner-McLeish theory based on the solution of 1D Kramers problem predicts the terminal arm retraction time in the absence of CR as [30, 37]

$$\tau_d(N) = \frac{\pi^{5/2}}{4\sqrt{6}} \tau_R(N) \frac{1}{z} \exp\left(\frac{3z^2}{2}\right), \tag{3.6}$$

where $z = \sqrt{N/N_e}$ and the arm Rouse time $\tau_R(N) = 4\zeta_0 N^2 b^2/3\pi^2 k_B T$. The entanglement molecular weight N_e can be estimated by substituting the corresponding FFS result on $\tau_d(N)$ into Eq. 3.6. As shown in Fig. 3.7, the obtained N_e values are roughly independent of N, giving $N_e \approx 4.98$.

Recently Cao et al. pointed out that the first-passage problem of Rouse chain should be treated as a multi-dimensional Kramers problem [34]. FFS simulations of 1D Rouse chains showed that the z^{-1} scaling in the prefactor of τ_d as predicted in Eq. 3.6 is only valid for very large chain extensions. In the intermediate chain extension regime corresponding to realistic arm retraction process, a new theory based on the Freidlin-Wentzell theory was proposed [112], which predicts a z^{-3} scaling in the prefactor of the terminal time [Eq. 60 in Ref. [34]]

$$\tau_d(N) = \frac{C(N)\tau_R(N)}{z^3} \exp\left(\frac{3z^2}{2}\right), \tag{3.7}$$

where $C(N)$ is a fitting parameter. For arm lengths $N \geq 20$ we can take the plateau value of $C(N) = 1.2$ as found in the FFS simulations of 1D Rouse chains [34]. The N_e values calculated by substituting the FFS data on $\tau_d(N)$ into Eq. 3.7 are shown in Fig. 3.7, which increase with the increasing arm-length and approach an asymptotic value of $N_e \approx 4.47$ that is smaller than the N_e value estimated by using Eq. 3.6. The two theoretical models thus predict qualitatively different dependence of N_e on
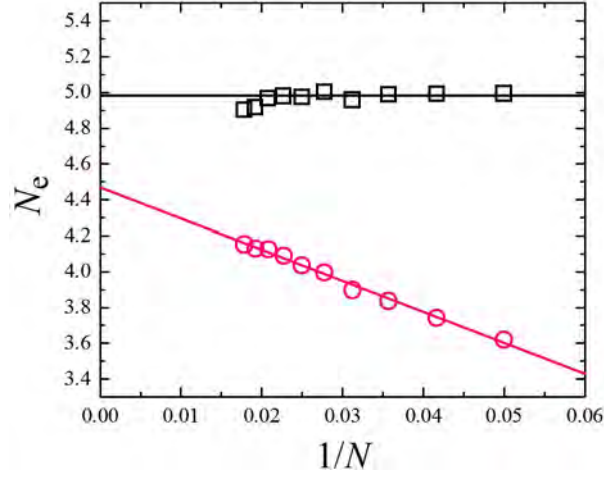
Figure 3.7: Entanglement molecular weight N_e calculated by substituting the FFS simulation results on τ_d (Fig. 3.5) into the theoretical predictions of Eqs. 3.6 (squares) and 3.7 (circles) for various arm lengths.

N, at least in the systems without CR. Since the entanglement molecular weight is one of the most important model input parameters for predicting the dynamics and rheology of entangled polymers, this N-dependent behavior apparently needs further investigation for developing quantitative theories. The FFS results on τ_d over a broad range of arm lengths should work as a benchmark for examining theoretical models that are typically developed for well entangled polymers.

We note that the N_e values given in Fig. 3.7 are different from that obtained by mapping the slip-spring model simulation results on the linear viscoelastic properties of linear polymer melts to the tube model predictions ($N_e \approx 5.7$) [66, 82]. The difference could be related to the use of different theoretical models for the data fitting and also the presence of constraint release effects in the polymer melts.

3.4.3 Arm Relaxation Spectrum

Apart from terminal relaxation time, the FFS method can also be applied to obtain the entire relaxation spectrum of the arm. This is done in a similar way as calculating τ_d. The only difference is to set the index of the monomer that the i-th original slip-link sits on, instead of that of the innermost slip-link, as the reaction coordinate. Accordingly the first interface λ_0 in the FFS method is defined on the monomer where the i-th slip-link originally occupied. The FP time of the i-th slip-link is recorded as $\tau(X)$ with the fractional index $X = i/\langle N_{sl} \rangle$. The simulation results on $\tau(X)$ are plotted in Fig. 3.8 for the arm lengths $20 \leq N \leq 44$. For the systems with $N \leq 36$, the direct shooting simulation results are also presented for comparison. The agreement between the FFS and direct shooting data gets improved as the arm free end retracts deeper along the primitive path, i. e., with the decrease of the slip-link index i and so X. This is understandable because the release of the outer slip-links or entanglements is dominated by the fast Rouse-like fluctuations. The corresponding energy barrier is relatively low such that the FFS method does not work well at large X. For this reason, the most reliable relaxation spectrum, especially for the long arms, should be constructed by combining the FP times of the inner slip-links as calculated by the FFS method with the FP times of the outer ones obtained from direct shooting simulations. One such example is shown in Fig. 3.8 for the systems with $N = 44$. The complete relaxation spectrum $\tau(X)$ can be directly applied to test theoretical models on arm retraction dynamics.

3.4.4 Constructing Relaxation Correlation Functions

In experiments the dynamics and rheology of entangled polymers are generally characterized by the dielectric relaxation or chain end-to-end vector correlation function, $\Phi(t)$, and the stress relaxation function, $G(t)$. The calculation of these observables usually requires the continuous trajectories of the polymers, which are however not naturally available in FFS simulations, because only instantaneous configurations
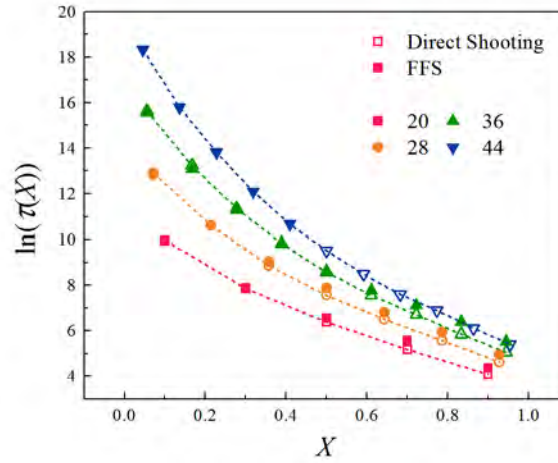
Figure 3.8: Relaxation spectrum calculated using the first-passage times of all slip-links for star arms with various lengths obtained by both FFS (solid symbols) and direct shooting (open symbols) simulations. The dashed curves are for guiding the eye. The parameter $X = i/\langle N_{\text{sl}} \rangle$ is the fractional index of the i-th slip-link along the arm, which increases from $X = 1/\langle N_{\text{sl}} \rangle$ for the innermost slip-link to 1 for the outermost one.

at the hitting points on the interfaces are recorded. Here we introduce a numerical route to effectively link these discrete pieces of information to construct the dielectric and stress relaxation functions. The systems of entangled star polymers without CR are used as examples to demonstrate the application of this algorithm.

Fig. 3.3(b) sketches the method used to build continuous arm relaxation pathways from the piecewise FFS shooting trajectories shown in Fig. 3.3(a). Considering two hitting points on the terminal interface λ_m, marked as A_m and B_m, there must be two continuous trajectories or pathways that one can track back from them to the first interface λ_0. As shown in Fig. 3.3(b), the pathway to state A_m is constructed by linking the successful shooting trajectory from the hitting point A_{m-1} to A_m with that from A_{m-2} to A_{m-1}, and so on until reaching the point A_1 on the interface λ_1. The linking from A_1 to a start point A_0 is obtained from the trajectory generated

in the continuous simulation in the first stage of the FFS simulations. Similarly the pathway to the hitting point B_m can be traced back to B_1 on λ_1 and then to a starting point B_0. We note that these rebuilt trajectories are different from the true continuous trajectories generated in standard slip-spring model simulations, but the ensemble-averaged pathways obtained in these two cases should be very close, as reflected in the consistent $\Phi(t)$ results in Fig. 3.10. From computational point view, the rebuilding method requires the storage of all the successful shooting trajectories between neighboring interfaces and also large memory for data processing. This may limit its application to large systems such as the fine-grained bead-spring models widely used in molecular dynamics simulations.

When calculating the arm relaxation correlation functions from the rebuilt trajectories, two assumptions have been made. First, when one slip-link is destroyed by the retracting arm free end, the primitive path segment in between its nearest neighboring slip-link and itself will be forgotten immediately. This assumption is valid for most of the slip-links due to the discrete feature of entanglements in the SS model. The only exception is with the tube segment between the branch point and the innermost slip-link where this assumption may affect the calculation of the relaxation functions in the terminal regime, as discussed below. The second assumption is that the FP times on each interface follow a single exponential distribution. This assumption has also used in solving the 1D Kramers problem and in the Doi-Edwards tube model without CR [17]. Since the slip-spring model is essentially a multidimensional problem, we perform an extra set of simulations to examine the validity of this assumption. A total number of $10,000$ direct shooting simulations, all starting from exactly the same initial configuration, are carried out to mimic a FFS run. The FP times for the innermost slip-link to reach different monomers, or different interfaces in the FFS definition, are recorded. Fig. 3.9 presents the probability distributions, $P_i(t)$, of the FP times on three different interfaces for the arms of length $N = 20$. It can be seen that $P_i(t)$ on interfaces with higher indexes
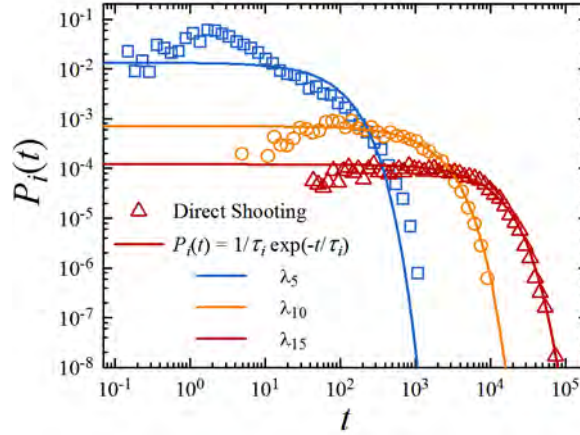
Figure 3.9: Probability distributions of the first-passage times for the innermost slip-link to reach different monomers or different interfaces in the FFS definition λ_i along the arm as calculated by direct shooting slip-spring simulations of star arms of length $N = 20$. All of the $10,000$ simulations start from the same initial configuration where the innermost slip-link sits on monomer 1 next to the branch point. The solid lines represent single exponential fit to the simulation data in each case.

---

can be well described by the exponential function

$$P_i(t) = \frac{1}{\tau_i} \exp\left(-\frac{t}{\tau_i}\right) \tag{3.8}$$

where τ_i is the mean FP time on the interface λ_i. The second assumption becomes valid as the arm free end retracts deeply along the primitive path.

Following Eq. 3.8 the probability that the innermost slip-link has never crossed the interface λ_i after time t is

$$P_{\lambda_i}^0(t) = \exp\left(-\frac{t}{\tau_i}\right), \tag{3.9}$$

and the probability that it has crossed λ_i at least once is

$$P_{\lambda_i}^\infty(t) = 1 - \exp\left(-\frac{t}{\tau_i}\right). \tag{3.10}$$

Therefore the probability that the trajectory starting from λ_0 has crossed interface λ_i but never crossed interface λ_{i+1} is

$$P_{\lambda_i}^{\lambda_{i+1}}(t) = P_{\lambda_i}^{\infty}(t) - P_{\lambda_{i+1}}^{\infty}(t) = -\exp\left(-\frac{t}{\tau_i}\right) + \exp\left(-\frac{t}{\tau_{i+1}}\right). \qquad (3.11)$$

The time correlation function of a dynamic observable, V, whose instantaneous values are calculated on different interfaces can be evaluated by

$$\langle V(t)V(0)\rangle = \left\langle P_{\lambda_0}^{\lambda_1}(t)W_0 + \sum_{i=1}^{m-1} P_{\lambda_i}^{\lambda_{i+1}}(t)W_i + P_{\lambda_m}^{\infty}(t)W_m \right\rangle \qquad (3.12)$$

where W_i is defined as

$$W_i = \frac{1}{h_i} \sum_{k=1}^{h_i} V_i^k V_0^k, \qquad (3.13)$$

and h_i is the number of hitting points on the interface λ_i out of the M_{i-1} shootings from λ_{i-1}, V_i^k is the observable value at the k-th hitting point on λ_i and V_0^k is its value at the corresponding starting point of the trajectory on the first interface λ_0. For the system sketched in Fig. 3.3(b), there are only 2 hitting points on the final interface λ_m such that $h_m = 2$ in Eq. 3.13.

Substituting Eqs. 3.10 and 3.11 into Eq. 3.12, we get

$$\langle V(t)V(0)\rangle = \left\langle \sum_{i=0}^{m-1} \Delta W_{i,i+1} \exp\left(-\frac{t}{\tau_{i+1}}\right) + W_m \right\rangle, \qquad (3.14)$$

where $\Delta W_{i,i+1} = W_i - W_{i+1}$. The correlation function in Eq. 3.14 is expressed as a weighted summation of a set of exponential functions, which is consistent with the tube model predictions for the end-to-end vector and stress relaxation functions of entangled polymers in the absence of constraint release [17]. The only difference lies in the last term W_m on the right hand side of Eq. 3.14 which, if being nonzero, may result in an unphysical plateau after the terminal relaxation time τ_d.

The problem associated with W_m does not exist in the tube model where the tube is assumed to be continuous. The arm free end can thus retract continuously along the primitive path all the way to the branch point and so release all the memories

in the original tube. As a result, W_m decays to zero for all dynamic observables. However, in the slip-spring model, the entanglements are represented discretely by the slip-links. The terminal time τ_d is taken to be the time when the arm free end passes the innermost slip-link. It implies that the memories, such as stress and end-to-end vector orientation, stored in the original tube segment between this slip-link and the branch point are not fully forgotten right after τ_d, giving to a nonzero ensemble average value of W_m. Actually this is an intrinsic problem for all models using discrete description of entanglements. We will address this problem in more details in a future work. For the current work, we will neglect the last term in Eq. 3.14 by setting $W_m = 0$, which is reasonable at least for the systems with very long arms where the contribution from the last tube segment is relatively small. This approximation is analogous to the so-called disentanglement relaxation mechanism used in the tube-based computational models where a polymer branch is considered to be fully relaxed by disentanglement when there is only one or few entanglements left on the branch [39, 44].

The dielectric and stress relaxation functions calculated using Eq. 3.14 with $W_m = 0$ from the rebuilt trajectories are plotted in Fig. 3.10 for arm lengths up to $N = 72$. For comparison, the $\Phi(t)$ and $G(t)$ results obtained from standard slip-spring model simulations are also included for the systems with $N \leq 36$. The two sets of $\Phi(t)$ curves show very good agreement in the terminal regime, indicating the capability of Eq. 3.14 in constructing the arm relaxation functions using discrete FFS shooting trajectories. The discrepancy at short time scales can be attributed to the numerical problem that the constructed $\Phi(t)$ curves start from initial values smaller than 1. Since the W_m term in Eq. 3.14 is neglected when calculating $\Phi(t) = \langle \boldsymbol{R}_e(t) \cdot \boldsymbol{R}_e(0) \rangle$ where $\boldsymbol{R}_e$ is the arm end-to-end vector, the resulted value of $\langle \boldsymbol{R}_e^2(0) \rangle$ at the initial time is smaller than the true mean squared end-to-end distance of the arms which is obtained from standard slip-spring model simulations and used for normalizing $\Phi(t)$. The so-obtained initial values of the $\Phi(t)$ curves
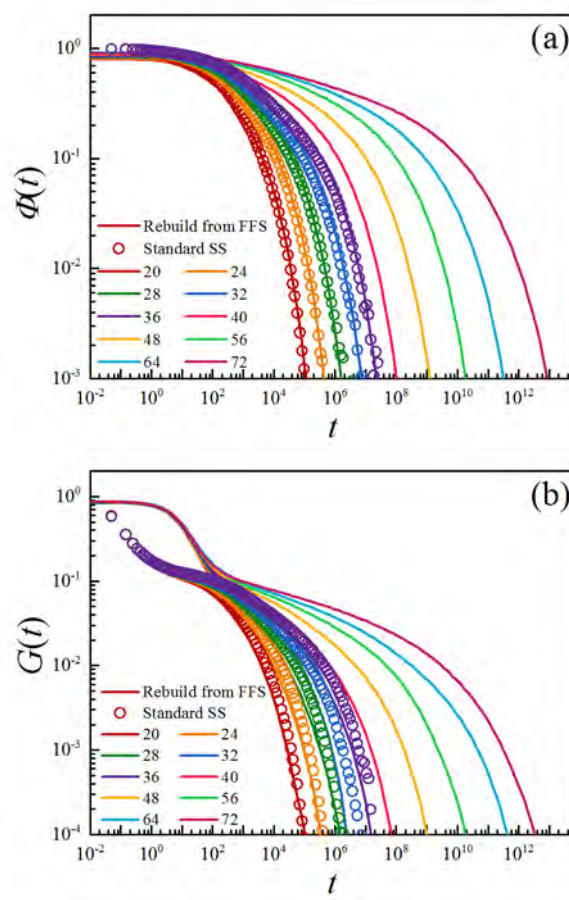
Figure 3.10: (a) Arm end-to-end vector correlation function $\Phi(t)$ and (b) stress relaxation function $G(t)$ obtained from standard slip-spring simulations (symbols) and calculated using Eq. 3.14 from the rebuilt trajectories (lines), respectively.

are $\Phi(t = 0) = 0.80$ for arm length $N = 20$ and 0.92 for $N = 72$, respectively. As expected, the contribution of W_m becomes less significant with increasing arm length.

The $G(t)$ results presented in Fig. 3.10(b) are the single-arm stress autocorrelation functions without considering the cross correlation contributions from the virtual springs [113, 114]. This choice does not affect any discussions or conclusions in the current work, especially when there is no constraint release effect. Different

from the $\Phi(t)$ results, the $G(t)$ curves calculated using the rebuilt trajectories decay faster than those from the slip-spring simulations, which implies the existence of systematic errors originated from different resources. First of all, the assumption that the FP times follow an exponential distribution does not apply for the first few interfaces due to the relatively low energy barrier, as shown in Fig. 3.9. Therefore the constructed $G(t)$ curves show significant difference from the standard slip-spring simulation results at early times. Secondly, the calculation of the stress relaxation function requires a very large ensemble average for achieving good statistics. In the molecular dynamics and slip-spring model simulations, the instantaneous stress tensor usually needs to be calculated at every single time step [115]. But in FFS simulations the number of data points on each interface is rather limited. Thirdly, Eq. 3.14 calculates the relaxation correlation functions using the information, such as the arm conformations and the locations of the slip-links, carried by the hitting points on each interface. These hitting points are only saved from the successful shooting trajectories which are in favor of the arm retraction process and correspondingly the redistribution of the Rouse beads in between the slip-links. The biased change of the local conformations of polymer segments leads to faster relaxation of the stress, because $G(t)$ depends on the local bond or segment reorientation. The end-to-end vector correlation function is less sensitive to this problem, because $\Phi(t)$ is determined by the relaxation of the vectors linking neighboring slip-links.

3.5 Extension of the combined FFS and SS method to Systems with Constraint Release

The combined FFS and SS method can be extended to entangled polymer systems with CR by adjusting the definition of the reaction coordinate. In the standard slip-spring model [54, 66], constraint release is included by coupling the slip-links sitting on different polymer chains or arms into pairs to represent the binary entanglements.

When one slip-link is deleted from the free end of an arm, its coupled partner is also deleted regardless of its location, which results in a CR event. This means that for FFS simulations the originally innermost slip-link could not be used to define a reaction coordinate alone for exploring the entire arm relaxation spectrum, because this slip-link may be destructed by a CR event before reaching the arm free end. To resolve this problem, we refer to a recent slip-spring simulation work on entangled symmetric star polymers with CR [54]. There it was shown that the relaxation of the original tube segments, and correspondingly the relaxation of the arm end-to-end vector, is dominated by the first-passage times of the so-called tube-representative (TR) slip-links, which are the original slip-links finally released from the arm free end. The other original slip-links which are destructed from the middle of the arm by CR events only contribute to stress relaxation. For determining the terminal relaxation time of the arm end-to-end vector, we only need to find the moment when the last tube segment held in between the branch point and the innermost TR slip-link is released by the arm free end. Since it is not known in advance whether an original slip-link will be deleted by the arm end or by CR, we can define the reaction coordinate as the index of the monomer which the innermost *surviving* original slip-link sits on. In other words, if at time t the innermost original slip-link was deleted by CR, the reaction coordinate will be immediately shifted from the monomer it sat on to the monomer occupied by the nearest original slip-link, because the latter becomes the innermost surviving original slip-link. This procedure will continue until the last surviving original slip-link is destructed by the arm free end and so the terminal relaxation time τ_d is reached.

The ensemble-averaged terminal relaxation times, τ_d, obtained in the FFS simulations with the modified definition of the reaction coordinate are presented in Fig. 3.11, together with the terminal relaxation times of the arm end-to-end vector relaxation functions as obtained from standard slip-spring model simulations and the mean FP times of the innermost surviving original slip-links as obtained from
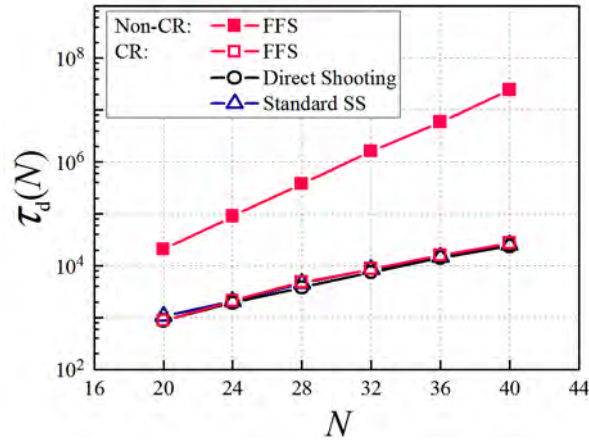
Figure 3.11: Simulation results on the terminal arm relaxation times τ_d obtained from the FFS (open squares) and direct shooting (open circles) simulations, together with the terminal times of the arm end-to-end vector correction functions calculated from standard slip-spring simulations (open triangles), in the systems with constraint release. For reference, the FFS results on τ_d for the systems without CR (solid squares, same as in Fig. 3.5) are also plotted.

the direct shooting simulations. The three sets of data show very good agreement within error bars, which effectively validates the proposed FFS method. The combined FFS and SS method can thus provide quantitative predictions on the terminal relaxation times of entangled star polymers either with or without CR over a broad range of arm lengths that are surely needed for the development of quantitative theories for entangled branched polymers. The construction of the relaxation correlation functions, $\Phi(t)$ and $G(t)$, in the CR cases is rather complicated and will be left for further study.

3.6 Conclusions

We present an application of the forward flux sampling method in combination with the slip-spring model on studying the arm retraction dynamics of entangled star polymers. The single-chain slip-spring model originally developed for describing entangled linear polymers has been extended to model symmetric star polymers. As a proof of concept, we start with the systems without constraint release where the entanglements or slip-links can only be created on or deleted from the arm free ends, making the FFS method conveniently applicable. Two possible reaction coordinates for the FFS simulations have been tested. The choice of the index of the monomer that the originally innermost slip-link sits on is found to provide FFS simulation results on terminal relaxation times τ_d in good agreement with those obtained in direct shooting simulations for mildly entangled stars with arm lengths up to 8 entanglements. The FFS simulations are then performed to study the terminal relaxation of much longer arms (up to 16 entanglements) that are not accessible by any direct simulations, especially considering the exponential growth of τ_d with the arm length in the absence of CR. The FFS results on τ_d over such a broad range of arm lengths allow direct comparison with the predictions of theoretical models which are typically developed for well entangled polymers. The entanglement molecular weight N_e extracted from such comparison is found to have an arm-length dependence.

In addition to the terminal arm relaxation time, the first-passage times of all other original slip-links on a given arm can also be conveniently calculated by defining the reaction coordinate as the index of the monomer that the interested slip-link sits on, which in turn provides the entire relaxation spectrum of the arm. For mildly entangled arms the FFS results on the FP times show good agreement with direct shooting simulation data for the deep entanglements or inner slip-links, but some discrepancy exists for the shallow ones, because the FFS method does not work well at low energy barriers. The reliable relaxation spectrum of long star arms

thus should be constructed by combining the FP times of the inner slip-links as calculated by the FFS method with the FP times of the outer ones obtained from direct simulations. Furthermore we have proposed a numerical route to construct the arm relaxation correlation functions from the FFS simulation data saved on discrete interfaces. This method is essentially a summation of weighted exponential relaxation functions with characteristic times determined by the mean FP times of different slip-links along the arm. The so-constructed arm end-to-end vector correlation functions, $\Phi(t)$, show reasonably good agreement with those obtained in standard slip-spring simulations, while larger quantitative discrepancies are found for the stress relaxation functions $G(t)$ probably due to the biased selection of local segment conformations during the FFS simulations.

We have also attempted to extend the FFS method to systems with constraint release, namely to entangled star polymer melts. The key change from the non-CR case is to define the reaction coordinate using the innermost surviving original slip-link. Again good agreement is found between the FFS simulation results on the terminal arm relaxation time with those obtained in standard slip-spring model simulations. Therefore the combined FFS and slip-spring simulation method provides an efficient tool for studying the dynamics of highly entangled branched polymers which are generally inaccessible to direct simulation methods but highly desired for the development of quantitative theories on entangled branched polymers.

Chapter 4

Relaxation of Branched Polymers: A Combinational Study by Molecular Dynamics and Slip-Spring Model

4.1 Overview

To describe the rheological behaviour of branched polymers and their general mixtures, the tube theory has to incorporate different relaxation mechanisms, such as contour length fluctuation or arm-retraction [27], and constraint release which is modelled by either dynamic tube dilation [28, 30] or constraint release Rouse motion [22]. A number of approximations and assumptions have to be made for describing various experimental results. For example, for describing 3-arm asymmetric stars, it was assumed that the full retraction of the short arm allows the branch point to hop a fraction of the tube diameter, pa, where p is a factor smaller than 1 and a is either the original or dilated tube diameter under different assumptions. In order to fit the experimental data, the fitting parameter p^2 ranges from 1 to 1/60 for different asymmetric stars. For H-polymers, however, the range of p^2 is relatively narrow, roughly from 1/12 to 1/15 [36]. Recently Bačová et al. [116] performed large-scale

molecular dynamics simulations of entangled branched polymers and found that considering hopping in the dilated tube provides the most consistent set of hopping parameters in different architectures. However, whether the value of p^2 should be universal or system-dependent remains unknown, which implies that both the theoretical model and the underlying assumptions should be examined starting from microscopic principle.

On the other hand, different theoretical or numerical models at more fine-grained levels have been developed for describing entangled polymers. Representative examples are the slip-link based models [59–67]. This class of models treats the entanglements as binary contacts between different chain segments, and thus can introduce finer details, such as the conformation of polymers in space, the specified locations of entanglements, and the spectrum of constraint release rates. Among these models, the slip-spring model developed by Likhtman [66] has been shown to describe the MD simulations and experimental results on linear systems reasonably well [81]. Most recently, the slip-spring model has been extended to study symmetric stars and star-linear blends by comparing the stress relaxation modulus $G(t)$ with the experimental data [101]. Cao and Wang [54] have also used slip-spring model and the MD simulations based on Kremer-Grest (KG) model to investigate the arm-retraction and constraint release effects on star polymers, and examined the mechanism proposed by Shanbhag et al. [62] on explaining the release of the deepest entanglements on the star arms.

In this chapter, we investigate the application of the slip-spring model on branched polymers of different architectures, starting from testing the consistency of its prediction power, such as the universality of model parameters for both linear chains and branched polymers. The model systems we studied include 3-arm symmetric stars, asymmetric-stars, and H-polymers. For the later two architectures, current slip-spring model might fail because some mechanisms are missing, e.g., the slip-springs on the cross-bars of H-polymers cannot be released by arm retraction. In

order to find the additional mechanisms, microscopic understanding from molecular dynamics simulations is required.

This chapter is arranged as follows. In Sec. 4.2, we will introduce the advanced techniques for performing highly efficient MD simulations and data analysis of mildly entangled branched polymers represented by the fully flexible Kremer-Grest bead-spring model. The slip-spring model has two versions which are different on the way to handle slip-link motion. In the original version, the slip-links diffuse continuously along the chain backbone, following the standard Brownian dynamics (BD) [66]. In a recently updated version (see Sec. 1.6.2), the slip-links move discretely by hopping between neighbouring monomers as governed by a Monte-Carlo algorithm in order to achieve higher efficiency [83]. The optimization of the model parameters, including the frequency to perform MC algorithm f^{SS}, the coarse-graining parameter N_0, and the time-scale mapping factor t_0, and the test of their consistency between linear and branched polymers are given in Sec. 4.3. In Sec. 4.4, we present the MD simulation results for symmetric stars, asymmetric stars, and H-polymers, whose observables, such as the end-to-end vector relaxation function $\Phi(t)$ and the monomer mean-square-displacement $g_1(t)$ are compared with the predictions of the tube-based theory. Following that, we compare the simulation results obtained by running the standard slip-spring simulations with the MD data on the same systems and show the significant discrepancy between them, especially for asymmetric stars and H-polymers. Such discrepancy can be attributed to the missing mechanism mentioned before. To cope with it, a parameter-free algorithm allowing the slip-links to cross the branch-point will be added into the slip-spring model, whereby a remarkable improvement can be achieved on the agreement with MD results. The conclusions will be given in the last section.

4.2 MD Simulation Method

The KG bead-spring model (see Sec. 1.6.1) is the most widely used generic MD model for entangled polymers, in which the beads representing the monomeric units interact with each other via the purely repulsive Lennard-Jones (L-J) potential. Combined with the bonding potential modelled by FENE, the excluded volume interactions can effectively prevent the chains from crossing. Chain stiffness can be introduced into the KG model via a three-bead bending potential, whereby more entanglements can be implemented with same chain length. For distinction, the chain model with and without bending potential are, respectively, called fully flexible and semi-flexible KG models. The semi-flexible KG model is relatively cheaper on the computational cost, but the simulation results obtained using fully flexible KG chain model have been shown to have better agreement with experimental data; thus the fully flexible KG model is still the first choice as long as the computational cost is affordable [82, 115].

MD simulations of the entangled star polymers are extremely expensive, because the terminal relaxation time τ_d grows exponentially with the number of entanglements per arm. In order to use the fully flexible KG model, we employed a high-performance GPU package called **HOOMD** [117, 118], which allows us to reach the terminal relaxation time of the symmetric stars with arm-length up to $M = 384$ (for convenience we use M to represent the number of monomers in KG model and use N to represent the number of beads in slip-spring model in this chapter). Considering the average entanglement segment length is about 50 to 65 [51, 82], the corresponding number of entanglements per arm is around 6 to 7. The simulations are performed in the NVT ensemble with a periodic boundary conditions applied to all three dimensions. The volume of the central cubic box is obtained by $V = M_{\text{tot}}/\rho$, where M_{tot} is the total number of beads and $\rho = 0.85\sigma^{-3}$ is the density

of the beads. The equation of motion of beads is given by

$$m\ddot{\mathbf{r}}_i = -\nabla U(\mathbf{r}_i) - \Gamma\dot{\mathbf{r}}_i + \mathbf{W}_i(t).$$

where $\mathbf{r}_i$ is the coordinate of the i-th bead, m is the mass of beads, $\Gamma = 0.5(mk_{\mathrm{B}}T)^{1/2}/\sigma$ is the friction coefficient, $\mathbf{W}$ is the Gaussian white noise satisfying $\langle\mathbf{W}_i(t)\cdot\mathbf{W}_j(t')\rangle = \delta_{ij}\delta(t-t')6k_{\mathrm{B}}T\Gamma\mathbf{I}$, and $\mathbf{I}$ denotes the three-dimensional unit matrix. The simulation time-step is $\Delta t = 0.012\tau_{\mathrm{LJ}}$, while τ_{LJ} is the Lennard-Jones time.

The equilibration of the initial system is carried out by a home-made code called **generic polymer simulator (GPS)**. In order to achieve a faster equilibration, a soft potential [102] is employed to perform the relaxation. The potential functions for bonded and non-bonded interactions are formulated by

$$U_{\mathrm{b}}(r) = \frac{k_{\mathrm{s}}}{2}(r - r_0)^2; \quad U_{\mathrm{nb}}(r) = \begin{cases} -\dfrac{3u_0}{4}\left(r^2 - r_{\mathrm{c}}^2\right) & r \leq r_{\mathrm{c}} \\ 0 & r > r_{\mathrm{c}} \end{cases} \tag{4.1}$$

where $k_{\mathrm{r}} = 20\epsilon$, $r_0 = 1.222\sigma$, $r_{\mathrm{c}} = 1.6\sigma$, and $u_0 = 2.2\epsilon$. The soft potential allows the chains to cross each other, but can preserve the static properties, such as the chain conformations, close to the KG model.

The dynamic observables are obtained using the data analysis tools in the GPS code, which can efficiently calculate the time correlation functions on-the-fly via an algorithm called "**correlator**" [119]. During simulations, GPS can work as an external module of HOOMD. Specifically, HOOMD generates the trajectory coordinates of the beads, which are read and analyzed by GPS at high frequency; then, GPS update the data of measured observables, and stores the trajectory files at a low frequency for further analysis.

4.3 Calibration of the Slip-Spring Model Parameters

4.3.1 Basic Parameters

In Sec. 1.6.2, we have introduced the slip-spring model that takes Monte-Carlo algorithm to govern the diffusion of slip-links. Slip-spring model requires three basic parameters: the average number of beads between neighbouring slip-links N_e^{SS}, the number of the beads on the virtual spring N_s^{SS}, and the frequency to perform the MC moves f^{SS}. In Ref. [66], Likhtman compared a variety of the combinations of N_e^{SS} and N_s^{SS} in the slip-spring model of the Brownian dynamics version, showing that their combinations determine the plateau modulus G_e in stress relaxation. Thus the plateau regimes can be superimposed on each other by adjusting them in pair. In a standard setting, N_e^{SS} and N_s^{SS} are 4 and 0.5 respectively. Once N_e^{SS} and N_s^{SS} are decided, the entanglement segment length is determined, thus the coarse-graining level is also determined. Other pairs of N_e^{SS} and N_s^{SS} could be employed to change the level of coarse-graining. For example, $N_e^{SS} = 8$ and $N_s^{SS} = 1$ will reduce the level of coarse-graining by half, thus one must double the number of beads to preserve the number of entanglements. The finer slip-spring model shows finer resolution in early regimes with additional computational cost.

The frequency of MC attempts per time-step f^{SS} is related to the friction coefficient of the slip-links in the original BD version. ξ_s is supposed to have little effect on rheological properties when it is much smaller than the friction coefficient of beads ξ_0. In the standard setting of the BD version, ξ_s is set to be $0.1\xi_0$ since technically it cannot be 0. Similarly, f^{SS} in the MC version must be large enough to ensure that the slip-link can efficiently find out the local minimum potential within each time-step. In order to find the optimal value of f^{SS}, we compared the viscosity
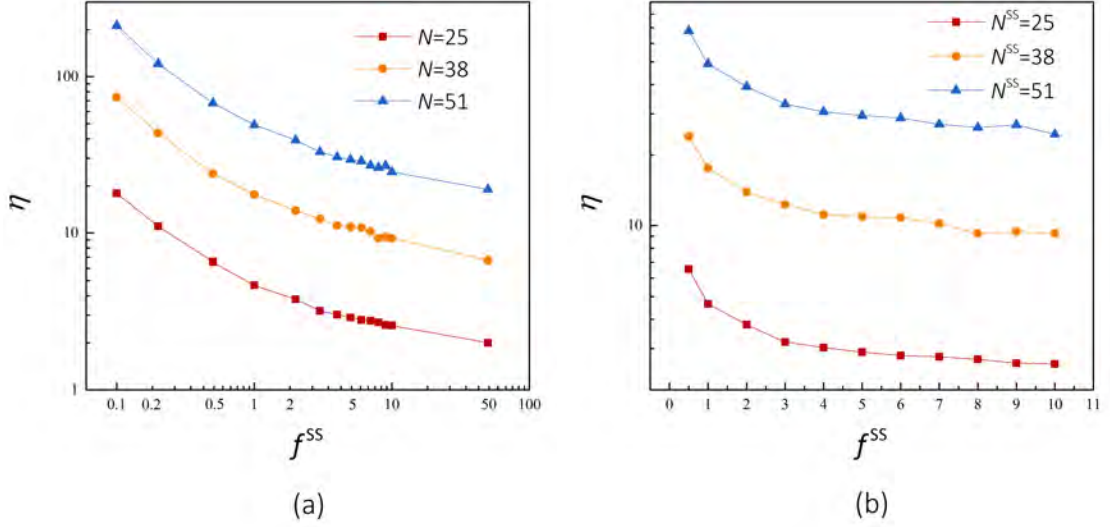
Figure 4.1: The viscosity η obtained at different frequency f^{SS} in the slip-spring model for linear chain systems with $N_{\mathrm{e}}^{\mathrm{SS}} = 4$ and $N_{\mathrm{s}}^{\mathrm{SS}} = 0.5$. (a) The logarithm plot with f^{SS} ranging from 0.1 to 50. (b) The linear plot zooming into the range of f^{SS} from 0.5 to 10.

η obtained at different f^{SS}, where η is given by

$$\eta = \int_0^\infty G(t)\mathrm{d}t.$$

As shown in Fig. 4.1(a), we choose three different chain lengths, $N = 25$, 38 and 51, to test their viscosities at the frequencies f^{SS} ranging over 2 decades, namely from 0.1 to 50, with the time-step $\Delta t = 0.05\tau_0$ and τ_0 is the slip-spring unit time [66]. In Fig. 4.1(a), η decreases fast when f^{SS} is smaller than 1. Afterwards, it decays much slower with increasing f^{SS}. If we zoom into the range from 0.5 to 10 and plot the data in the linear scale of f^{SS} (see Fig. 4.1(b)), the decrement of the viscosities at all chain lengths has an obvious "plateau-like" region after $f^{\mathrm{SS}} = 4$. In fact, η decreases by 30% when f^{SS} increases from 5 to 50. Similar phenomenon happens to the BD version, in which η drops by 30% when the friction of the slip-link decrease from $0.1\xi_0$ to $0.01\xi_0$ [66]. We conjecture such monotonic decease of η with increasing f^{SS}

or decreasing ξ^s as a consequence that in finite time-step the slip-links affects the mobility of the monomers connected by them, and thus influence the dynamics of the whole chain. Therefore, this effect can be eliminated by adjusting the horizontal shifting factor or the time mapping factor t_0.
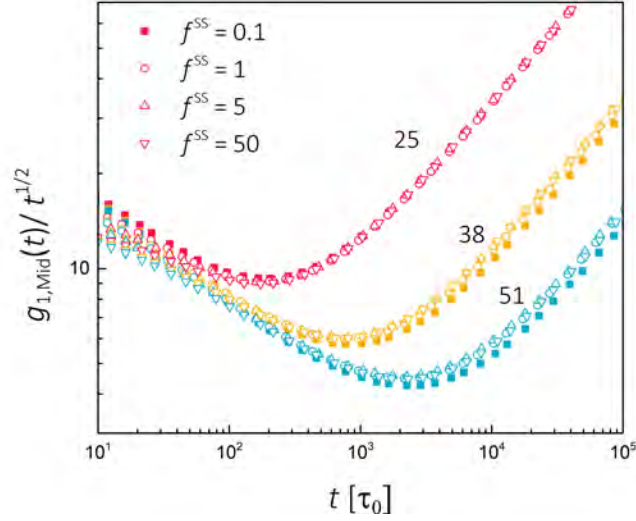
Figure 4.2: The horizontally shifted middle monomer mean-square displacements of linear chains at different MC frequency f^{SS}. The chain lengths are $N = 25$, 38 and 51 respectively. The shifting factors are adjusted to make the curves superimposed on each other at the chain length $N = 25$.

For further verification, we compare the middle monomer mean-square displacements $g_{1,\text{mid}}(t)$ of the chains at different f^{SS}, whose results are presented in Fig. 4.2. The curves of $g_{1,\text{mid}}(t)$ have been normalized by the Rouse power law $t^{1/2}$ in order to bring the curves into one decade along vertical axis. Four frequencies are chosen, namely $f^{SS} = 0.1$, 1, 5 and 50. According to Fig. 4.1, it is expected that when $f^{SS} > 4$ the slip-spring model should exhibit the same dynamics in late regimes after adjusting the time mapping factor t_0. For comparison, we shifted the curves of $g_{1,\text{mid}}(t)$ horizontally, making them superimposed at $N = 25$ and then use the same shifting factors for other chains lengths. As expected, the $g_{1,\text{mid}}(t)$ curves for

$f^{\text{SS}} = 5$ and 50 are superimposed in late regimes, while the curves for $f^{\text{SS}} = 0.5$ cannot overlap with those of other frequencies at the chain length $N = 38$ and 51. Therefore, we can define $f^{\text{SS}} = 5$ as a standard parameter of the MC version when $\Delta t = 0.05\tau_0$. With smaller Δt, $f^{\text{SS}} = 5$ should be reduced proportionally, e.g., $f^{\text{SS}} = 1$ when $\Delta t = 0.01\tau_0$.

4.3.2 Mapping Parameters

The parameters used to map slip-spring results to KG model data include the length-sale and time-scale mapping factors. On length scale, one must determine how many monomers in KG model are represented by one bead in the slip-spring model. This mapping number N_0 has an unique value for a certain pair of N_{e}^{SS} and N_{s}^{SS}. On time scale, the exact solution of the mapping factor t_0 due to coarse-graining remains unknown. But its value must be a constant for a given model, thus can be easily found by fitting the dynamic observables, such as the end-to-end relaxation function $\Phi(t)$ or the stress relaxation function $G(t)$. In Ref. [82], Wang et al. explored the parameter sets. When $N_{\text{e}}^{\text{SS}} = 4$ and $N_{\text{s}}^{\text{SS}} = 0.5$, they found the mapping parameters, $t_0 = 3370$ and $N_0 = 9.74$ for fully flexible KG linear chain model. On length scale, the mapping factor is non-arbitrary, but determined by N_0 and C_∞, where C_∞ is the characteristic ratio of the chain. For example, the vertical shifting factor for the end-to-end vector relaxation function $\Phi(t)$ is the product of C_∞ and N_0. In fully flexible KG model, C_∞ is around 1.82 [51].

It is expected that the length-scale mapping factor is independent of f^{SS}, but the time mapping factor t_0 can be affected by f^{SS} according to our previous discussion. To get the value of t_0, we performed a series of MD simulations using fully flexible KG model of linear chains, whose lengths are $M = 256, 320, 384, 448$ and 512, respectively. With $N_0 = 10$, the chain lengths used in the slip-spring model simulations are $N = 26, 32, 38, 45$ and 51 respectively. As shown in Fig. 4.3(a), the data of the slip-spring model on $\Phi(t)$ agree well with the MD results at all chain
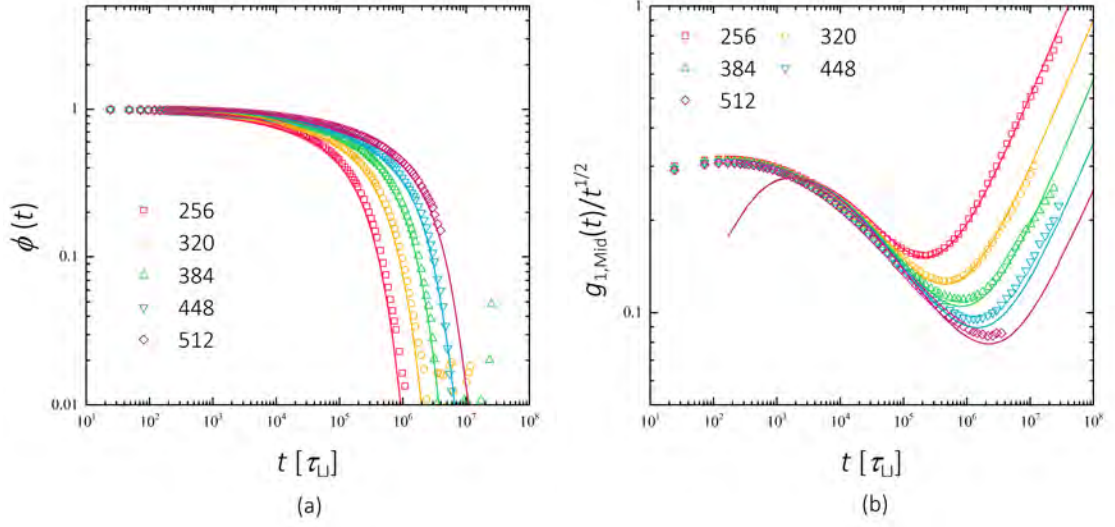
Figure 4.3: Mapping of the slip-spring model results (lines) obtained with $f^{\mathrm{SS}} = 5$ and $\Delta t = 0.05\tau_0$ to the data of fully flexible KG model (symbols) for linear chains on the end-to-end relaxations $\Phi(t)$ and the middle monomer mean-square displacements $g_{1,\mathrm{mid}}(t)$.

lengths when using $t_0 = 3400$. This value is very close to the previous work [82]. A further check is carried out on the middle monomer mean-square-displacements, $g_{1,\mathrm{mid}}(t)$, as shown in Fig. 4.3(b). This is a more strict examination, because the single bead diffusion is very sensitive to the slip-spring parameters, especially after τ_{e}. Again, $g_{1,\mathrm{mid}}(t)$ is divided by $t^{1/2}$ to bring the curves into one decade for better comparison. The standard parameter setting fits the simulation data very well in the middle and late regimes. The fitting in early regime, $t < \tau_{\mathrm{e}}$, could be improved by finer-graining. In Refs. [115] and [82], the finer-grained slip-spring model simulations were performed with $N_{\mathrm{e}}^{\mathrm{SS}} = 8$ and $N_{\mathrm{e}}^{\mathrm{SS}} = 1$, which gives better resolution in early regimes.

4.4 Relaxation of the Branched Polymers

4.4.1 Simulation Systems

Fig. 4.4 presents the schematic plot of the branched polymer architectures investigated in this work, including symmetric stars, asymmetric stars and H-polymers. For convenience, several subscripts are added on "N" and "M" to denote different architectures, i.e., "sym" for symmetric star, "asy" for asymmetric star, and "h" for H-polymer. The superscripts are added on "N" and "M" to denote the types of subchains, i.e. "l" and "s" represent long and short arm in an asymmetric star, while "t" and "a" respectively represent the cross-bar and the arm in a H-polymer, respectively.
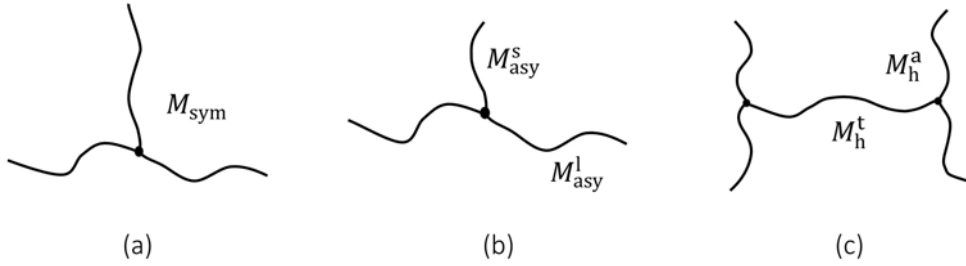
Figure 4.4: Sketches of branched polymer architectures: (a) Symmetric star, (b) Asymmetric star, (c) H-polymer.

The MD simulation systems are listed in Table 4.1. Five symmetric stars are investigated, whose arm lengths vary from 64 to 384. For asymmetric stars, two long-arm lengths are chosen, i.e., $M_{\mathrm{asy}}^{\mathrm{l}} = 256$ and 384. We only choose one cross-bar length $M_{\mathrm{h}}^{\mathrm{t}} = 256$ in H-polymers due to extraordinarily long relaxation time. In all cases, there are 100 molecules in the central simulation box. Thus the biggest system has $115,300$ particles. The number of molecules is large enough to ensure the end-to-end distance or radius of gyration is less than 2/3 of the cubic box size, whereby the finite size effect is negligible. With a time-step $\Delta t = 0.012\tau_{\mathrm{LJ}}$, the total

Symmetric Star		Asymmetric Star				H-Polymer			
M_{sym}	N_{sym}	$M_{\text{asy}}^{\text{l}}$	$M_{\text{asy}}^{\text{s}}$	$N_{\text{asy}}^{\text{l}}$	$N_{\text{asy}}^{\text{s}}$	M_{h}^{t}	M_{h}^{a}	N_{h}^{t}	N_{h}^{a}
64	6	256	64	25	6	256	64	25	6
128	13	256	128	25	13	256	128	25	13
256	25	384	64	38	6				
320	32	384	128	38	13				
384	38	384	256	38	25				

Table 4.1: Molecular structure parameters used in the KG model (M), and the corresponding slip-spring model (N).

simulation time reaches $5 \times 10^7 \tau_{\text{LJ}}$, covering a time range of 9 decades.

The simulation systems of slip-spring model are also listed in Table 4.1. In the slip-spring model, each bead corresponds to 10 monomers in the KG model. Accordingly, each branch-point bead in the 3-arm stars or H-polymers represents the corresponding branch-point monomer in the KG model plus 3 monomers from each subchain connected to it. In all slip-spring model simulations, the total number of molecules in the ensemble is set to be 30, which is sufficient to obtain good statistics of the measured observables. Each simulation runs roughly about 2 hours on a single CPU to achieve more than 10 terminal relaxation times.

4.4.2 MD Simulation Results

In this subsection, we will focus on the monomer mean-square displacements of different branched polymers obtained from MD simulations. Those observables provide rich microscopic information in microscopic dynamics, and are usually compared with the relaxation regimes predicted by the tube theory [17].

Fig. 4.5 presents the middle monomer mean-square displacements $g_{1,\text{mid}}(t)$ of the symmetric stars. In Fig. 4.5(a) and (b), the $g_{1,\text{mid}}(t)$ data (open symbols) have been
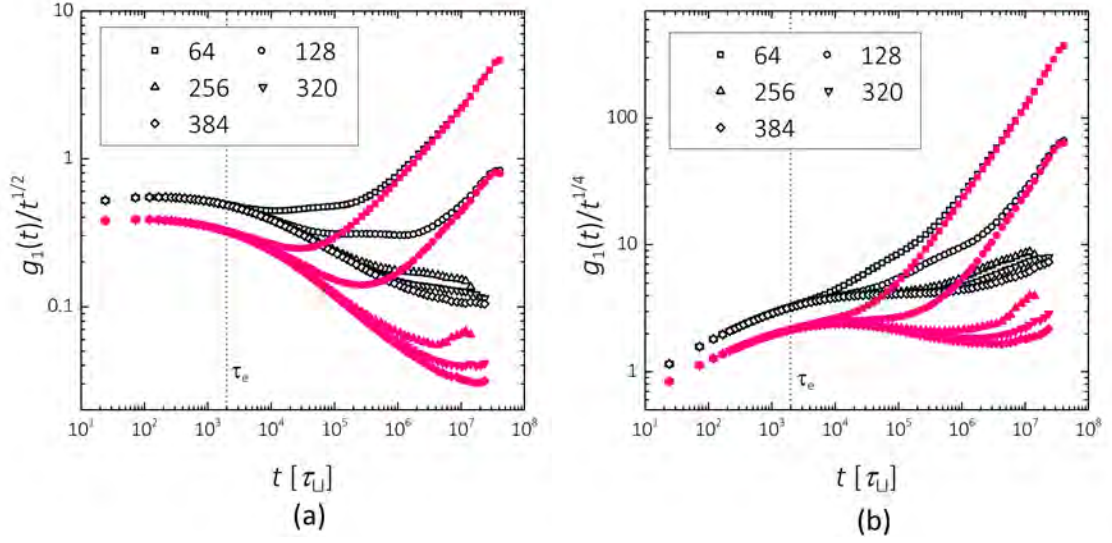
Figure 4.5: MD results on the mean-square displacements of the middle monomers of the arms $g_{1,\mathrm{mid}}(t)$ (open symbols) and the branch points $g_{1,\mathrm{branch}}(t)$ (solid symbols) for symmetric stars.

divided by $t^{1/2}$ and $t^{1/4}$ to reveal different regimes, respectively. At time scales $t < \tau_{\mathrm{e}}$, the monomers are not aware of the topological constraints imposed by surrounding chains, and thus follow the standard Rouse motion, $g_{1,\mathrm{mid}}(t) \sim t^{1/2}$. As a result, the first plateau-like regime is found before τ_{e} (dashed line) in Fig. 4.5(a). At time scales $\tau_{\mathrm{e}} < t < \tau_{\mathrm{R}}$, the monomer diffusion follows "constraint Rouse", where the star arm experiences 1D Rouse relaxation in the confining tube, leading to a power law of $g_1(t) \sim t^{1/4}$. Thus, in Fig. 4.5(b), a plateau regime can be found in $g_{1,\mathrm{mid}}(t)$ curves after τ_{e}, whose width increases with the growing arm length due to the power law of $\tau_{\mathrm{R}} \sim M_{\mathrm{sym}}^2$. For $M_{\mathrm{sym}} = 64$, the barely observed plateau implies that τ_{R} of the arm is roughly equal to τ_{e} and thus the entanglement segment length is about 64, which is consistent with the measured $M_{\mathrm{e}} \approx 50 - 65$ by mean-square displacement data in Ref. [82]. In tube theory, a scaling law of $g_1(t) \sim t^{1/2}$ is predicted at time scales $\tau_{\mathrm{R}} < t < \tau_{\mathrm{d}}$. However, this region is hard to observe in linear chain melts [82], because τ_{R} and τ_{d} are proportional to the square and cubic of the chain length

respectively, which requires very long chains to distinguish τ_R and τ_d in logarithm scale. The $g_1 \sim t^{1/2}$ power law is predicted for reptation (1D random walk in the tube) of linear chains. For stars, the relaxation proceeds by arm retraction, the behaviour could be somewhat different. But the separation between τ_R and τ_d due to the exponentially slow relaxation leads to a regime where $g_1(t)$ grows slowly after τ_R. At time scales $t > \tau_d$, the monomers follow free diffusion, $g_{1,\mathrm{mid}}(t) \sim t$. It is important to note that the semi-flexible KG model leads to different power laws in two regimes, $t < \tau_e$ and $\tau_e < t < \tau_R$, where $g_1(t)$ are proportional to $t^{0.6}$ and $t^{0.3}$ respectively [57, 82]. Therefore, the fully flexible model agrees better with the tube model.

Another interesting observable is the branch point mean-square displacement $g_{1,\mathrm{branch}}(t)$. The $g_{1,\mathrm{branch}}(t)$ data for symmetric stars are shown by the solid symbols in Fig. 4.5. Due to the connections with more than 2 monomers, the Rouse motion of the branch point is different from other monomers. At time scales $\tau_e < t < \tau_R$, $g_{1,\mathrm{branch}}(t)$ roughly follows $t^{1/5}$ scaling for $M_{\mathrm{sym}} > 256$ rather than $t^{1/4}$, due to the cage effect. In Fig. 4.5(a), the minimum of the $g_{1,\mathrm{branch}}(t)$ curve corresponds to the terminal relaxation time τ_d, after which the branch point follows free diffusion, $g_{1,\mathrm{branch}}(t) \sim t$.

For asymmetric stars, the $g_{1,\mathrm{branch}}(t)$ exhibits a significant speeding-up due to the shortening of one arm. Fig. 4.6(a) presents a comparison between the $g_{1,\mathrm{branch}}(t)$ data of the symmetric and asymmetric stars. The arm lengths of the symmetric stars are 256 and 384. Shortening one arm of the symmetric stars into 64, 128, or 256 for $N_{\mathrm{sym}} = 384$, the mobility of the branch point increases significantly at time scales $\tau_e < t < \tau_d$. The earlier terminal relaxation brought by shortening one arm is reflected in the arm end-to-end relaxation $\Phi(t)$. As shown in Fig. 4.6(b), we present $\Phi(t)$ of long arms of the asymmetric stars, which are compared with $\Phi(t)$ of the symmetric stars. The linear chains with the lengths of 512 and 768 are treated as 2-arm symmetric stars, whose arm end-to-end relaxations $\Phi_{\mathrm{mid}}(t)$ are also plotted in
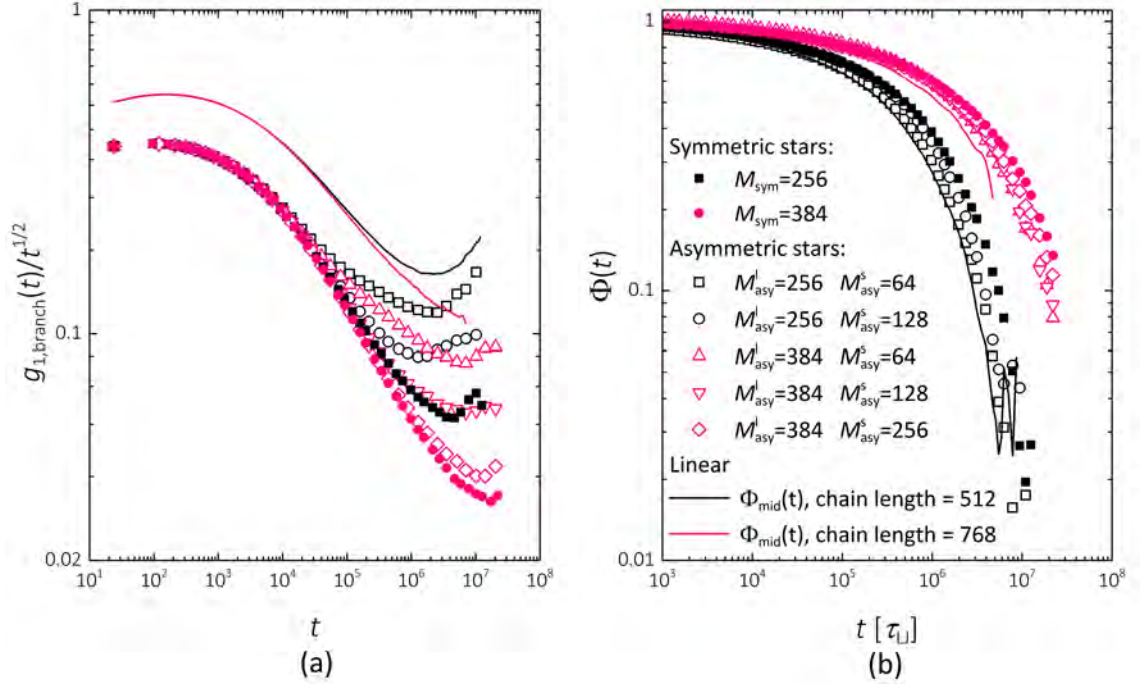
Figure 4.6: (a) MD results on branch point mean-square displacement $g_{1,\text{branch}}(t)$ of the symmetric and asymmetric stars, and middle monomer mean-square displacement $g_{1,\text{mid}}(t)$ of the linear chains. (b) End-to-end relaxation $\Phi(t)$ of the arms of the symmetric stars and the longer arms of the asymmetric stars, and middle-to-end relaxation $\Phi_{\text{mid}}(t)$ of the linear chains. The same symbols are used in both figures.

Fig. 4.6(b). The terminal arm end-to-end relaxation time τ_d of the symmetric star with the arm length $M_{\text{sym}} = 256$ is around $3.8 \times 10^6 \tau_{\text{LJ}}$. For the asymmetric star with $M_{\text{asy}}^l = 256$ and $M_{\text{asy}}^s = 64$, τ_d of the longer arms is around $2.5 \times 10^6 \tau_{\text{LJ}}$, which is almost equal to τ_d of the linear chains with a length of 512. In this case, the short arms seem to have little effect on the terminal relaxation time when attaching them to the middle monomer of linear chains, but leads to a slower Rouse motion due to extra connection.

For H-polymers, we present the mean-square displacements of the branch points $g_{1,\text{branch}}(t)$ and the middle monomers of the cross-bars $g_{1,\text{mid}}^t(t)$, as shown in Fig.
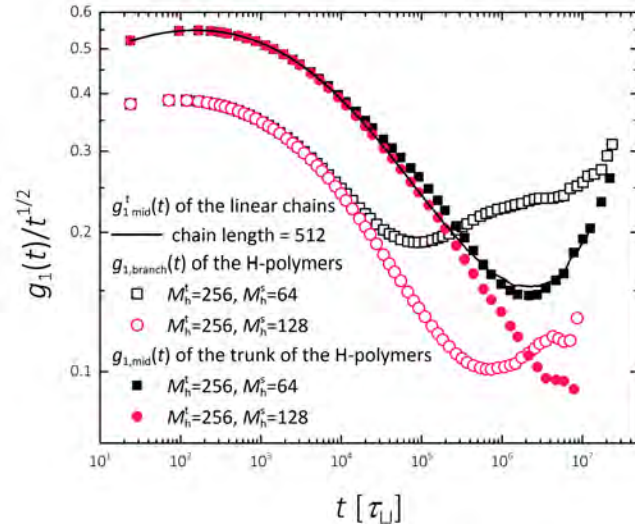
Figure 4.7: MD results on mean-square displacement of the branch points $g_{1,\mathrm{branch}}(t)$ and the middle monomers $g_{1,\mathrm{mid}}^t(t)$ in the H-polymers together with that of middle monomers of linear chains.

4.7. The normalized $g_{1,\mathrm{branch}}(t)$ reaches the minimum earlier than $g_{1,\mathrm{mid}}^t(t)$ of cross-bar by more than a decade, implying that the arm relaxation happens much earlier than the cross-bar relaxation. According to the "hierarchical" hypothesis [39, 120], after the relaxation time of the branch arms, the cross-bar do reptation with higher effective frictions at the two ends arisen from the relaxed arms. Therefore, the shape of $g_{1,\mathrm{mid}}^t(t)$ of cross-bar should be similar to that of linear chains. In Fig. 4.7, one can find that $g_{1,\mathrm{mid}}(t)$ of the linear chain with a length of 512 is almost the same as $g_{1,\mathrm{mid}}^t(t)$ of the H-polymer with $M_{\mathrm{h}}^t = 256$ and $M_{\mathrm{h}}^s = 64$. It could be a coincidence since the molecular weight of them are equal, but can also imply that the short arm length $M_{\mathrm{h}}^a = 64$ has weak entanglement.

4.4.3 Slip-Spring Model for Branched Polymers

In this subsection, we first present the simulation results of the current slip-spring model with MC moves on the branched polymers discussed above. Fig. 4.8(a)

presents the results of symmetric stars, including the arm end-to-end relaxation $\Phi(t)$, the branch point mean-square displacement $g_{1,\text{branch}}(t)$ and the middle monomer mean-square displacement of arms $g_{1,\text{mid}}(t)$. The slip-spring model results have been shifted to map the MD simulation data with the mapping parameters exactly the same as those used in linear chains, i.e., $N_0 = 10$ and $t_0 = 3400$. It is found that the agreement is good for all observables. Therefore, current slip-spring model, which has only CR and arm-retraction as the relaxation mechanisms, is sufficient to describe the slightly and mildly entangled symmetric stars. We can expect that it also works for the well-entangled symmetric stars. This is reasonable, because for such polymers, the terminal relaxation times of the systems are the same as the arm retraction times.

The simulation results of the asymmetric stars are given in Fig. 4.8(b), including the arm end-to-end relaxation $\Phi(t)$, the middle monomer mean-square displacement of long arms $g_{1,\text{mid}}^{\text{l}}(t)$, and the branch point mean-square displacement $g_{1,\text{branch}}(t)$. In these plots, significant discrepancies can be found in the $g_{1,\text{branch}}$ and $g_{1,\text{mid}}^{\text{l}}(t)$ data for most asymmetric stars except the one with $M_{\text{asy}}^{\text{l}} = 384$ and $M_{\text{asy}}^{\text{s}} = 256$. We presume this is due to the lower asymmetricity, i.e., the short arm length is relatively closer to the long arm length than other asymmetric stars. The discrepancies of other asymmetric stars occur at time scales close to τ_{d} of long arms, where $g_{1,\text{mid}}^{\text{l}}(t)$ and $g_{1,\text{branch}}(t)$ curves predicted by the slip-spring model are both lower than the MD results. The significantly underestimated mobility of branch points and middle monomers indicates that CR and arm-retraction are insufficient to describe the relaxation of asymmetric stars, especially for those with larger asymmetricity. On $\Phi(t)$, however, the slip-spring results agree well with the MD results for both short arms and long arms, which might be because the shape of $\Phi(t)$ is not strongly affected by the branch point motion.

In H-polymers, the current slip-spring model also does not work. As shown in Fig. 4.9. $\Phi(t)$ of the cross-bar reaches a plateau after the Rouse relaxation, because
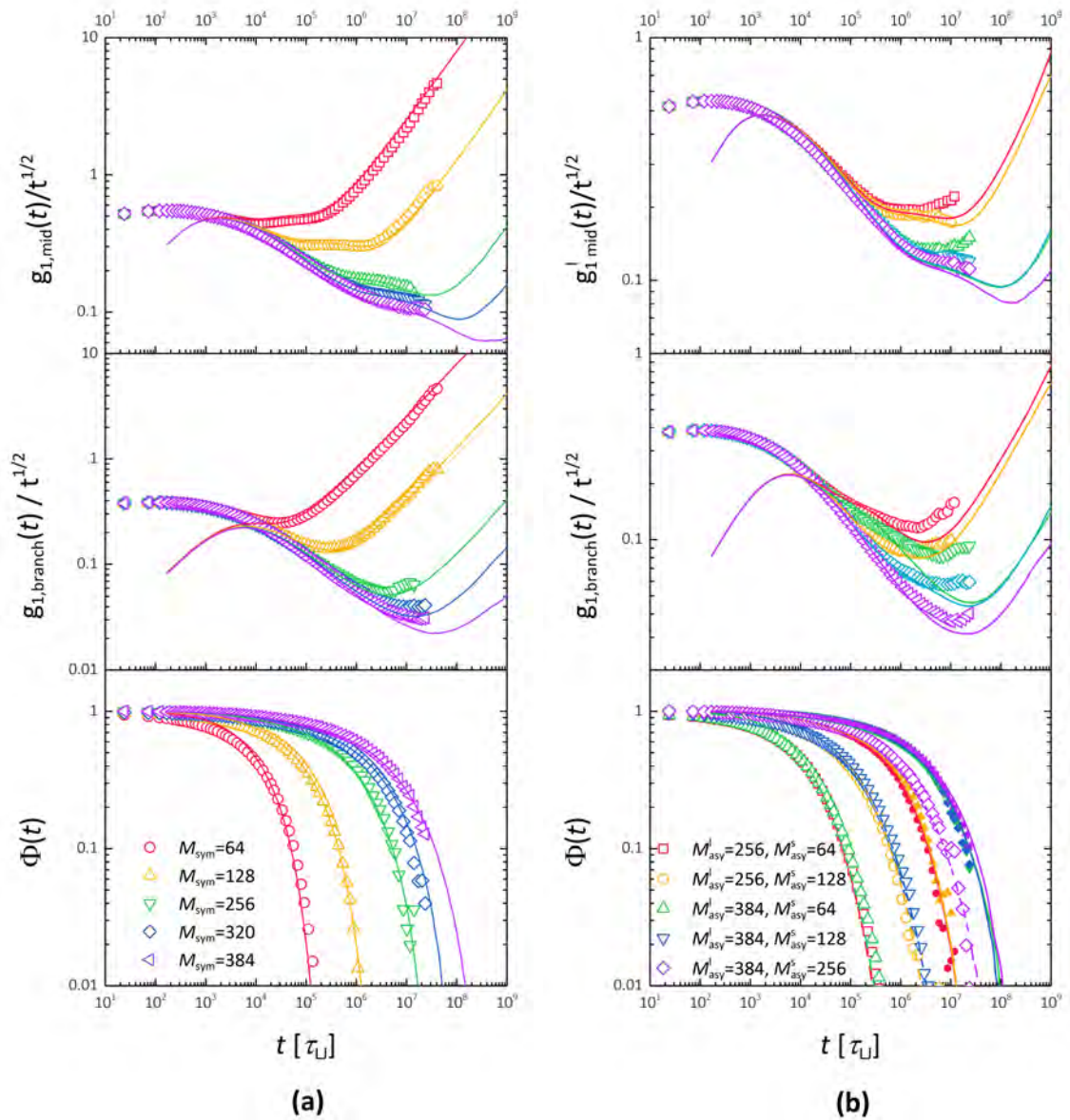
Figure 4.8: Simulation results of the previous slip-spring model and the KG model on the end-to-end relaxation $\Phi(t)$, the branch point mean-square displacement $g_{1,\text{branch}}(t)$, and the middle monomer mean-square displacement $g_{1,\text{mid}}(t)$ for (a) the symmetric stars, and (b) asymmetric stars. In asymmetric stars, we only plot $g^l_{1,\text{mid}}(t)$ for long arms. The symbols and lines are the results of the KG model and the slip-spring model, respectively. In bottom plot of (b), the solid symbol and lines are for the long arms, while the open symbols and dashed lines are for the short arms.
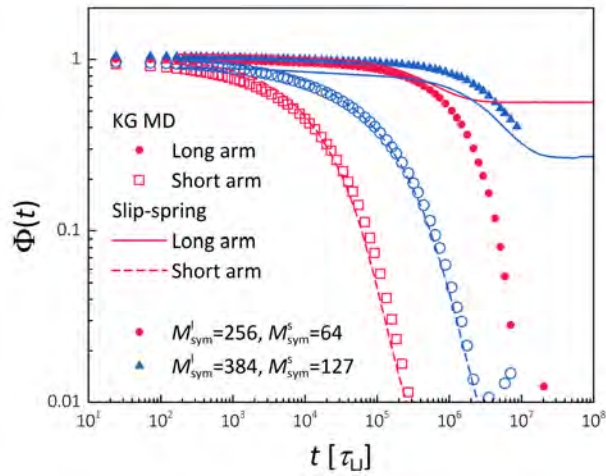
Figure 4.9: The simulation results of the slip-spring (lines) and MD using KG model (symbols) on $\Phi(t)$ of the H-polymers.

the slip-links on the cross-bar are blocked at the two branch points. The results in Fig. 4.8(b) and 4.9 imply that the failure of slip-spring model on asymmetric stars and H-polymer may originate from the same problem: the entanglements should be allowed to cross the branch point in some conditions; or in other words, the branch point can "hop" along the confining tube of the two long arms of an asymmetric star, or the confining tube of the cross-bar and one arm in a H-polymer.

In Ref. [63], Shanbhag and Larson proposed a slip-link model for branched polymers, in which they assume that the branch point hops when the slip-links on the short arm are all removed, corresponding to a complete arm retraction event. The advantage of this assumption is that it requires no additional parameters. In this work, we can introduce a parameter-free slip-link "hopping" mechanism in current slip-spring model, i.e., the slip-link can cross the branch point and hop onto another arm when the 3rd arm is fully relaxed. This hopping step is taken using the standard MC step of slip-spring model, thus requiring no additional parameters. It must be noted that the slip-link hopping in H-polymers only occurs between cross-bar and one arm.

With this slip-link "hopping" mechanism, we plot the results of the slip-spring model for symmetric stars in Fig. 4.10. The results on arm end-to-end relaxations $\Phi(t)$ and mean-square displacements for both branch points $g_{1,\mathrm{branch}}(t)$ and middle monomers of arms $g_{1,\mathrm{mid}}(t)$ show little difference from Fig. 4.8(a). In Fig. 4.10(d), we also present the average waiting time of one "hopping" event for each subchain, τ_{hop}, which is proportional to the inverse of the hopping rate on each branch point r_{hop}:

$$\tau_{\mathrm{hop}} = \frac{q}{r_{\mathrm{hop}}}, \tag{4.2}$$

where q is branch point functionality (i.e. the number of subchains connected to one branch point). In one time-step, a slip-link can cross a branch point many time when $f^{\mathrm{ss}} > 1$, we consider the frequent crossings due to the algorithm of slip-link diffusion should only be counted once for each time-step if the hopping succeeds. As shown in Fig. 4.10(d), τ_{hop} is equal to τ_{d} of the arm end-to-end relaxation function when the arm length M_{sym} is smaller than 128, after which τ_{hop} is even larger than τ_{d}. Thus, in symmetric stars, contribution of slip-link hopping to relaxation is negligible, which also explains why the original slip-link model can well describe symmetric stars.

For asymmetric stars, the relaxation times of the short arms $\tau_{\mathrm{d}}^{\mathrm{s}}$ and the long arms $\tau_{\mathrm{d}}^{\mathrm{l}}$ are well separated, thus the relaxation can be accelerated by the "hopping" mechanism. Fig. 4.11(a) shows the mean-square displacements of branch points $g_{1,\mathrm{branch}}(t)$ and middle monomers for both long arms $g_{1,\mathrm{mid}}^{l}(t)$ and short arms $g_{1,\mathrm{mid}}^{s}(t)$ in the slip-spring model simulations, which are found to be in good agreement with the MD results of KG model. Comparing to Fig. 4.8(b), the slip-spring model with slip-link hopping mechanism not only predicts the separation of $g_{1,\mathrm{mid}}^{l}(t)$ of the asymmetric stars with different short-arm lengths, but also well predicts the higher mobility of branch points in the terminal regime. In Fig. 4.11(b), the arm end-to-end relaxation $\Phi(t)$ is similar to Fig. 4.8(b), showing that the hopping mechanism does not affect the prediction of $\Phi(t)$. In Fig. 4.11(c), τ_{hop} of the asymmetric stars as calculated using Eq. 4.2 are compared with the end-to-end terminal relaxation times
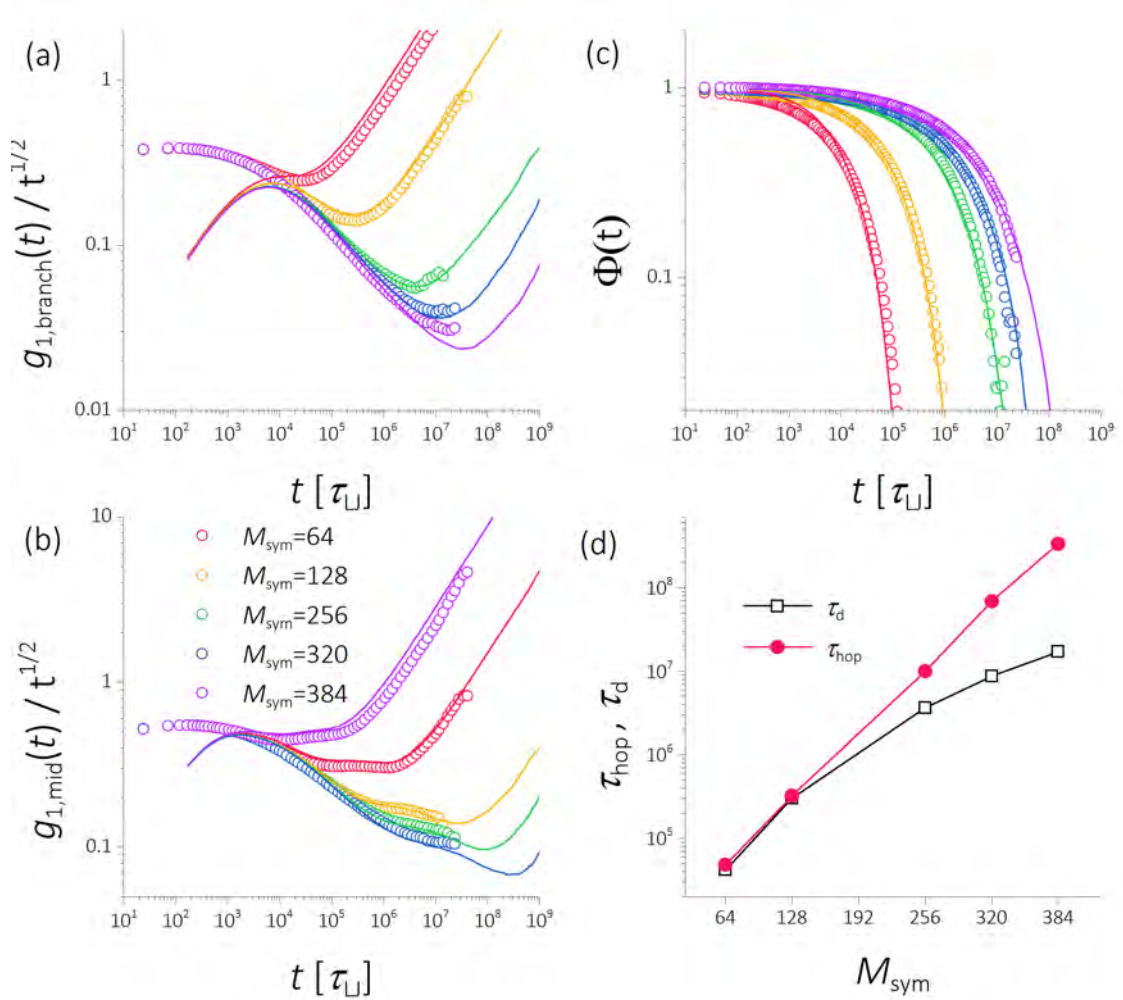
Figure 4.10: Simulation results of the slip-spring model with slip-link "hopping" mechanism at the branch point in comparison with the MD data using the KG model for the symmetric stars: (a) the branch point mean-square displacements $g_{1,\mathrm{branch}}(t)$, (b) the middle monomer mean-square displacements $g_{1,\mathrm{mid}}(t)$, (c) the arm end-to-end vector relaxations $\Phi(t)$, (d) the average waiting times of one "hopping" event for each subchain τ_{hop} and the end-to-end terminal relaxation times τ_{d}.
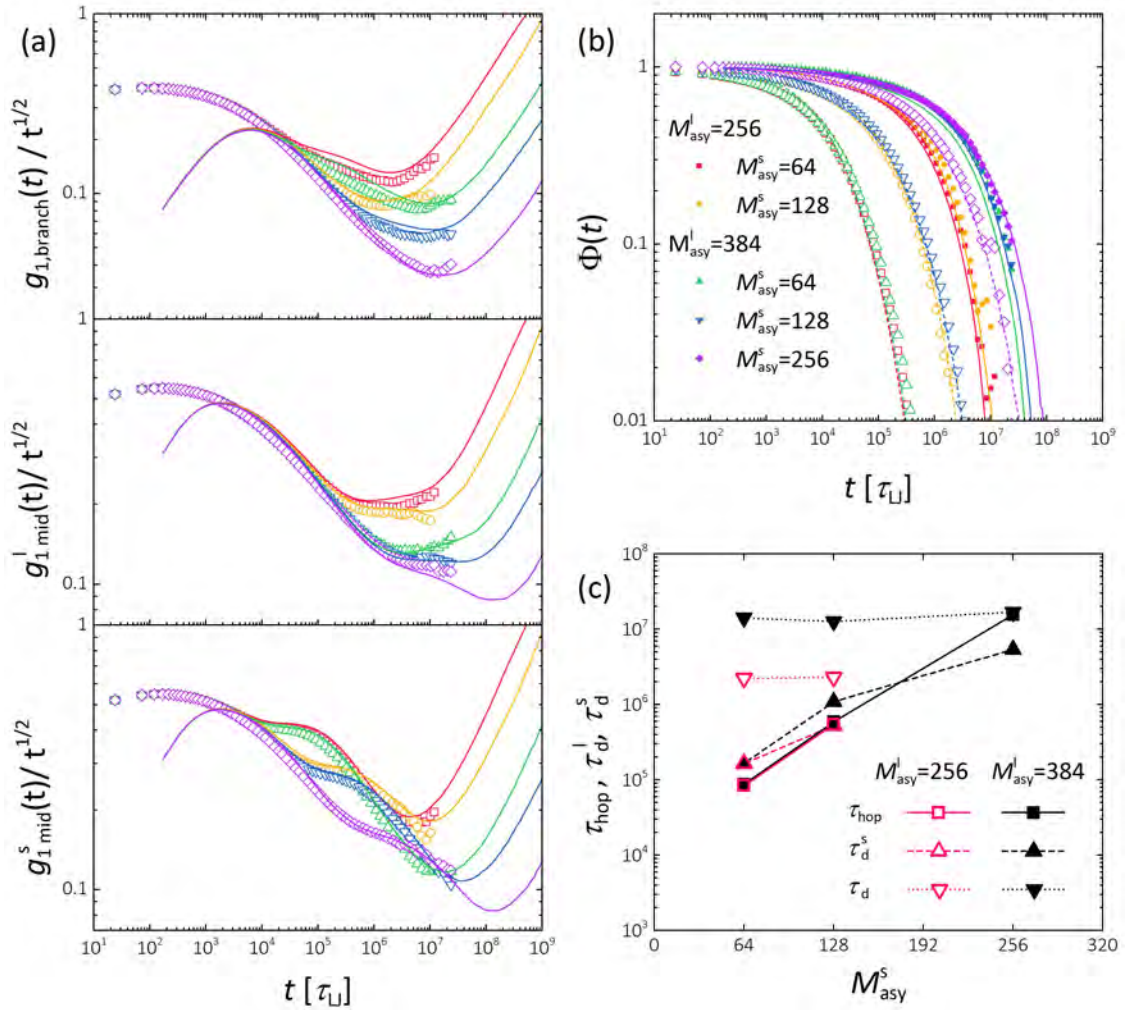
Figure 4.11: Simulation results of the slip-spring model with slip-link "hopping" mechanism at the branch point in comparison with the MD data using the KG model for the asymmetric stars: (a) the mean-square displacements of the branch points $g_{1,\mathrm{branch}}(t)$, the middle monomers of long arms $g^{\mathrm{l}}_{1,\mathrm{mid}}(t)$, and the middle monomers of short arms $g^{\mathrm{s}}_{1,\mathrm{mid}}(t)$, (b) the arm end-to-end relaxations $\Phi(t)$ (solid symbols and lines represent long arms, open symbols and dashed lines represent short arms), (c) the average waiting time of one "hopping" event for each subchain τ_{hop}, and the end-to-end terminal relaxation times of short arms $\tau^{\mathrm{s}}_{\mathrm{d}}$ and the long arms $\tau^{\mathrm{l}}_{\mathrm{d}}$.
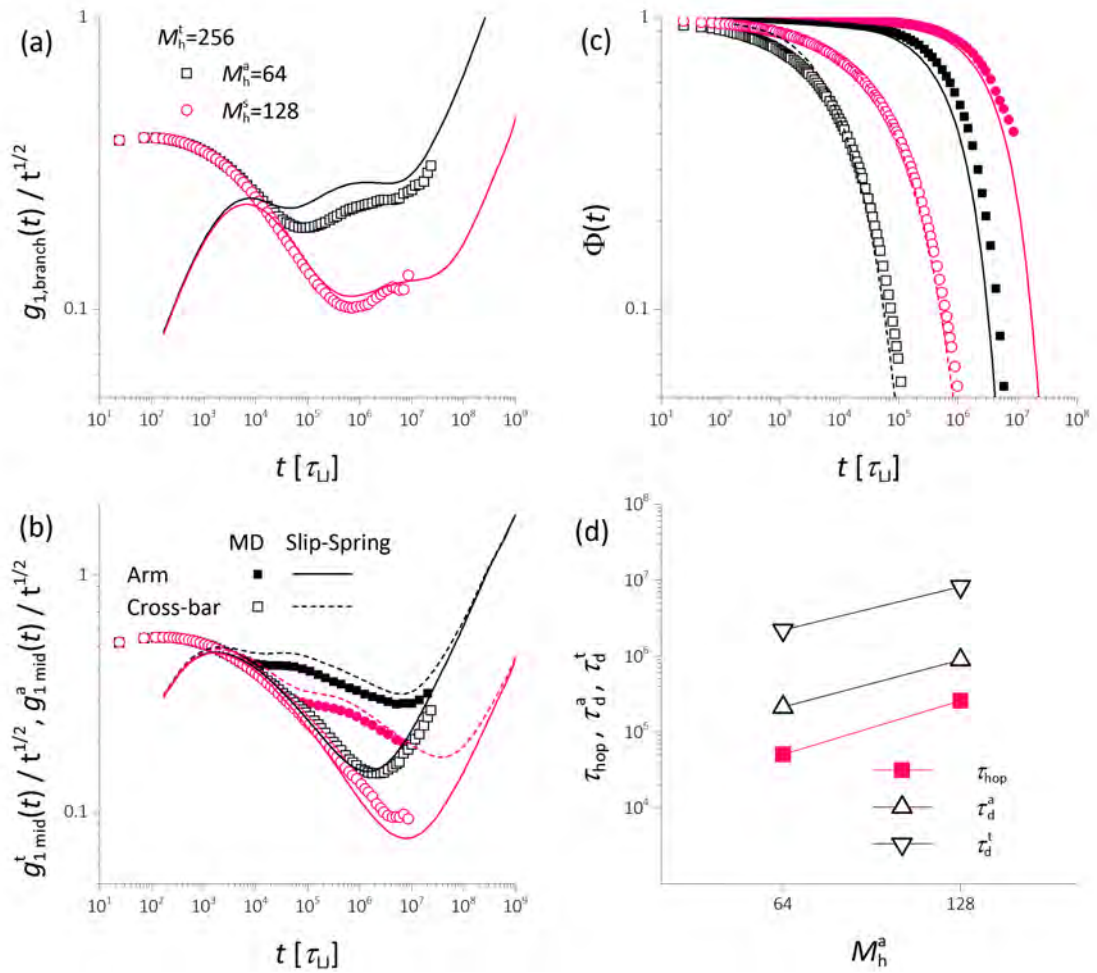
Figure 4.12: Simulation results of the slip-spring model with slip-link "hopping" mechanism at the branch point in comparison with the MD data using the KG model for the H-polymers: (a) the branch point mean-square displacements $g_{1,\mathrm{branch}}(t)$, (b) the mean-square displacements of the middle monomers of the arms $g^{\mathrm{a}}_{1,\mathrm{mid}}(t)$ and the cross-bars $g^{\mathrm{t}}_{1,\mathrm{mid}}(t)$, (c) the end-to-end relaxations $\Phi(t)$ (solid symbols and lines represent cross-bars, open symbols and dashed lines represent arms), (d) the average waiting time of one "hopping" event τ_{hop} for each subchain, and the end-to-end terminal relaxation times of the arms $\tau^{\mathrm{a}}_{\mathrm{d}}$ and the cross-bars $\tau^{\mathrm{t}}_{\mathrm{d}}$.

of long arms $\tau_{\mathrm{d}}^{\mathrm{l}}$ and short arms $\tau_{\mathrm{d}}^{\mathrm{s}}$. With identical short-arm length, τ_{hop} for different long-arm lengths are equal, indicating that the relaxation of short arms dominates the "hopping" probability. For most asymmetric stars, τ_{hop} is smaller than $\tau_{\mathrm{d}}^{\mathrm{s}}$ apart from the asymmetric star with $M_{\mathrm{asy}}^{\mathrm{l}} = 384$ and $M_{\mathrm{asy}}^{\mathrm{s}} = 256$, whose τ_{hop} is equal to $\tau_{\mathrm{d}}^{\mathrm{l}}$. Thus we can affirm that the hopping mechanism is trivial in the systems with low asymmetricity, which also explains why the slip-spring model without "hopping" mechanism can well describe this asymmetric star (see Fig. 4.8(b)).

In H-polymers, the cross-bar relaxation is dominated by the diffusion of branch points, thus a significant improvement of the slip-spring model for H-polymers can be achieved by incorporating such slip-link "hopping" mechanism, as shown in Fig. 4.12. For all observables considered, the agreement with the KG model is reasonably good. In Fig. 4.12(a), the $g_{1,\mathrm{branch}}(t)$ data for $M_{\mathrm{h}}^{\mathrm{a}} = 64$ is higher than the MD results by roughly 20% at time scales $\tau_{\mathrm{e}} < t < \tau_{\mathrm{d}}$. Similar disagreement can be found in the middle monomer mean-square displacements of the arms, as shown in Fig. 4.12(b). The overestimated branch point mobility for $M_{\mathrm{h}}^{\mathrm{a}} = 64$ is also reflected in the $\Phi(t)$ plots in Fig. 4.12(c), where the relaxation of the cross-bar is slightly faster than the MD result. This might result from the fast creation and deletion of the single slip-link at the free ends of the short arms which on average have less than two slip-springs. For H-polymer with longer arm length $M_{\mathrm{h}}^{\mathrm{a}} = 128$, the agreements on these observables become much better. In Fig. 4.12(d), τ_{hop} for both H-polymers are much shorter than the end-to-end terminal relaxation times of the arms τ_{d}^{m}. τ_{hop} for $M_{\mathrm{h}}^{\mathrm{a}} = 64$ and $M_{\mathrm{h}}^{\mathrm{a}} = 128$ are roughly half of τ_{hop} for asymmetric stars with $M_{\mathrm{asy}}^{\mathrm{s}} = 64$ and $M_{\mathrm{asy}}^{\mathrm{s}} = 128$, because there are two short arms connected to each branch point in H-polymers.

4.5 Conclusions

In this chapter, we presented a detailed description of the slip-spring model using Monte-Carlo algorithm to govern the motion of the slip-links. This version of the slip-spring model enables us to employ a larger time-step than the original Brownian dynamics version without changing the predicted dynamic properties. With a careful selection of the parameters, we obtained the simulation results of the slip-spring model on monodisperse linear chains, which are found to be in good agreement with those of the molecular dynamics simulations using the fully flexible Kremer-Grest model. In a standard parameter setting, i.e., $N_e^{SS} = 4$ and $N_s^{SS} = 0.5$, the mapping parameters for the fully flexible KG model are found to be $t_0 = 3400$ for time scale and $N_0 = 10$ for length scale, which are believed to be universal for different polymer architectures.

After the careful calibration, the slip-spring model was extended to branched polymers. In order to examine the slip-spring model results, we performed extensive molecular dynamics simulations using the flexible KG model for a variety of branched polymers, including the 3-arm symmetric and asymmetric stars, and the H-polymers. The slip-spring model results agree well with MD simulations on symmetric stars, but fail on both asymmetric stars and H-polymers. We consider this problem originating from the absence of some relaxation mechanisms in the model. One possible mechanism is that the slip-links can hop over a branch point between two subchains connected to it when the third arm has no slip-links on it. The modified slip-spring model with the "hopping" mechanism provides results in good agreement with MD data without requiring extra parameters. Such "hopping" mechanism is found to be important for asymmetric stars with significantly different arm lengths and essential for H-polymers.

Chapter 5

Conclusions

The study of the dynamics of entangled branched polymers is of both fundamental and practical importance. In the thesis, we focus on investigating the relaxation behaviours of entangled branched polymer with simple architectures.

Due to the steeply growing quadratic potential, arm retraction is a typical multidimensional first-passage problem, whose exact solution remains a open question. In the Milner-McLeish theory [30], this problem is simplified by treating the whole chain as one bead attached to the branch point via a harmonic spring. This solution, however, overestimated the relaxation time by neglecting the contributions of multiple Rouse modes. Cao et al. [54] presented an analytical solution to the multi-dimensional first-passage problem, which predicts an arm relaxation time in the absence of constraint release $2/N$ times smaller than that given by the Milner-McLeish theory, where N is the arm length. In order to examine the two theoretical models, we employ advanced numerical methods for studying first-passage problems, such as the forward flux sampling and weighted ensemble methods. These methods were first implemented to the simplest multi-dimensional first-passage problem: the escaping time of a Brownian particle in a 2D potential well. Due to its remarkable performance in all aspects, the FFS method was then chosen to study the extension problem of a 1D Rouse chain model, which is analogous to the arm-retraction

problem. We found that the first-passage time is getting shorter if the Rouse chain is represented by more beads, showing good agreement with the prediction of the asymptotic solution of Cao el al. [54].

Then the FFS method was implemented to solve the arm-retraction problem in the slip-spring model, which is a coarse-grained bead-spring model for entangled polymers. With a controllable precision, this method allows direct comparison between the slip-spring model and the tube theory for well-entangled star polymers with up to 16 entanglements per arm. Moreover, a study is conducted on the extraction of experimentally measurable observables from FFS simulations, such as the end-to-end vector and stress relaxation functions. We believe this work will not only expand the application of FFS method to polymer dynamics by reproducing full dynamic spectrum rather than just the first-passage time, but also to many other scientific areas.

After the remarkable success on linear melt systems, the slip-spring model has been extended to the study of the branched polymers [34, 101]. However, due to the absence of certain mechanisms, current slip-spring model cannot describe the relaxation behaviours of some architectures, such as asymmetric stars and H-polymers. To cope with it, we conducted a series of MD simulations for branched polymers with different architectures, including 3-arm symmetric and asymmetric stars, and H-polymers. With the fully flexible Kremer-Grest chain model, these simulations achieved the terminal relaxation time of the mildly entangled arms with up to 7 entanglements. The slip-spring model, whose parameters have been carefully calibrated according to the MD results of linear chains, was implemented to predict the relaxation behaviours of these branched polymers. Comparing the MD and slip-spring model simulation results, we found a significant discrepancy due to the missing mechanism aforementioned. In the tube theory for asymmetric stars, it is assumed that the branch point can hop a fraction of tube diameter when the short arm is fully relaxed. For the slip-spring model, we proposed a slip-link "hopping"

mechanism, which allows the slip-links to cross the branch point when the third arm is unentangled. Using this mechanism, the slip-spring model is shown to have a good agreement with the MD results.

In conclusion, many problem of entangled branched polymers dynamics remains open. Based on the achievements made in this thesis, future studies can be carried out in many aspects. One of the main challenges of branched polymer dynamics is the lack of clear microscopic picture of entanglements, which leads to numerous assumptions and fitting parameters in the current tube model. One solution is mapping a more fine-grained model onto a more coarse-grained one. This could effectively avoid the dependence on the exact definition of entanglements, while the missing mechanisms can still be revealed. In fact, this approach has been implemented in the fourth chapter to develop the slip-spring model for branched polymers by comparing its main results with MD simulations. In the second and third chapters, we have shown that the analytical and numerical solutions of the multi-dimensional first-passage time problem are effective to obtain the relaxation spectra of well entangled symmetric stars, which can be either modelled by the one dimensional Rouse model or the slip-spring model. Both models can be mapped onto the tube model, but further more their results can be compared with experiments and MD simulations, which could be useful to refine the tube theories, especially with constraint release. Another solution is to investigate the dynamic behaviours by analysing the evolution of entanglements in MD simulations. The powerful analysis tools, such as the "primitive path analysis" [51], and the newly developed "contact map analysis" [52] and "tube axis" [55] can pave the way to decipher the hidden mechanisms. For example, the constraint release events can be monitored by tracing the creation and destruction of entanglements in the middle of the chains, and the possible entanglement hopping mechanism of branched polymers can be detected by tracing the movements of entanglements close to the branch points. From these analysis, the distribution of the constraint release rates and the hopping distance

are available. Moreover, such an approach is very important to the investigation of entanglements in the nonlinear regime, since the solid evidences are most likely to come from MD simulations. In particular, one can figure out how does the number of entanglement change under flow, and thus help to improve the theories and models for nonlinear dynamics.

Bibliography

[1] W. Kuhn and H. Kuhn. Modellmässige deutung der inneren viskosität (der formzähigkeitskonstante) von fadenmolekeln i. *Helvetica Chimica Acta*, 29(3):609–626, 1946.

[2] W. Kuhn and H. Kuhn. Modellmässige deutung der inneren viskosität (der formzähigkeit) von fadenmolekeln ii. *Helvetica Chimica Acta*, 29(4):830–858, 1946.

[3] A. Tobolsky and H. Eyring. Mechanical properties of polymeric materials. *Journal of Chemical Physics*, 11(3):125–134, 1943.

[4] A. V. Tobolsky. Properties and structure of polymers. 1960.

[5] S. Onogi, T. Masuda, and K. Kitagawa. Rheological properties of anionic polystyrenes. I. Dynamic viscoelasticity of narrow-distribution polystyrenes. *Macromolecules*, 3(2):109–116, 1970.

[6] W. W. Graessley. *The entanglement concept in polymer rheology*. Springer, 1974.

[7] J. D. Ferry. *Viscoelastic properties of polymers*. John Wiley & Sons, 1980.

[8] H. Watanabe. Viscoelasticity and dynamics of entangled polymers. *Progress in Polymer Science*, 24(9):1253–1403, 1999.

[9] H. Janeschitz-Kriegl. *Polymer melt rheology and flow birefringence*, volume 6. Springer Science & Business Media, 2012.

[10] L. M. Wheeler and T. P. Lodge. Tracer diffusion of linear polystyrenes in dilute, semidilute, and concentrated poly (vinyl methyl ether) solutions. *Macromolecules*, 22(8):3399–3408, 1989.

[11] P. F. Green and E. J. Kramer. Matrix effects on the diffusion of long polymer chains. *Macromolecules*, 19(4):1108–1114, 1986.

[12] S. F. Edwards. The theory of rubber elasticity. *British Polymer Journal*, 9(2):140–143, 1977.

[13] R. C. Ball, M. Doi, S. F. Edwards, and M. Warner. Elasticity of entangled networks. *Polymer*, 22(8):1010–1018, 1981.

[14] P. E. Rouse Jr. A theory of the linear viscoelastic properties of dilute solutions of coiling polymers. *Journal of Chemical Physics*, 21(7):1272–1280, 1953.

[15] S. F. Edwards. The statistical mechanics of polymerized material. *Proceedings of the Physical Society*, 92(1):9, 1967.

[16] P.-G. de Gennes. Reptation of a polymer chain in the presence of fixed obstacles. *Journal of Chemical Physics*, 55:572–579, 1971.

[17] M. Doi and S. F. Edwards. *The theory of polymer dynamics*, volume 73. Oxford University Press, 1988.

[18] M. Doi. Explanation for the 3.4 power law of viscosity of polymeric liquids on the basis of the tube model. *Journal of Polymer Science Part C-Polymer Letters*, 19(5):265–273, 1981.

[19] W. W. Graessley and M. J. Struglinski. Effects of polydispersity on the linear viscoelastic properties of entangled polymers. 2. Comparison of viscosity

and recoverable compliance with tube model predictions. *Macromolecules*, 19(6):1754–1760, 1986.

[20] J. Des Cloizeaux. Relaxation of entangled polymers in melts. *Macromolecules*, 23(17):3992–4006, 1990.

[21] M. Rubinstein, E. Helfand, and D. S. Pearson. Theory of polydispersity effects of polymer rheology: binary distribution of molecular weights. *Macromolecules*, 20(4):822–829, 1987.

[22] M. Rubinstein and R. H. Colby. Self-consistent theory of polydisperse entangled polymers: Linear viscoelasticity of binary blends. *Journal of Chemical Physics*, 89(8):5291–5306, 1988.

[23] J. L. Viovy, M. Rubinstein, and R. H. Colby. Constraint release in polymer melts: tube reorganization versus tube dilation. *Macromolecules*, 24(12):3587–3596, 1991.

[24] A. E. Likhtman and T. C. B. McLeish. Quantitative theory for linear dynamics of linear entangled polymers. *Macromolecules*, 35(16):6332–6343, 2002.

[25] P. G. De Gennes. Reptation of stars. *Journal de Physique*, 36(12):1199–1203, 1975.

[26] M. Doi and N. Y. Kuzuu. Rheology of star polymers in concentrated solutions and melts. *Journal of Polymer Science: Polymer Letters Edition*, 18(12):775–780, 1980.

[27] D. S. Pearson and E. Helfand. Viscoelastic properties of star-shaped polymers. *Macromolecules*, 17(4):888–895, 1984.

[28] R. C. Ball and T. C. B. McLeish. Dynamic dilution and the viscosity of star-polymer melts. *Macromolecules*, 22(4):1911–1913, 1989.

[29] G. Marrucci. Relaxation by reptation and tube enlargement: a model for polydisperse polymers. *Journal of Polymer Science: Polymer Physics Edition*, 23(1):159–177, 1985.

[30] S. T. Milner and T. C. B. McLeish. Parameter-free theory for stress relaxation in star polymer melts. *Macromolecules*, 30(7):2159–2166, 1997.

[31] H. A. Kramers. Brownian motion in a field of force and the diffusion model of chemical reactions. *Physica*, 7(4):284–304, 1940.

[32] L. J. Fetters, D. J. Lohse, D. Richter, T. A. Witten, and A. Zirkel. Connection between polymer molecular weight, density, chain dimensions, and melt viscoelastic properties. *Macromolecules*, 27(17):4639–4647, 1994.

[33] S. T. Milner and T. C. B. McLeish. Arm-length dependence of stress relaxation in star polymer melts. *Macromolecules*, 31(21):7479–7482, 1998.

[34] J. Cao, J. Zhu, Z. Wang, and A. E. Likhtman. Large deviations of Rouse polymer chain: First passage problem. *Journal of Chemical Physics*, 143(20):204105, 2015.

[35] S. T. Milner, T. C. B. McLeish, R. N. Young, A. Hakiki, and J. M. Johnson. Dynamic dilution, constraint-release, and star-linear blends. *Macromolecules*, 31(26):9345–9353, 1998.

[36] A. L. Frischknecht, S. T. Milner, A. Pryke, R. N. Young, R. Hawkins, and T. C. B. McLeish. Rheology of three-arm asymmetric star polymer melts. *Macromolecules*, 35(12):4801–4820, 2002.

[37] S. T. Milner and T. C. B. McLeish. Reptation and contour-length fluctuations in melts of linear polymers. *Physical Review Letters*, 81(3):725, 1998.

[38] R. J. Blackwell, O. G. Harlen, and T. C. B. McLeish. Theoretical linear and nonlinear rheology of symmetric treelike polymer melts. *Macromolecules*, 34(8):2579–2596, 2001.

[39] R. G. Larson. Combinatorial rheology of branched polymer melts. *Macromolecules*, 34(13):4556–4571, 2001.

[40] D. R. Daniels, T. C. B. McLeish, B. J. Crosby, R. N. Young, and C. M. Fernyhough. Molecular rheology of comb polymer melts. 1. Linear viscoelastic response. *Macromolecules*, 34(20):7025–7033, 2001.

[41] T. C. B. McLeish. Tube theory of entangled polymer dynamics. *Advances in Physics*, 51(6):1379–1527, 2002.

[42] C. Das, N. J. Inkson, D. J. Read, M. A. Kelmanson, and T. C. B. McLeish. Computational linear rheology of general branch-on-branch polymers. *Journal of Rheology*, 50(2):207–234, 2006.

[43] H. Watanabe, Y. Matsumiya, E. Van Ruymbeke, D. Vlassopoulos, and N. Hadjichristidis. Viscoelastic and dielectric relaxation of a cayley-tree-type polyisoprene: Test of molecular picture of dynamic tube dilation. *Macromolecules*, 41(16):6110–6124, 2008.

[44] Z. Wang, X. Chen, and R. G. Larson. Comparing tube models for predicting the linear rheology of branched polymer melts. *Journal of Rheology (1978-present)*, 54(2):223–260, 2010.

[45] S. J. Park and R. G. Larson. Modeling the linear viscoelastic properties of metallocene-catalyzed high density polyethylenes with long-chain branching. *Journal of Rheology*, 49(2):523–536, 2005.

[46] E. Van Ruymbeke, R. Keunings, and C. Bailly. Prediction of linear viscoelastic properties for polydisperse mixtures of entangled star and linear polymers:

Modified tube-based model and comparison with experimental results. *Journal of Non-Newtonian Fluid Mechanics*, 128(1):7–22, 2005.

[47] E. Van Ruymbeke, C. Bailly, R. Keunings, and D. Vlassopoulos. A general methodology to predict the linear rheology of branched polymers. *Macromolecules*, 39(18):6248–6259, 2006.

[48] E. Van Ruymbeke, K. Orfanou, M. Kapnistos, H. Iatrou, M. Pitsikalis, N. Hadjichristidis, D. J. Lohse, and D. Vlassopoulos. Entangled dendritic polymers and beyond: Rheology of symmetric Cayley-tree polymers and macromolecular self-assemblies. *Macromolecules*, 40(16):5941–5952, 2007.

[49] K. Kremer and G. S. Grest. Dynamics of entangled linear polymer melts: A molecular-dynamics simulation. *Journal of Chemical Physics*, 92(8):5057–5086, 1990.

[50] R. Auhl, R. Everaers, G. S. Grest, K. Kremer, and S. J. Plimpton. Equilibration of long chain polymer melts in computer simulations. *Journal of Chemical Physics*, 119(24):12718–12728, 2003.

[51] R. Everaers, S. K. Sukumaran, G. S. Grest, C. Svaneborg, A. Sivasubramanian, and K. Kremer. Rheology and microscopic topology of entangled polymeric liquids. *Science*, 303(5659):823–826, 2004.

[52] A. E. Likhtman and M. Ponmurugan. Microscopic definition of polymer entanglements. *Macromolecules*, 47(4):1470–1481, 2014.

[53] D. J. Read, K. Jagannathan, and A. E. Likhtman. Entangled polymers: Constraint release, mean paths, and tube bending energy. *Macromolecules*, 41(18):6843–6853, 2008.

[54] J. Cao and Z. Wang. Microscopic Picture of Constraint Release Effects in Entangled Star Polymer Melts. *Macromolecules*, 49(15):5677–5691, 2016.

[55] A. E. Likhtman. The tube axis and entanglements in polymer melts. *Soft matter*, 10(12):1895–1904, 2014.

[56] Q. Zhou and R. G. Larson. Direct molecular dynamics simulation of branch point motion in asymmetric star polymer melts. *Macromolecules*, 40(9):3443–3449, 2007.

[57] P. Bačová, L. G. D. Hawke, D. J. Read, and A. J. Moreno. Dynamics of branched polymers: A combined study by molecular dynamics simulations and tube theory. *Macromolecules*, 46(11):4633–4650, 2013.

[58] M. Doi and S. F. Edwards. Dynamics of concentrated polymer systems. Part 2.-Molecular motion under flow. *Journal of the Chemical Society, Faraday Transactions 2: Molecular and Chemical Physics*, 74:1802–1817, 1978.

[59] C. C. Hua and J. D. Schieber. Segment connectivity, chain-length breathing, segmental stretch, and constraint release in reptation models. I. Theory and single-step strain predictions. *Journal of Chemical Physics*, 109(22):10018–10027, 1998.

[60] J. D. Schieber, J. Neergaard, and S. Gupta. A full-chain, temporary network model with sliplinks, chain-length fluctuations, chain connectivity and chain stretching. *Journal of Rheology*, 47(1):213–233, 2003.

[61] R. N. Khaliullin and J. D. Schieber. Self-consistent modeling of constraint release in a single-chain mean-field slip-link model. *Macromolecules*, 42(19):7504–7517, 2009.

[62] S. Shanbhag, R. G. Larson, J. Takimoto, and M. Doi. Deviations from dynamic dilution in the terminal relaxation of star polymers. *Physical Review Letters*, 87(19):195502, 2001.

[63] S. Shanbhag and R. G. Larson. A slip-link model of branch-point motion in entangled polymers. *Macromolecules*, 37(21):8160–8166, 2004.

[64] Y. Masubuchi, J.-I. Takimoto, K. Koyama, G. Ianniruberto, G. Marrucci, and F. Greco. Brownian simulations of a network of reptating primitive chains. *Journal of Chemical Physics*, 115(9):4387–4394, 2001.

[65] Y. Masubuchi, G. Ianniruberto, F. Greco, and G. Marrucci. Primitive chain network simulations for branched polymers. *Rheologica Acta*, 46(2):297–303, 2006.

[66] A. E. Likhtman. Single-chain slip-link model of entangled polymers: Simultaneous description of neutron spin-echo, rheology, and diffusion. *Macromolecules*, 38(14):6128–6139, 2005.

[67] M. Langeloth, Y. Masubuchi, M. C. Böhm, and F. Müller-Plathe. Recovering the reptation dynamics of polymer melts in dissipative particle dynamics simulations via slip-springs. *Journal of Chemical Physics*, 138(10):104907, 2013.

[68] R. J. Allen, P. B. Warren, and P. R. Ten Wolde. Sampling rare switching events in biochemical networks. *Physical Review Letters*, 94(1):018104, 2005.

[69] G. A. Huber and S. Kim. Weighted-ensemble Brownian dynamics simulations for protein association reactions. *Biophysical journal*, 70(1):97, 1996.

[70] B. W. Zhang, D. Jasnow, and D. M. Zuckerman. The "weighted ensemble" path sampling method is statistically exact for a broad class of stochastic processes and binning procedures. *Journal of Chemical Physics*, 132(5):54107, 2010.

[71] H. Nyquist. Thermal agitation of electric charge in conductors. *Physical Review*, 32(1):110, 1928.

[72] H. B. Callen and T. A. Welton. Irreversibility and generalized noise. *Physical Review*, 83(1):34, 1951.

[73] C. R. Bartels, B. Crist, and W. W. Graessley. Self-diffusion coefficient in melts of linear polymers: chain length and temperature dependence for hydrogenated polybutadiene. *Macromolecules*, 17(12):2702–2708, 1984.

[74] D. S. Pearson, L. J. Fetters, W. W. Graessley, G. Ver Strate, and E. von Meerwall. Viscosity and self-diffusion coefficient of hydrogenated polybutadiene. *Macromolecules*, 27(3):711–719, 1994.

[75] M. Rubinstein and R. Colby. *Polymers physics*, volume 767. Oxford Oxford, UK, 2003.

[76] J. Klein. The onset of entangled behavior in semidilute and concentrated polymer solutions. *Macromolecules*, 11(5):852–858, 1978.

[77] M. Daoud and P. G. De Gennes. Some remarks on the dynamics of polymer melts. *Journal of Polymer Science: Polymer Physics Edition*, 17(11):1971–1981, 1979.

[78] H. Watanabe and T. Kotaka. Viscoelastic properties and relaxation mechanisms of binary blends of narrow molecular weight distribution polystyrenes. *Macromolecules*, 17(11):2316–2325, 1984.

[79] H. Watanabe, M. Yamazaki, H. Yoshida, and T. Kotaka. Viscoelastic properties of binary blends of linear polystyrenes: further examination of constraint release models. *Macromolecules*, 24(20):5573–5581, 1991.

[80] W. W. Graessley. Entangled linear, branched and network polymer systems-molecular theories. In *Synthesis and Degradation Rheology and Extrusion*, pages 67–117. Springer, 1982.

[81] S. K. Sukumaran and A. E. Likhtman. Modeling entangled dynamics: comparison between stochastic single-chain and multichain models. *Macromolecules*, 42(12):4300–4309, 2009.

[82] Z. Wang, A. E. Likhtman, and R. G. Larson. Segmental dynamics in entangled linear polymer melts. *Macromolecules*, 45(8):3557–3570, 2012.

[83] M. Wang, A. E. Likhtman, and B. D. Olsen. Tube Curvature Slows the Motion of Rod–Coil Block Copolymers through Activated Reptation. *ACS Macro Letters*, 4(2):242–246, 2015.

[84] P. Hänggi, P. Talkner, and M. Borkovec. Reaction-rate theory: fifty years after Kramers. *Reviews of Modern Physics*, 62(2):251, 1990.

[85] A. Rojnuckarin, S. Kim, and S. Subramaniam. Brownian dynamics simulations of protein folding: access to milliseconds time scale and beyond. *Proceedings of the National Academy of Sciences*, 95(8):4288–4292, 1998.

[86] E. Darve and E. Ryu. Computing reaction rates in bio-molecular systems using discrete macro-states. In *Innovations in Biomolecular Modeling and Simulations, Vol 1*, number 23 in RSC Biomolecular Sciences, pages 138–206. 2012.

[87] R. Costaouec, H. Feng, J. Izaguirre, and E. Darve. Analysis of the accelerated weighted ensemble methodology. *Discrete and Continuous Dynamical Systems*, pages 171–181, 2013.

[88] Y. I. Kifer. Certain results concerning small random perturbations of dynamical systems. *Theory of Probability & Its Applications*, 19(3):487–505, 1975.

[89] S. M. Meerkov and T. Runolfsson. Residence time control. *IEEE Transactions on Automatic Control*, 33(4):323–332, 1988.

[90] D. Chandler. Statistical mechanics of isomerization dynamics in liquids and the transition state approximation. *Journal of Chemical Physics*, 68(6):2959–2970, 1978.

[91] C. H. Bennett. Algorithms for chemical computations. In *ACS symposium Series*, volume 46, pages 63–97, 1977.

[92] H. C. Öttinger. *Stochastic processes in polymeric fluids: tools and examples for developing simulation algorithms.* Springer Science & Business Media, 2012.

[93] K. Kratzer, A. Arnold, and R. J. Allen. Automatic, optimized interface placement in forward flux sampling simulations. *Journal of Chemical Physics*, 138(16):164112, 2013.

[94] M. P. Allen and D. J. Tildesley. *Computer simulation of liquids.* Oxford University Press, 1989.

[95] D. A. Vega, J. M. Sebastian, W. B. Russel, and R. A. Register. Viscoelastic properties of entangled star polymer melts: Comparison of theory and experiment. *Macromolecules*, 35(1):169–177, 2002.

[96] S. J. Park, S. Shanbhag, and R. G. Larson. A hierarchical algorithm for predicting the linear viscoelastic properties of Polymer melts with long-chain branching. *Rheologica Acta*, 44(3):319–330, 2005.

[97] P. S. Desai, B.-G. Kang, M. Katzarova, R. Hall, Q. Huang, S. Lee, M. Shivokhin, T. Chang, D. C. Venerus, J. Mays, J. D. Schieber, and R. G. Larson. Challenging Tube and Slip-Link Models: Predicting the Linear Rheology of Blends of Well-Characterized Star and Linear 1,4-Polybutadienes. *Macromolecules*, 49:4964–4977, 2016.

[98] Y. Masubuchi, G. Ianniruberto, F. Greco, and G. Marrucci. Entanglement

molecular weight and frequency response of sliplink networks. *Journal of Chemical Physics*, 119(13):6925–6930, 2003.

[99] Y. Masubuchi, G. Ianniruberto, F. Greco, and G. Marrucci. Molecular simulations of the long-time behaviour of entangled polymeric liquids by the primitive chain network model. *Modelling and Simulation in Materials Science and Engineering*, 12(3):S91, 2004.

[100] T. Yaoita, T. Isaki, Y. Masubuchi, H. Watanabe, G. Ianniruberto, F. Greco, and G. Marrucci. Highly entangled polymer primitive chain network simulations based on dynamic tube dilation. *Journal of Chemical Physics*, 121(24):12650–12654, 2004.

[101] M. E. Shivokhin, E. Van Ruymbeke, C. Bailly, D. Kouloumasis, N. Hadjichristidis, and A. E. Likhtman. Understanding constraint release in star/linear polymer blends. *Macromolecules*, 47(7):2451–2463, 2014.

[102] A. E. Likhtman. Viscoelasticity and molecular rheology. In *Polymer Science: A Comprehensive Reference*, pages 133–179. Elsevier B.V., 2012.

[103] A. V. Brukhno, J. Anwar, R. Davidchack, and R. Handel. Challenges in molecular simulation of homogeneous ice nucleation. *Journal of Physics: Condensed Matter*, 20(49):494243, 2008.

[104] D. Quigley and P. M. Rodger. Metadynamics simulations of ice nucleation and growth. *Journal of Chemical Physics*, 128(15):154518, 2008.

[105] A. Borgia, P. M. Williams, and J. Clarke. Single-molecule studies of protein folding. *Annual Review of Biochemistry*, 77:101–125, 2008.

[106] T. Li, D. Donadio, G. Russo, and G. Galli. Homogeneous ice nucleation from supercooled water. *Physical Chemistry Chemical Physics*, 13(44):19807–19813, 2011.

[107] G. M. Torrie and J. P. Valleau. Nonphysical sampling distributions in Monte Carlo free-energy estimation: Umbrella sampling. *Journal of Computational Physics*, 23(2):187–199, 1977.

[108] C. Dellago, P. G. Bolhuis, F. S. Csajka, and D. Chandler. Transition path sampling and the calculation of rate constants. *Journal of Chemical Physics*, 108(5):1964–1977, 1998.

[109] R. J. Allen, C. Valeriani, and P. R. ten Wolde. Forward flux sampling for rare event simulations. *Journal of Physics: Condensed Matter*, 21(46):463102, 2009.

[110] E. E. Borrero and F. A. Escobedo. Folding kinetics of a lattice protein via a forward flux sampling approach. *Journal of Chemical Physics*, 125(16):164904, 2006.

[111] J. Qin and S. T. Milner. Tubes, topology, and polymer entanglement. *Macromolecules*, 47(17):6077–6085, 2014.

[112] M. Freidlin, J. Szucs, and A. Wentzell. *Random Perturbations of Dynamical Systems*. Springer New York, 2012.

[113] J. Ramirez, S. K. Sukumaran, and A. E. Likhtman. Significance of cross correlations in the stress relaxation of Polymer melts. *Journal of Chemical Physics*, 126(24):244904, 2007.

[114] T. Uneyama and Y. Masubuchi. Multi-chain slip-spring model for entangled polymer dynamics. *Journal of Chemical Physics*, 137(15):154902, 2012.

[115] A. E. Likhtman, S. K. Sukumaran, and J. Ramirez. Linear viscoelasticity from molecular dynamics simulation of entangled polymers. *Macromolecules*, 40(18):6748–6757, 2007.

[116] P. Bačová, H. Lentzakis, D. J. Read, A. J. Moreno, D. Vlassopoulos, and C. Das. Branch-point motion in architecturally complex polymers: estimation of hopping parameters from computer simulations and experiments. *Macromolecules*, 47(10):3362–3377, 2014.

[117] J. A. Anderson, C. D. Lorenz, and A. Travesset. General purpose molecular dynamics simulations fully implemented on graphics processing units. *Journal of Computational Physics*, 227(10):5342–5359, 2008.

[118] J. Glaser, T. D. Nguyen, J. A. Anderson, P. Lui, F. Spiga, J. A. Millan, D. C. Morse, and S. C. Glotzer. Strong scaling of general-purpose molecular dynamics simulations on GPUs. *Computer Physics Communications*, 192:97–107, 2015.

[119] J. Ramirez, S. K. Sukumaran, B. Vorselaars, and A. E. Likhtman. Efficient on the fly calculation of time correlation functions in computer simulations. *Journal of Chemical Physics*, 133(15):154103, 2010.

[120] T. C. B. McLeish, J. Allgaier, D. K. Bick, G. Bishko, P. Biswas, R. Blackwell, B. Blottiere, N. Clarke, B. Gibbs, D. J. Groves, and Others. Dynamics of entangled H-polymers: Theory, rheology, and neutron-scattering. *Macromolecules*, 32(20):6734–6758, 1999.